# GENERALIZED OHM'S LAW AT THE PLASMA-VACUUM INTERFACE

A Dissertation

Presented to the Faculty of the Graduate School

of Cornell University

in Partial Fulfillment of the Requirements for the Degree of

Doctor of Philosophy

by

Matthew Ryan Martin

May 2010

GENERALIZED OHM'S LAW AT THE PLASMA-VACUUM INTERFACE

Matthew Ryan Martin, Ph.D.

Cornell University 2010

We address the generalized Ohm's law description of current driven plasma flows with finite extent in a vacuum. In pulsed power experiments, initially solid density targets are resistively heated until they form a coronal plasma through surface ablation. The coronal plasma then expands into the vacuum chamber. We show that the resistive MHD approximation does not provide self consistent solutions at low densities near the plasma edge where the electron inertial length is of order the system size. It is shown that the two-fluid model allows for simulation of these plasmas in a consistent and numerically efficient manner, propagating the two-fluid waves where the species' inertial lengths are large and recovering the MHD limit when the species inertial lengths are smaller than the grid spacing. When the two-fluid model is applied to simulating pulsed power loads, the finite electron mass limits current flow near the plasma edge, removing the requirement of resistive MHD to invoke anomalous collisionality as a means to confine current flow to the plasma. The two-fluid model is simplified through introduction of a generalized Ohm's law, and using this model we develop a semi-implicit numerical scheme to advance the generalized Ohm's law system. Our formulation of this system allows for stable integration while taking time steps typical of MHD. Our method avoids the solution of curl-curl differential operator with discontinuous magnetic diffusion coefficient, which is required when an induction equation formulation is applied to problems with a vacuum interface. This is accomplished by includ-

ing both finite electron inertia and displacement current in our system of equations while decreasing the speed of light to a few times the fastest velocities of interest. This results in efficient computation of the Hall physics without the computational difficulties of Hall MHD. Additionally, the model allows us to simulate two-fluid physics over previously inaccessible time and space scales, such as those typical of wire array Z-pinches. We use the code to investigate the two-fluid physics of wire arrays, plasma slabs, and magnetic bubbles. Our numerical investigations show that our generalized Ohm's law model predicts flows and instabilities that MHD would otherwise neglect.

## BIOGRAPHICAL SKETCH

Matthew Ryan Martin was born in Bartlesville, Oklahoma on May 30, 1981. He attended Field Kindley Memorial High School in Coffeyville, KS and graduated in 1999. He then attended Kansas State University where he received a Bachelors of Science in Computer Engineering in 2003 and a Masters of Science in Electrical Engineering in 2004. He then went on to Cornell University to study plasma physics, receiving his Ph.D. in Electrical Engineering in 2010.

**ACKNOWLEDGEMENTS**

First and foremost, I would like to thank my advisor Charles Seyler for his guidance and advice throughout my graduate studies. His mathematical insight and deep understanding of physics were an inspiration and served as a goal to strive for. None of this work would have been possible without his ideas and assistance. I want to thank the Laboratory of Plasma Studies for the financial support of my graduate studies. As such, I would like to thank David Hammer and Bruce Kusse for putting together an excellent experimental plasma physics group. In particular, I would like to thank David Hammer for taking time to be on my committee and for his advice over the years. My first class in computational fluid dynamics was taught by Kenneth Torrance, who I also had the pleasure of having on my committee. I would like to thank him for challenging me to broaden my studies in classical mechanics and for serving as minor field member of my committee. I'm deeply indebted to John Greenly for everything he taught me about experimental pulsed power and for his willingness to test our theories. A great deal of my understanding of the workings of pulsed power machines and its diagnostics resulted from conversations with Jon Douglass, Ryan McBride, Isaac Blesener, Patrick Knapp, and the other graduate students in the lab. Thanks for always helping me find experimental datasets and thanks for all the beers at the Barn. My involvement in this field is mostly due to the encouragement of Tom Mehlhorn and I want to thank him along with Ray Lemke and Mike Desjarlais for serving as mentors during my internships at Sandia National Labs. Early on in my graduate studies I had the pleasure of sharing an office with Kaijun Liu. I want to thank him for always being available and able to answer any question I had about plasma physics. I owe an extreme debt to Nicola Kinzie for taking the time to proofread my thesis. I look

forward to repaying it by proofreading yours someday. Finally, I want to thank my Family for their love and constant support.

## TABLE OF CONTENTS

## LIST OF TABLES

## LIST OF FIGURES

CHAPTER 1

# INTRODUCTION

The simulation and analysis of pulsed power generated plasmas is an inherently difficult problem due to the massive breadth of physics required to described the flow of mega-amps of current into micro-grams of matter over tens to hundreds of nanoseconds. This is a multi-physics problem that draws upon many diverse fields, such as electromagnetism, statistical mechanics, and quantum mechanics. In addition to its multi-physics nature, the time evolution of these systems contains important physical phenomena that extend across several orders of magnitude in time and space, making them truly multi-scale problems. In this thesis we strive to focus on one narrow but important topic: a self consistent numerical model for Joule heating driven, ionized gas expanding into a vacuum. The pulsed power production mechanism of plasmas has typically required that they have finite extent in a vacuum chamber. A proper understanding of the expansion of a Joule heated plasma into vacuum while in the presence of strong magnetic fields becomes exceedingly important. To date, the simulation of such flows is limited to the resistive magneto-hydrodynamic (MHD) model. We explore the range of validity for resistive MHD and build a self-consistent picture of the low density expansion front of magnetized plasma driven by Joule heating.

We perform this analysis while considering a specific pulsed power load, the cylindrical wire array. The wire array Z-pinch has been shown to be a versatile and efficient X-ray source which has been studied as a driver for inertial confinement fusion targets [1, 2]. This configuration has also found success as a K-shell X-ray source [3], and slight modifications to the geometry make it use-

ful for exploring laboratory astrophysics [4]. Wire arrays, applied to all of these applications, share the same qualitative physical evolution. A cylindrical array of wires moves through distinct stages before the final implosion and pinch on axis. We briefly describe the time dependent behavior of a wire array driven by a pulsed power load.

First the wires experience a resistive heating phase where large voltages develop as the coronal plasma is formed [5]. The coronal plasma is the relatively hot plasma that surrounds the cold dense core and is responsible for shunting current away from the core. Once break down occurs, the core is thought to not be fully ionized, but in a mixed liquid-gas phase [6]. After voltage collapse, the coronal plasma heats, redirecting most of the current from the core. The core is ablating mass and feeding the coronal plasma [7]. The exact details of the energy partition of thermal transport and radiation transport between the multi-phase core and coronal plasma is not completely understood. However, the core is found to roughly ablate in agreement with the rocket model [8]. Early on, instability occurs in the coronal plasma which is commonly referred to as the "fundamental" mode [9] of the array as it is thought that each wire material possesses a unique wavelength. The hot coronal plasma is directed in collimated streams toward the geometric axis of the array. The streams collide in the center forming a precursor column. The non-uniform ablation due to the fundamental mode causes gaps to form in the wire cores. As the wire cores lose mass, the array starts its implosion toward the axis, snowplowing [10] through the ablated prefill. As a result of the non-uniform ablation due to the fundamental mode, trailing mass is left behind. Magneto-Rayleigh-Taylor instability [11] of the imploding mass decreases the convergence of the final pinch on the axis. Finally, for our times of interest, stagnation of the pinch occurs on axis, where

the majority of the X-ray production occurs [12].

In the following chapters we will develop analytic and numeric models to explore the streaming ablation and precursor formation stages of the cylindrical wire array pulsed power load. Our focus will be on the correct treatment of the plasma-vacuum interface and the selection of an appropriate level of approximation with which to analyze these flows. In chapter two we analyze the plasma parameters and construct a generalized Ohm's law (GOL) model. In chapter three we develop a numerical model that allows for efficient simulation of the generalized Ohm's law system of equations. In chapter four we test the numerical model and explore the two-fluid and MHD limits. In chapter five we develop a theory based on resistive MHD to describe the initiation of ablation in wire arrays. In chapter six the generalized Ohm's law model is compared to resistive MHD when modeling the dynamics of the plasma vacuum interface in a 1D sheet pinch. In chapter seven we perform two-dimensional implosions of infinitely long cylindrical wire arrays in two dimensions. Finally, in chapter eight, alternative pulsed power loads such as imploding slabs and magnetic-bubble forming foils are simulated with the generalized Ohm's law code.

CHAPTER 2

# GENERALIZED OHM'S LAW NEAR THE PLASMA-VACUUM INTERFACE

In this chapter, we explore the collisional transport, which dominates the single fluid resistive MHD model, to the collisionless transport of the two-fluid plasma description, focusing on the case of plasma near the vacuum interface. That is under the confines of the fluid approximation, we approach the question of how to properly represent the physics of ionized flows in a strong magnetic field with number densities from $10^{18}\text{cm}^{-3}$, where the Hall electric field is important, to number densities as low as $10^{12}\text{cm}^{-3}$, where the inertia of electrons is not negligible. This density range is defined as the plasma-vacuum interface where 'plasma' describes the leading edge of an ablation front. The 'vacuum' refers to the part of the computational domain which contains the background fill gas of the vacuum chamber. The common method for applying boundary conditions on the magnetic field in numerical simulation requires this numerical 'vacuum' region apply to cells below a density cutoff. Below the cutoff density the cells are transparent to magnetic fields and evolved with special rules. A proper description of both regions is required for simulation of a metal plasma with finite extent in a vacuum chamber.

In the resistive MHD model the transition from a current carrying high density plasma to the relatively insulating background density may only be achieved through increasing the resistivity of the low density plasma beyond the classical Spitzer value. The classical Spitzer value corresponds to the diffusion coefficient of an ionized plasma where electron-electron collisions are considered [13] and for a transverse magnetic field is approximately

$1.29x10^4 Z \ln\Lambda/T^{\frac{3}{2}}$ ohm-cm, where $\ln\Lambda$ is the Coulomb logarithm. The kinetic theory of plasmas predicts mechanisms such as wave-particle interactions which will enhance the resistivity in low density regions. These "anomalous" collisions are often invoked in the resistive MHD model as they provide a means to limit current flow and decouple the force of the magnetic field from the flow. Instead of invoking kinetic modifications to the single fluid transport coefficients, we consider transport of individual species through the two-fluid model. The two-fluid model considers the electrons as a separate species from the ions. This gives electrons a separate equation of motion and finite response time to an applied electric field. We show that this finite electron inertia plays a similar role in limiting current flow at the plasma-vacuum interface to that of anomalous collisions.

In the following chapter we will discuss the validity of the single fluid model in plasmas with a vacuum interface, first through analyzing the dimensionless parameters that are encountered in wire array ablation. Next, we introduce the two-fluid plasma model and simplify its description through a reduced generalized Ohm's law. We then explore the application of anomalous resistivity in modeling wire array ablation and question the validity of the single fluid MHD model in describing the evolution of the plasma-vacuum interface. We show the two-fluid plasma model limits the current flow at the plasma-vacuum interface through the inclusion of finite electron inertia and that it is non-negligible when compared to the effects of lower-hybrid micro-turbulence.

## 2.1 Wire-Array Plasma Parameters

To make progress in the analysis of plasma flows extending into a vacuum, it is import to understand the range of length scales, time scales, and transport coefficients that parameterize the system. If we first consider variables describing the evolution of the gas dynamics, it is immediately apparent that the mean fluid velocity due to ablation, experimentally measured to be of order 100 km $s^{-1}$, will exceed the local sound speed of the Joule heated plasma which is of order 10 km $s^{-1}$. This suggests that it is advantageous for a numerical method treating these flows to be shock capturing.

The next parameter we consider is the viscosity of the coronal plasma. The coefficient of dynamic viscosity is approximated by $\mu = nk_bT/\nu_c$ where $n$ is the number density of $10^{18}$ $cm^{-3}$ , $k_b$ is the Boltzmann constant, $T$ is the plasma temperature taken to be 10 eV and $\nu_c$ is the ion collision frequency of $10^{11}$ $s^{-1}$ [14]. For the given values of a typical aluminum coronal plasma the kinematic viscosity $\mu/\rho$ is of order $10^{-5}$ $m^2$ $s^{-1}$ with $\rho$ representing the mass density of the fluid. The Reynolds number, $R_e$, is defined as the ratio of the dissipation timescale to the convection timescale. For the coronal plasma parameters where the flow velocity varies from 1 km $s^{-1}$ to 100 km $s^{-1}$ with a convective scale length of order 1 mm, the Reynolds number varies from $R_e \approx 10^5$ to $R_e \approx 10^7$. For most regions of interest the thickness of the momentum boundary layer is small, and the coronal plasma can be considered inviscid.

Since the hot coronal plasma is in contact with the relatively cold core of the wire, conduction will play a role in the transport of energy. The electron collision frequency $\nu_{ee}$ is estimated from the previously calculated ion collision

frequency as $\nu_{ee} = \nu_{ii}(m_e/m_i)^{-\frac{1}{2}} \approx 10^{12}\,\mathrm{s}^{-1}$. The thermal conductivity, $\kappa$ is defined as $\kappa = 5n_e k_b^2 T_e/2m_e\nu_{ee}$ and is approximately 10 W m$^{-1}$ K. As discussed in [15], the value of the electron thermal conduction coefficient is small relative to that of radiation conduction, $\kappa_{rad}$. Radiative cooling and other transport mechanisms are important in capturing the energetics of these hot metal plasmas but are outside of the scope of this thesis. It is important to note that the value of the transport coefficients, specifically the plasma conductivity, is a topic of controversy in modeling wire arrays. It is common practice in codes such as ALEGRA to decrease the conductivity in the cold wire core region by a factor of 100 from the Spitzer value to obtain agreement with experiment [16]. Doing so will artificially enhance the role of thermal conduction and radiation transport by suppressing the Joule heating of the wire core material. With this in mind we will now explore the extreme ranges of plasma length and time scales for a typical coronal plasma extending into a vacuum.

The magnetic Reynolds number $R_m$ is defined as the ratio of magnetic advection to that of magnetic diffusion and is given by $R_m = UL\mu_0/\eta$ where U is the flow velocity,$L$ is the characteristic length scale, $\mu_0$ is the magnetic permeability, and $\eta$ is the plasma resistivity. Deviation from the Spitzer value of plasma resistivity is expected in the low density plasma where wave-particle interactions occur and in the high density core region where a mixture of liquid and vapor metal exists, so we will consider a packet of coronal plasma with number density $10^{20}$ cm$^{-3}$ at 10 eV. This is a reasonable estimate for coronal plasma ablated from the core. The transverse Spitzer resistivity is of order $10^{-5}$ Ω–m and the typical fluid velocity near the core can be estimated from the sound speed and is approximately 10 km s$^{-1}$. The magnetic Reynolds number in the corona will vary depending upon location, with $R_m \approx 1$ near the corona. As we move to-

ward the array axis, the Reynolds number will then rapidly increase along with the flow velocity such that $R_m >> 1$. This implies that at the very least resistive MHD is required to describe ablative flows.

In these hot plasmas the Debye length, the scale length over which electric fields from charge separation are screened out, will be at most of order tens of microns in the lower density plasmas. It is approximately equal to $7.43x10^2 T^{\frac{1}{2}} n^{\frac{-1}{2}} cm$ where the temperature T is in eV and the number density n is in particles per $cm^3$ [14]. The background number density can be estimated from the ideal gas law with a pump down pressure of $10^{-5}$ Torr and a temperature of 300 K. This gives a number density of $10^{11}$ $cm^{-3}$ as a lower bound. In reality the number density will be much higher near the wires due to out-gassing effects. Assuming the plasma is ionized at a few eV, charge separation effects should be negligible unless we consider scale lengths under tens of microns. Thus we can assume that quasi-neutrality will hold over the bulk of the plasma. However, charge separation effects most likely influence the low density plasmas encountered in the vacuum chamber. Most analysis of the subject for numerical simulation ends at this point, and it assumes that the resistive MHD model is appropriate. We go a step further and consider the role of the separate ion and electron flows in the system. This introduces new scale parameters via the two-fluid model that will indicate where the single fluid approximation could fail.

Continuing on with the analysis of an ablating wire, we now introduce a new scale length associated with finite electron mass. The electron inertial length is defined by the speed of light divided by the plasma frequency $\lambda_e = c/\omega_{pe}$. The plasma frequency is approximately equal to $5.64x10^4 n_e^{\frac{1}{2}}$ rad $sec^{-1}$, where $n_e$ is

the electron number density per $cm^3$ [14]. When this scale length is of order of the system of interest ($\approx$ 1 mm) then we can expect the inertial physics to influence the evolution of the system. The inertial length scales inversely with the square root of the number density with a value of 10's of nanometers in the wire core, extending to 10's of millimeters for our estimate of the background number density. This suggests the electron mass will play a role in the transition to the background number density for a plasma sheet flowing from the wire. The second length scale we will consider is the ion inertial length. The ion inertial length is defined as the speed of light divided by the ion cyclotron frequency $\lambda_i = c/\omega_{pi}$. To determine its value we can multiply the electron inertial length by the square root of the ion to electron mass ratio which for an aluminum plasma is approximately $\sqrt{27x1836}$. This means that for the highest density plasma, the ion inertial length will be of order tens of microns and of order 1 mm for number densities of $10^{18}$ $cm^{-3}$. As we move to the background plasma, the Hall term will be important at higher density relative to the electron inertia terms.

Neglecting the role of radiation transport and thermal conduction, the above analysis of scale parameters suggests that the inviscid two-fluid plasma model provides an appropriate physical description of wire arrays. Ignored in this analysis are the roles of fractional ionization and the equation of state. Neither topic will not be explored in this thesis. In the next section we derive a simplified system of equations based on the two-fluid plasma description. This generalized Ohm's law model includes dynamics on the ion and electron inertial length scales which play an import role at the plasma-vacuum interface of ablative flows.

## 2.2 The Generalized Ohm's Law Approximation

The basis for our analysis of plasma expanding into a vacuum in this chapter is the generalized Ohm's law model. The form of Ohm's law used in literature varies due to the different levels of approximation applied to the time and length scales of interest, so we now derive a self consistent formulation for the evolution of a two species plasma in a center-of-mass frame and will compare to other approximate forms of Ohm's law commonly used to describe plasmas in pulsed power applications.

The most fundamental description for the evolution of particles in our system is provided by the kinetic description of a plasma. The distribution function $f(\mathbf{r}, \mathbf{v}, t)$ gives the number density of particles for a volume element at radius $\mathbf{r}$ and around velocity $\mathbf{v}$ as a function of time $t$. Under the assumption of conservation of particles, the evolution of the distribution function is given by the collisional kinetic equation

$$\frac{\partial f_\alpha}{\partial t} + \mathbf{v} \cdot \frac{\partial f_\alpha}{\partial \mathbf{r}} + \frac{\mathbf{F}}{m} \cdot \frac{\partial f_\alpha}{\partial \mathbf{v}} = \left( \frac{\partial f_\alpha}{\partial t} \right)_c \tag{2.1}$$

where $\mathbf{F} = q(\mathbf{E} + \mathbf{v} \times \mathbf{B})$ is the macroscopic force due to the electric field $\mathbf{E}$ and the magnetic field $\mathbf{B}$. The collision operator is $(\partial f / \partial t)_c$ and the individual species are $\alpha$ are ions and electrons.

The analytic and numerical complications of analyzing wire array flows in the six dimensional phase space given by Equation 2.1 compels us to simplify the description. This simplification is achieved by removing the velocity dependence of the distribution function by integrating over all velocity space leading to an infinite chain of moment equations. We assume a five-moment closure

which results in a modified Euler equation for each species. The details of this procedure can be found in [17] but will not be addressed here. The zeroth moment, found by integrating Equation 2.1 over velocity space provides a continuity equation for each species representing conservation of mass and is given by

$$\frac{\partial n_\alpha}{\partial t} + \nabla \cdot (n_\alpha \mathbf{u}_\alpha) = 0 \tag{2.2}$$

where $n_\alpha$ is the number density of species $\alpha$ and $\mathbf{u}_\alpha$ is the fluid velocity of species $\alpha$. In addition to conservation of mass, conservation of momentum is required. The equation describing this constraint is found by multiplying Equation 2.1 by the particles velocity $\mathbf{v}$, then integrating over velocity space. The first moment equation is

$$\frac{\partial \rho_\alpha \mathbf{u}_\alpha}{\partial t} + \nabla \cdot (\rho_\alpha \mathbf{u}_\alpha \mathbf{u}_\alpha + P_\alpha \mathbf{I}) = \frac{q_\alpha \rho_\alpha}{m_\alpha} (\mathbf{E} + \mathbf{u}_\alpha \times \mathbf{B}) + \mathbf{R}_\alpha \tag{2.3}$$

where $\rho_\alpha$ is the species mass density and $P_\alpha$ is the species pressure. This five moment closure assumes the simplifications for an inviscid plasma with isotropic pressure whose rate of momentum transfer between species is given by $\mathbf{R}_\alpha$. Since the full description requires an infinite chain of moment equations, we must truncate the system at some point. If we assume an isotropic pressure and an ideal equation of state $P_\alpha = n_\alpha k T_\alpha$, the evolution of the internal energy density $\epsilon_\alpha = P_\alpha / (\gamma - 1) + \rho_\alpha u_\alpha^2 / 2$ is determined by multiplying Equation 2.1 by $v^2$ and then integrating over velocity space which gives the equivalent equation

$$\frac{\partial \epsilon_\alpha}{\partial t} + \nabla \cdot [\mathbf{u}_\alpha (\epsilon_\alpha + P_\alpha)] = q_\alpha n_\alpha \mathbf{u}_\alpha \cdot \left[\mathbf{E} - \frac{\mathbf{R}_\alpha}{q_\alpha n_\alpha}\right] \tag{2.4}$$

The set of five moment Equations 2.2 - 2.4, along with Maxwell's equations and the ideal equation of state, form the two-fluid model of plasma physics. As we will discuss in Chapter 3, the numerical solution of the full set of two-fluid equations is computationally expensive, therefore a reduced model is desirable. The standard simplification of the two-fluid model is to assume quasi-neutrality, neglect displacement current, move the system into a center-of-mass frame, and neglect terms of order $m_e/m_i$ to simplify the equations and remove physics associated with charge separation and light waves. However, it will be shown in Chapter 3 that it is advantageous to keep displacement current in our numerical model as the numerical propagation of the electric and magnetic fields via light waves is tractable on pulsed power timescales, whereas advancing the fields through solution of an induction equation based on generalized Ohm's law and neglecting displacement current will at best involve implicitly solving a stiff linear system. Keeping displacement current in Maxwell's equations while assuming quasi-neutrality does not result in an obviously self-consistent model. Displacement current in Maxwell's equations implies that upon taking the divergence of Ampere's law

$$\frac{\partial \rho_c}{\partial t} + \nabla \cdot \mathbf{j} = 0 \tag{2.5}$$

where as quasi-neutrality requires that $n_i \approx n_e$. Since the free charge density $\rho_c$ is given by $Zen_i - en_e$, displacement current along with the quasi-neutrality assumption appears to give a contradiction if $\nabla \cdot \mathbf{j}$ is introduced through numerical error and free charge builds up in a system where we neglected terms that would self-consistently return the system to equilibrium. If the divergence

of the current density is kept zero, the model is consistent since the desired electromagnetic propagation of waves only depends upon the divergence free transverse electric field. As is the case with the magnetic field, numerical error will introduce divergence errors, which in the case of the current density term creates a longitudinal electric field and free charge density that can violate the quasi-neutral assumption. We look to alternative methods in lieu of imposing a $\nabla \cdot \mathbf{j} = 0$ constraint.

### 2.2.1 Reduced Two-Fluid Model and Displacement Current

We now explore the compatibility of a reduced two-fluid model and displacement current in a numerical model where the divergence of the current density is not necessarily zero and the Debye length is much smaller than any scale length of interest. We reduce the two-fluid model only for terms of order $m_e/m_i$ and then consider the evolution in the center-of-mass frame which poses the evolutionary equations for ions and electrons in terms of the combined mass and combined charge density. We define the ion velocity $\mathbf{u}_i$ and electron velocity $\mathbf{u}_e$ in terms of the center-of-mass fluid velocity $\mathbf{u}$ and the Hall velocity $\mathbf{\Gamma} = \mathbf{u_i} - \mathbf{u_e}$ as follows

$$\mathbf{u}_i = \mathbf{u} + \frac{\rho_e}{\rho}\mathbf{\Gamma} \tag{2.6}$$

$$\mathbf{u}_e = \mathbf{u} - \frac{\rho_i}{\rho}\mathbf{\Gamma} \tag{2.7}$$

where the combined mass density of the species is $\rho = m_e n_e + m_i n_i$. We now substitute in definitions for the total mass density and Equations 2.6-2.7 into

Equations 2.2 - 2.4 while neglecting terms of order $m_e/m_i$ along with the assumption that $Z \ll \sqrt{m_i/m_e}$ where $Z$ is the ionization state. The resultant equations are nondimensionalized with respect to the reference Alfven velocity $V_{a0} = B_0/\sqrt{\mu_0\rho_0}$ where constants with dimension are denoted by '0', otherwise the variable or constant is assumed dimensionless. Our choice of reference magnetic field, length scale, and number density set the reference Hall velocity $V_{h0} = B_0/(\mu_0 L_0 e n_{e0})$ and electron inertial length $\lambda_{e0} = c_0/\omega_{pe0}$. The reference fields result in a set of dimensionless parameters including the plasma beta $\beta = P\mu_0 P_0/B_0^2$, the electron plasma beta $\beta_e = \left(\mu_0 P_e/B_0^2\right)(\rho_0/\rho_{e0})$, the Hall velocity $V_h = V_{h0}/(V_{a0} n_e)$, the Lundquist number $S = \mu_0 L_0 V_{a0}/\eta$, and the previously introduced electron inertial length $\lambda_e^2 = \lambda_{e0}^2/L_0^2/n_e$. The result of averaging the electron and ion continuity equations is

$$\frac{\partial \rho}{\partial t} + \nabla \cdot (\rho \mathbf{u}) = 0 \tag{2.8}$$

$$\frac{\partial \rho_c^*}{\partial t} + \nabla \cdot \mathbf{j} = 0 \tag{2.9}$$

which describes the conservation of mass (2.8) and the conservation of charge (2.9) for the reduced system. We have introduced $\rho_c^* = \rho_c V_{a0}^2/c_0^2$ to simplify the equations. Next, averaging the two-fluid model momentum equations for ions and electrons and defining $\xi = 1 + V_{h0}\rho_c^*/(V_{a0} n_e)$ gives

$$\frac{\partial \rho \mathbf{u}}{\partial t} + \nabla \cdot \left[\rho \mathbf{u}\mathbf{u} + \lambda_e^2 \left(\mathbf{j}\mathbf{j} + \rho_c^* \left[\rho_c \mathbf{u}\mathbf{u} - \mathbf{u}\mathbf{j} - \mathbf{j}\mathbf{u}\right]\right) + \beta \mathbf{I}\right] = \rho_c^* \mathbf{E} + \mathbf{j} \times \mathbf{B} \tag{2.10}$$

$$\frac{\partial \mathbf{j}}{\partial t} + \nabla \cdot \left[\xi \left(\mathbf{u}\mathbf{j} + \mathbf{j}\mathbf{u} - \rho_c^* \mathbf{u}\mathbf{u}\right) - V_h \mathbf{j}\mathbf{j} - \frac{V_{a0}}{V_{h0}} \beta_e \mathbf{I}\right] = \tag{2.11}$$

$$\lambda_e^{-2}\left[\mathbf{E}+(\xi\mathbf{u}-V_h\mathbf{j})\times\mathbf{B}-S^{-1}\left(\mathbf{j}-\rho_c^*\mathbf{u}\right)\right]$$

where (2.10) is our ion momentum equation, (2.11) is the generalized Ohm's law, and **I** is the identity tensor. The details of the derivation for the generalized Ohm's law is given in Appendix A. The species combined energy density $\epsilon$ is defined as

$$\epsilon=\frac{\beta}{\gamma-1}+\frac{1}{2}\rho u^2+\frac{1}{2}\frac{\rho_{e0}}{\rho_0}\rho_e V_h^2\left(\mathbf{j}-\rho_c^*\mathbf{u}\right)^2 \tag{2.12}$$

while the electron fluid energy density $\epsilon_e$ in the center-of-mass frame is

$$\epsilon_e=\frac{\beta_e}{\gamma-1}+\frac{1}{2}\rho_e\left[\mathbf{u}-V_h\left(\mathbf{j}-\rho_c^*\mathbf{u}\right)\right]^2 \tag{2.13}$$

Using these definitions for the energy densities we can combine the individual evolutionary energy equations for ions and electrons which results in

$$\frac{\partial\epsilon}{\partial t}+\nabla\cdot\left[\mathbf{u}\left(\epsilon+\beta\right)-\frac{\rho_{e0}}{\rho_0}V_h\left(\mathbf{j}-\rho_c^*\mathbf{u}\right)\left(\epsilon_e+\beta_e\right)\right]=\mathbf{j}\cdot\mathbf{E}+S^{-1}\left(j^2-\rho_c^*\mathbf{u}\cdot\mathbf{j}\right) \tag{2.14}$$

$$\frac{\partial\epsilon_e}{\partial t}+\nabla\cdot\left[\left(\mathbf{u}-V_h\left[\mathbf{j}-\rho_c^*\mathbf{u}\right]\right)\left(\epsilon_e+\beta_e\right)\right]=\frac{V_{h0}}{V_{a0}}\lambda_e^{-2}\left[V_h\mathbf{j}-\left(V_h\rho_c^*+1\right)\mathbf{u}\right]\cdot\left[\mathbf{E}+S^{-1}\mathbf{j}\right] \tag{2.15}$$

where (2.14) describes the evolution of the combined energy density while (2.15) describes the evolution of the electron fluid energy. Equations 2.8 through 2.15 along with the polytropic equation of state, the dimensionless Faraday's equation,

$$\frac{\partial\mathbf{B}}{\partial t}=-\nabla\times\mathbf{E} \tag{2.16}$$

dimensionless Ampere's equation,

$$\frac{\partial\mathbf{E}}{\partial t}=\frac{c^2}{V_{a0}^2}\left(\nabla\times\mathbf{B}-\mathbf{j}\right) \tag{2.17}$$

the solenoidal constraint on the magnetic field,

$$\nabla \cdot \mathbf{B} = 0 \tag{2.18}$$

together form the complete system of equations. This system 2.8 - 2.18 is consistent with the two-fluid model except in cases where the ion and electron masses are similar, i.e. electron-positron plasmas. It is important to note that this model does not require a quasi-neutral assumption. There exists in this system of equations a hierarchy of asymptotic submodels, such as Hall MHD and ideal MHD, which depend upon the relative magnitudes of the dimensionless parameters. Our goal in the next section is to reduce the model to the minimal set of physics that self-consistently describe the evolution of a wire array plasma.

### 2.2.2 Generalized Ohm's Law System

We now describe a set of simplifications to the reduced two-fluid model that will result in our generalized Ohm's law system. First we consider the effects of charge separation. From the set of dimensionless equations, it is now apparent that charge separation contributions to species momentum and energy may be neglected when $\rho_c \mathbf{u} \ll \mathbf{j}$, when the flow of free charge is much less than the current density. Alternatively, this criterion may be posed as $E_0/B_0 << c^2/u_0$ which is well satisfied for the following set of parameters. For a pulsed power device such as COBRA, peak voltage is of order hundreds of kilovolts and the typical electrode separation distance is 20mm. If the grid spacing is of order 100 microns, then the free charge approximation is satisfied for electron number densities greater than $10^{13}\text{cm}^{-3}$ to $10^{14}\text{cm}^{-3}$ under the first constraint and at all number densities given the second constraint. This is within an order of magni-

tude of our estimate of the background fill gas. The number density constraint is satisfied throughout the majority of the plasma and only violated in 'vacuum' regions. Using these arguments we neglect free charge contributions from the reduced two-fluid model. The charge continuity equation is retained for convenience since the Hall velocity and electron inertial length depend upon the electron number density which can be determined using the dimensional equation

$$n_e = Zn_i - \rho_c/e \tag{2.19}$$

and thus any numerical contribution to the divergence of $\mathbf{j}$ will be treated as free charge whose only role is in modifying the available electron number density.

The next reduction involves physics on the scale length of the electron Larmor radius. This length scale associated with the electron pressure term in Ohm's law is typically in the micron scale and thus unresolvable for systems with overall scale lengths in the tens of millimeters. We assume $\beta_e \ll 1$ for our approximate Ohm's law out of numerical convenience. However, no underlying physical argument requires us to make this approximation. To simplify the analysis, we assume equal electron and ion temperatures. Finally, we consider terms of order $\lambda_e^2\mathbf{jj}$ which are associated with the electron self advection term $\mathbf{u_e}\cdot\nabla\mathbf{u_e}$. Since we have neglected the role of finite electron pressure, including the contribution from self advection is equivalent to an inviscid Burger's equation of motion for electrons. For the majority of the domain the relation $\lambda_i/L_0 \ll u/V_{a0}$ holds and the laminar contribution from the electron fluid negligible. However, for simulations where the electron Larmor radius is resolved turbulent contributions from these self advection terms might be important. These reductions result in the generalized Ohm's law model given by

$$\frac{\partial \rho}{\partial t} + \nabla \cdot (\rho \mathbf{u}) = 0 \tag{2.20}$$

$$\frac{\partial \rho_c^*}{\partial t} + \nabla \cdot \mathbf{j} = 0 \tag{2.21}$$

$$\frac{\partial \rho \mathbf{u}}{\partial t} + \nabla \cdot (\rho \mathbf{u}\mathbf{u} + \beta \mathbf{I}) = \mathbf{j} \times \mathbf{B} \tag{2.22}$$

$$\frac{\partial \mathbf{j}}{\partial t} + \nabla \cdot \left( \mathbf{u}\mathbf{j} + \mathbf{j}\mathbf{u} - V_h \mathbf{j}\mathbf{j} + \frac{V_{a0}}{V_{h0}} \beta_e P_e \mathbf{I} \right) = \lambda_e^{-2} \left( \mathbf{E} + (\mathbf{u} - V_h \mathbf{j}) \times \mathbf{B} - S^{-1} \mathbf{j} \right) \tag{2.23}$$

$$\epsilon = \frac{\beta}{\gamma - 1} + \frac{1}{2} \rho u^2 + \frac{1}{2} \frac{\rho_{e0}}{\rho_0} \rho_e V_h^2 \mathbf{j}^2 \tag{2.24}$$

$$\frac{\partial \epsilon}{\partial t} + \nabla \cdot \left[ \mathbf{u} \left( \epsilon + \beta \right) \right] = \mathbf{j} \cdot \mathbf{E} + S^{-1} j^2 \tag{2.25}$$

which we will apply to analyzing wire array flows. The model includes finite electron inertia and the associated ion-electron advection terms, the Hall electric field, ionization, and resistive effects.

Additional lower order approximations to plasma flow can be derived from this model. If we neglect displacement current from Maxwell's equations and consider the limit where the electron inertial length goes to zero the system reduces to the Hall MHD approximation. Taking the ion inertial length to be zero further reduces the system to the resistive MHD model. Resistive MHD is currently the most common level of approximation used in modeling wire arrays.

Finally, taking the Lundquist number to infinity gives the ideal MHD equations. The question of what level of approximation is appropriate for simulating wire ablation in the presence of a plasma-vacuum interface is the subject of the next section.

## 2.3 Generalized Ohm's Law at the Plasma-Vacuum Interface

The role of Ohm's law varies greatly over flows that originate from high density collisional plasma and extend into a vacuum region. The single fluid approximation is assumed to be appropriate at the plasma ablation source and in this region Ohm's law determines the electric field as a function of the fluid velocity, magnetic field, and resistance. This is in stark contrast to collisionless regions of low density current carrying plasma where Ohm's law depends upon additional parameters such as the difference in species velocities and their inertia. At even lower densities the velocity distributions become non-Maxwellian and the fluid model breaks down. For example, we expect electron beams in extremely low density regions where the electric field exceeds the Dreicer limit [18]. This is the limit to the magnitude of an electric field beyond which electron runaway occurs.

To correctly model the entire experiment would require a kinetic code which is impractical over pulsed power time and length scales if an entire array is to be simulated. Of primary concern in this thesis is the limit to which fluid theory describes the evolution of wire arrays. We focus on the inclusion of electric fields generated by separate species velocities and the modeling of the plasma-vacuum interface. At this interface an insufficient number of charge carriers ex-

ist to support significant current flow. We address this problem within the confines of fluid theory by considering a parcel of low density plasma background plasma subject to an electric field generated from a pulsed power device. For an applied electric field $E_z$, the generalized Ohm's law of Equation 2.23 in one dimension reduces to the equation

$$\frac{\partial j_z}{\partial t} = \frac{L_0^2}{\lambda_{e0}^2} n_e (E_z - \eta j_z) \tag{2.26}$$

under the assumptions that the ion velocity is zero, the electron beta is small, and that we have neglected contributions to electric field from the Hall term. Equation 2.26 describes the time dependence of the current density given the electron number density, applied electric field, and collisionality of the plasma. If we take electron inertial length to be small, we recover the familiar resistive Ohm's law $E_z = \eta j_z$ which is the asymptotic solution to the differential Equation 2.26. It is trivial to find the general solution to this equation when finite electron inertia is retained, and it is given by

$$j_z = \frac{E_z}{\eta}(1 - e^{-\frac{\eta t}{\mu_0 \lambda_e^2}}) \tag{2.27}$$

For this solution ( 2.27 ), we see that regions of plasma in an applied electric field where the resistive diffusion rate is small compared to the dimensionally equivalent electron inertial length squared divided by a characteristic time will not immediately develop the current density as determined by resistive Ohm's law. Assuming a hot ionized background plasma of number density $10^{14}$ cm$^{-3}$ to $10^{15}$ cm$^{-3}$ and the classical Spitzer plasma resistivity for 10 eV, Equation 2.27 states that for our pulsed power time scales the electron response is significant.

The mass of the electron is important at edge of the ablation front.

The exact meaning of the "timescale" $t$ in Equation 2.27 takes two forms in ablation flows. The first form we consider is the time after switching on the driver, when current flow is increasing due to the applied voltage. From the particle perspective this statement makes sense when one considers the velocity of an electron in a 20 kV field typical of the initiation phase. An electron accelerating over a 20 mm gap without collision would be traveling at a few percent of the speed of light, and thus we can expect finite mass effects to be important. During this resistive initiation phase there are large electric fields in excess of the Dreicer limit [13]

$$E_{Dreicer} = 5.6 * 10^{-24} n_e Z ln(\Lambda) T_e^{-1} V/m \tag{2.28}$$

for temperatures of 10 eV and number densities of order $10^{15}\text{cm}^{-3}$ and below. Above this limit the fluid theory of generalized Ohm's law predicts that very low density conductive regions can suffer from charge carrier depletion. A lack of collisions and charge carriers will limit the amount of current over the extremely short response time scale. The necessity of a mechanism for limitation of current flow in a conductor as the resistivity tends to zero is required as part of the mathematical formalism of the plasma system to remove the associated singularity when Ohm's law determines the current density. That is, under the single fluid description for our resistive Ohm's law which determines the electric field $E_z = \eta j_z$, as the resistivity tends to zero its electric field contribution vanishes whereas in the two-fluid model the current density is limited by the electron response time and the change in electric field is determined from the resultant current density.

The second form of the timescale $t$ is best considered at the ablation front where the current density is advected at the ion velocity through terms proportional to **uj** in generalized Ohm's law. First consider the time period $\tau \approx L/u$, over which a current element moves at the ion velocity $u$ a distance $L$ in a plasma where the electric field is increasing as a function of time. When $\tau$ is of order the electron inertia response time scale in 2.27, then the current density of the advected element does not immediately increase to $\sigma E$ as in single fluid MHD. Instead its value is limited by the collision frequency and electron inertial length. We know that the ablation velocity for wire arrays is at least of order 100km $s^{-1}$ for experimentally measurable number densities. If we take a typical length scale for our simulation cell size of 100 microns then tau is of order 1 ns. Electron induction will limit current flow over these timescales and a single fluid model will overestimate the amount of current at the plasma-vacuum interface. The exact amount of overestimation depends upon the collision frequency which is the subject of the next section.

For the above example we have neglected contributions from the Hall term, finite electron pressure, and other additional physics associated with the magnetic field. We now briefly address some of these other terms since the typical ionized background for a wire array experiment will have magnetic fields in the range of 10 to 100 T. Drawing upon the analysis for solutions of generalized Ohm's law in [13], we look at contributions to the current density from the Hall term. It is immediately apparent that magnetic field in the system perpendicular to the driving electric field will cause an $\mathbf{E}\times\mathbf{B}$ drift and that the Hall term will create current densities perpendicular to $j_z$. Solving for the Hall contribution to the current density in the equation

$$\frac{\partial \mathbf{j}}{\partial t} = \frac{L_0^2}{\lambda_{e0}^2} n_e \left( \mathbf{E} - \eta \mathbf{j} - \frac{\lambda_{i0}}{n_e L_0} \mathbf{j} \times \mathbf{B} \right) \tag{2.29}$$

gives solutions where the current density along the applied electric field is limited by electron inertia. For this case the magnitude of the inertially limited current density oscillates between components in the direction of the applied electric field and the transverse Hall direction.

There are two mechanisms by which current flow is limited for low density plasmas in fluid theory. The first mechanism is achieved by increasing the collision frequency and decreasing the current density via resistive effects, and the second mechanism limits current flow by adding finite electron mass, and, thus, charge carrier inertia. Additionally, the kinetic view indicates that for electric fields in excess of the Dreicer limit, electron run away will occur. These electron beams will also limit current flow, but their importance is mainly during the large electric fields of the initiation and implosion phases. If finite electron inertia is limiting current flow in the low density conductive plasma of a pulsed power device, then when fluid theory is applicable a generalized Ohm's law description will be required for self consistency.

## 2.4 Anomalous Collisionality at the Plasma Edge

As discussed in the previous section, the electron drift velocity in conjunction with finite electron inertia can limit the amount of current flowing in conductive regions of order the collisionless skin depth. Near the vacuum-plasma interface of wire array coronal plasmas, the two-fluid model also predicts that the electron drift velocity greatly exceeds the sound speed which is a known to cause

micro-instabilities that artificially increase the electron-ion collision frequency of the plasma [19, 20]. This turbulence may limit the electron drift velocity to a few times the local sound speed [21] reducing the role of electron inertia and electron runaway. Scale lengths of order the electron gyroradius are neglected in our reduced model so direct numerical simulation is not considered. Our model will not include the effects of anomalous collisions, however they are invoked in resistive MHD simulation as a numerical convenience since they smooth the transition in resistivity between the plasma and vacuum regions. Additionally, the enhanced resistivity can prevent thermal runaway in low density regions. For instances in which we compare our generalized Ohm's law model to the resistive MHD model with anomalous collisions, we will invoke the anomalous electron-ion contribution to resistive MHD through modification of the classical collision frequency.

The current density estimation of Equation 2.27 does not consider the role of a parallel magnetic field and under that assumption electrons accelerated by a constant electric field will experience a two-stream instability of ion-acoustic waves [22]. In [23] it is shown that the ratio of the inertial limitation of current density to the anomalous resistivity limiting of current density is of order $\lambda_e^2/(\Delta x)^2$ for ion-acoustic turbulence. As shown previously, the electron inertial length in low density plasma will be larger than scale lengths of interest $\Delta x$. For these reasons, we do not further consider ion-acoustic instability.

The more relevant micro-instability occurs for strong perpendicular magnetic field, and it is suggested that lower-hybrid instability is the source of an anomalously high electron-ion collision frequency [24]. From [24] we see that for the lower-hybrid instability the classical electron-ion collision frequency $\nu_{ei}$

will be increased in proportion to

$$\nu_{ei} \propto \omega_{lh} \left( \frac{u_d}{c_s} \right)^2 \tag{2.30}$$

where $u_d$ is the electron drift velocity, $c_s$ is the local sound speed, and $\omega_{lh}$ is the lower hybrid frequency for low densities and is approximately equal to

$$\omega_{lh}^2 = \Omega_i^2 + \frac{\omega_{pi}^2}{1 + \frac{\omega_{pe}^2}{\Omega_e^2}} \tag{2.31}$$

This anomalous contribution will decrease the plasma conductivity in proportion to the inverse square of the plasma number density, but in reality this form of anomalous collisionality source from [25] is only appropriate for the $T_i >> T_e$ case. Because of the quadratic dependence upon the ratio of the drift velocity to the sound speed this anomalous resistivity is negligible until it switches on as the drift velocity becomes supersonic. It is unknown how far beyond the Spitzer value that the micro-instability will increase the plasma resistivity, so it is possible that the low density plasma could become collisional over pulsed power timescales. We can estimate the maximum electric field supported by anomalous collisions by assuming the electric field energy density is comparable to the thermal energy density. This assumption is reasonable because electric field fluctuations much above the thermal speed will tend to heat the particles and self equilibrate. For the transverse case the maximum electric field is

$$E_z = \sqrt{\frac{2nkT}{\epsilon_0}} \tag{2.32}$$

which for a coronal plasma density of $10^{17}\text{cm}^{-3}$ and a temperature of 10 eV gives an electric field of $2\text{x}10^8\text{V m}^{-1}$ which is reasonable for pulsed power loads.

For experiments where the current rise time is on order of tens of microseconds, such as those described in [26], there is clear evidence from fluctuations in the measured electric field power spectrum that lower hybrid turbulence limits current flow in $10^{12}\text{cm}^{-3}$ hydrogen plasmas. However, for pulsed power on timescale of tens of nanoseconds the collisional nature of the plasma-vacuum interface is uncertain. This is due to inadequate knowledge of the plasma parameters when estimating the exact magnitude of the anomalous resistivity produced by the lower-hybrid instability. Simulations predict that the collisionality increases by a factor of one to a factor of several orders of magnitude [24]. We give two arguments for the case of including the collisionless inertial term with the lower-hybrid instability for the plasma-vacuum interface region in a wire array. The first is that the growth rate of the anomalous collisionality for lower-hybrid turbulence is on the order of the lower hybrid frequency. The response of the electrons for the inertial case is immediate and on a faster timescale governed by the plasma frequency. The second argument is that with the known inertial length of the plasma, we can estimate how much anomalous collisionality is required to overcome inertial effects. At the minimum, three orders of magnitude of increased resistivity beyond the Spitzer value is required which is at the upper limit of estimates for lower-hybrid turbulence at the plasma-vacuum interface.

## 2.5 Charge Carrier Starvation Versus Anomalous Collisions in Limiting Current Flow

In the wire array ablation problem, or for any current carrying flow expanding into a vacuum, the evolution of the current density as the number density tends toward the background level is of extreme importance. The previous two sections have discussed two alternatives compatible with fluid simulation for limiting current flow at the plasma-vacuum interface. We now compare the role of the collisionless electron inertia terms to the collisional lower hybrid instability and determine their relative importance for spatial and time scales associated with pulsed power generated ablation streams. The first difference considered is the reduction in current density as the number density tends towards the background number density of the vacuum chamber. To simplify the discussion let us consider the magnitude reduction in current flow due to electron inertia over a specific time period. Equation 2.27 may be simplified using a Taylor expansion in time $e^t = 1 + t + t^2/2 + ...$ for which under the assumption $\eta t/\mu_0\lambda_e^2 << 1$ Equation 2.27 gives the approximate relation

$$j_z \approx E_z\left(\frac{t}{\mu_0\lambda_e^2}\right) \tag{2.33}$$

The current density dependence on collisions through the plasma resistivity drops out under the expansion assumption. Recasting Equation 2.33 in a form similar to the resistive Ohm's law we find that

$$E_z \approx \eta\left(\frac{1}{n_e}, t\right) j_z \tag{2.34}$$

where the current limitation due to electron inertia over a specified period is dimensionally equivalent to an anomalous resistivity that scales inversely with the electron number density and with time. Using the generalized Ohm's law 2.23 and taking the electron inertial length, ion inertial length, and electron beta to zero, we recover the resistive Ohm's law which ion in the ion frame is just $\mathbf{E} = \eta\mathbf{j}$. We can now compare the ratio of current reduction from inertial effects to that due to enhanced collisionality from wave-particle interaction. From [24] we find the anomalous electron ion-collision frequency from the lower-hybrid micro-instability is

$$\nu_{an} = \frac{1}{2}\sqrt{\frac{\pi}{2}}\omega_{lh}\left(\frac{u_d}{c_s}\right)^2 \tag{2.35}$$

which, when increased, will increase the plasma resistivity proportionately. This relation is shown by considering the momentum contributions to electrons due to ion collisions as approximately [13]

$$\mathbf{R}^e = \eta n_e \mathbf{j} \tag{2.36}$$

then estimating the momentum exchange rate as the number of collisions per cubic meters $\nu_{ei} n_e$ times the mean momentum $m_e n_e (\mathbf{u}_i - \mathbf{u}_e)$. This can be equated to Equation 2.36 to give an order of magnitude estimate for the resistivity as

$$\eta = \frac{m_e \nu_{ei}}{n_e e^2} \tag{2.37}$$

showing that an increase in electron ion collisions will linearly increase the plasma resistivity. Substituting Equation 2.37 into Equation 2.27 says that electron inertia will be the dominate current limitation mechanism over timescales $\Delta t < \nu_{ei}^{-1}$. If we take in to account the increase in collision frequency due to lower-hybrid instability from Equation 2.1 we find that for timescales less than the classical collision frequency

$$\Delta t < \left( \nu_{ei} + \frac{1}{2} \sqrt{\frac{\pi}{2}} \omega_{lh} \left( \frac{u_d}{c_s} \right)^2 \right)^{-1} \tag{2.38}$$

that the magnitude of the magnetic field will also determine the separation between the two regimes. We note that this result is similar to that for current limitation due to ion-acoustic turbulence where spatial scales of interest must be of order the electron inertial length if electron mass is to limit current flow. If we go back to a 10 eV background plasma at number density $10^{12}$ cm$^{-3}$ the classical collision time is of order a microsecond which is much larger than time scales of interest that are of order 1 ns. If we allow the lower hybrid instability to increase the collision frequency without bounds, a 1 T field along with an electron drift velocity to sound speed ratio of order three makes it ambiguous whether collisions take over the role of current limitation. These estimates result in an extreme increase to the collision frequency and requires an anomalous resistivity three orders of magnitude beyond the classical Spitzer estimate. Such large increases have been found in pulsed power experiments whose timescales are in the tens of microseconds. Experiments by Takeda [26] demonstrate anomalous resistivity three thousand times the classical value. Their experiment also gives a lower threshold for the onset of lower-hybrid instability for microsecond pulsed power timescales. In their model lower hybrid instability switches on, without a quadratic buildup, when the Hall velocity exceeds the local sound speed. The condition for instability is $j > c_s n_e e$ which is trivially satisfied for coronal plasma.

Since we can assume the lower hybrid instability is switched on for large portions of the coronal plasma, Equation 2.38 delineates between collisional and collisionless regimes. The total collision time for a 10 eV aluminum plasma is

shown in Figure 2.1 for the combined effects of classical and anomalous collisions due to lower hybrid instability. The contours give the Log10 of the collision time and are plotted over a logarithmic range in number density and magnetic field magnitude. If we assume a gap of 20 mm with the gap voltage near stagnation to be of order 100 kV, then the transit time for an electron is approximately a tenth of a nanosecond. Since it takes a few collisions to establish current flow, we can establish a regime where two-fluid collisionless transport must be considered. For number densities below $10^{17}\text{cm}^{-3}$ we must retain the electron inertia term.

Since some ambiguity exists in the maximum amount that wave-particle interaction can decrease the plasma conductivity, we require additional arguments and numerical experiments to determine the dominate mechanism. Both explanations share the similar scaling as the inverse and square root inverse of the number density but have different time dependence. For electron inertia, as the time increases, one approaches the asymptotic solution of resistive Ohm's law and thus dependence upon anomalous collisionality for limitation of current flow. For the lower-hybrid instability we have the spatial and temporal dependence upon the lower hybrid frequency which is due to magnetic field.

Another key difference between the collisional and collisionless current limitation mechanisms is in the Joule heating rate at the plasma-vacuum interface. The energy partition will differ between the two mechanisms. We can compare the contributions to the energy partition from micro-instability and classical collisions given by

$$T_e \approx (\gamma - 1) \int_0^{t_f} \frac{m_e \left(\nu_{ei} + \nu_{ei}^*\right)}{e^2 n_e^2} j^2 dt \tag{2.39}$$

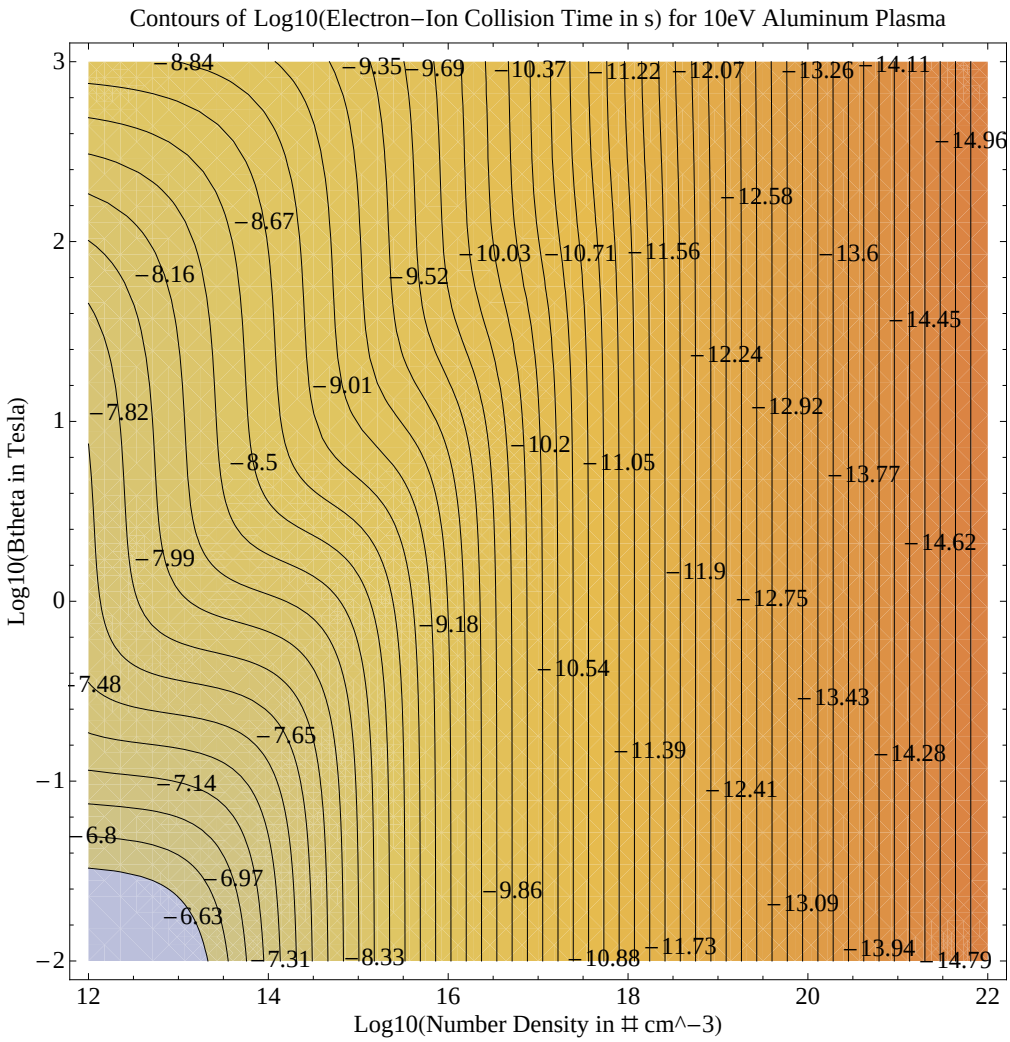


Figure 2.1: Electron-ion collision time calculated from classical electron ion frequency plus anomalous lower-hybrid collisions for aluminum plasma at 10 eV.

to that of the Hall kinetic energy and Joule heating.

$$KE_{hall} + \frac{n_e T_e}{(\gamma - 1)} \approx \frac{\rho_e V_h^2 j^2}{2} + \int_0^{t_f} \eta_{Spitzer} j^2 dt \tag{2.40}$$

For the collisionless current limitation case, the large drift velocity will result in kinetic energy associated with the Hall velocity and Joule heating at a rate determined by the classical Spitzer resistivity. For the lower-hybrid micro-instability

the plasma edge will experience Joule heating two to three orders magnitude larger than inertial current limiting. The increase in collision frequency will also drive the ion and electron temperatures more quickly into equilibrium, extending the density range of the single temperature approximation. The dominance of each mechanism determines the partition of energy density between the axially directed Hall kinetic energy and the isotropic pressure from Joule heating.

In addition to the differences in energy, the anomalous resistivity will also modify the coupling of the flow with the magnetic field through diffusion. This issue will be addressed in Chapter 5. These results suggest that numerical experiment with a code capable of solving generalized Ohm's law is necessary in understanding which mechanism, electron inertia or anomalous resistivity, is dominant and what role the difference between each mechanism's heating rates will play in the low density coronal plasma and thus in the overall ablation dynamics. In the next chapter we will show how the generalized Ohm's law model can be numerically solved for the wire array problem along with the numerical benefits of including electron inertia.

CHAPTER 3

# A SEMI-IMPLICIT RELAXATION SCHEME FOR THE GENERALIZED OHM'S LAW-MAXWELL SYSTEM

Numerical simulation of pulsed power loads such as wire arrays, solid liners, and X-pinches is a daunting task due to the extreme range of physical parameters and uncertainty in transport coefficients that define the system. Typically these systems have mega-amps of current carried by densities ranging over more than eight orders of magnitude. The large range of current carrying densities implies that the single fluid model will break down on scale lengths of order the ion inertial length and below. There is clearly a need to numerically explore the two-fluid regime of pulsed power flows, but the applicability of existing numerical methods in this plasma regime is limited by stringent requirements on grid resolution and time step.

A full treatment of the two-fluid plasma model where displacement current is neglected requires resolving the electron plasma frequency, which for an explicit treatment of wire array flows equates to time-steps on the order of femtoseconds for numerical stability. In this formulation the two-fluid model also requires the solution of Poisson's equation for the electric field, which imposes a grid spacing requirement of resolving the Debye length which is in the nanometer range [27]. Since the system of interest is characterized by timescales of order 100 ns and lengths scales of order 10 mm, a formulation of the two-fluid equations without displacement current is out of the range of practical computation. In the following sections we describe a numerical formulation for the generalized Ohm's law simplification of the two fluid model that bypasses the Debye length grid spacing requirement, makes the plasma frequency amenable to im-

plicit integration, and retains the physics of two distinct species.

## 3.1 Numerical Solution Method

Before describing our algorithm to numerically integrate the generalized Ohm's law description of plasma dynamics, we briefly review numerical methods developed to address the complete two-fluid plasma system. In [28] a Roe type Riemann solver is developed for the full two-fluid system of equations. This allows for the development of high resolution Eulerian schemes based on Godonov's method under both Finite Volume [29] and Discontinuous Galerkin [30] discretization. Additionally, the two-fluid system is solved in [31] using Finite Elements. For fluid descriptions beyond the single fluid model, the main focus has been on either numerically solving the two-fluid model with separate species equations or using a reduced center-of-mass approximation where two-fluid effects such as Hall MHD [32] are contained within the induction equation.

Instead of these approaches, we explore the solution of an intermediate model in the center-of-mass frame where terms of order $m_e/m_i$ have been neglected, quasi-neutrality is not assumed, and electron inertia is retained. The analytic model for this system is derived in Chapter 2, and allows us to limit current flow in the background plasma via the electron inertia term without advancing the full electron equation of motion. This will bypass time and length scale restrictions associated with finite electron pressure.

### 3.1.1 Conservation Laws

Equations 2.20 through 2.25 along with Maxwell's equations form a system of conservation laws with source terms. We define the vector of conservation variables $\mathbf{U} = [\rho, \rho\mathbf{u}, \epsilon, \mathbf{j}, \mathbf{E}, \mathbf{B}]$ whose evolution is described by Equation 3.1 with $\mathbf{F}$ defined as the flux tensor and $\mathbf{S}$ defined as the sources. The evolution of the system of conservation laws is described by

$$\frac{\partial \mathbf{U}}{\partial t} + \nabla \cdot \mathbf{F}_h(\mathbf{U}) = \mathbf{S} \tag{3.1}$$

where the flux tensor $\mathbf{F}$ is assumed to be hyperbolic. The numerical solution of systems of hyperbolic conservation laws is a well studied problem [33], and we will take the approach of the Finite Volume method. In particular, we will consider the use of high-resolution schemes [34] to advance the solution of the partial differential equations in time. These shock-capturing methods have the property of being total variation diminishing (TVD), a desirable property for stable integration of conservation laws. The volume averaged conservation variable defined over the grid interval $x \in \left[x_{i-\frac{1}{2}}, x_{i+\frac{1}{2}}\right]$ is given by the expression $\bar{U}_i^n = \frac{1}{\Delta x}\int_{x_{i-\frac{1}{2}}}^{x_{i+\frac{1}{2}}} U(x, t_n)\, dx$. Using the divergence theorem to integrate over the system given by Equation 3.1, each cell average can be updated to a first order estimate of the next time level $n+1$ through the expression

$$\bar{U}_i^{n+1} = \bar{U}_i^n - \frac{\Delta t}{\Delta x}\left(F_{i+1/2}^n - F_{i-1/2}^n\right) \tag{3.2}$$

where the flux at each face of the cell $F_{i\pm1/2}^n$ is determined from the solution to the Riemann problem at each interface. This method of advancing the equations is known as Godunov's method [35] and will form the basis for our high resolution scheme. Two complications arise in applying this method to the generalized Ohm's law system. The first is that we require an approximate Riemann

solver for the reduced center-of-mass system to accurately determine the flux function. Such a solver exists for the non-center-of-mass formulation where the separate ion and electron continuity, current density, and total energy equations form the two-fluid system [28]. The solution method described in [28] is only stable for time-steps less than the minimum of $\omega_{pe}^{-1}$ and $\Delta x\, c^{-1}$. This is true even if the stiff source terms are implicitly advanced. As mentioned previously, for simulating problems over wire array time scales this time-step requirement makes computation of the wire ablation process unfeasible. This form of the evolutionary equations also makes determining physical origin of phenomena difficult as compared to a center-of-mass generalized Ohm's law formulation. Also, even in the simplest case of a Roe type solver, there is a large computational expense due to solving the Riemann problem over each cell interface.

We look to an alternative method to determine the flux at the cell interface when forcing source terms are present. The previously mentioned length and timescale problems are addressed through calculating the fluxes with the relaxation method of Jin and Xin [36]. We extend this method to the generalized Ohm's law system, the details of which will be described in the following section. The second complication is in extending the method to higher order accuracy. Godunov's method considers the conservation variables as piecewise constant over each cell and is first order in space. For practical computation, at least second order accuracy is required. We use van Leer's monotone upwind scheme for conservation laws (MUSCL) [37] where piecewise linear approximations to cell quantities along with flux limiting will provide monotone, second order accurate answers where the solution is smooth. The MUSCL scheme and a yet to be described treatment of the stiff source terms forms the numerical basis for solution of the GOL system. Before we discuss the general solution method

of the Relaxation scheme we first address the inclusion of displacement current in the model and how it benefits the numerical character of our conservation laws.

### 3.1.2 Displacement Current and the Boris Correction

The neglect of displacement current from Maxwell's equations is a common approximation in the description of plasma where the radiation pressure is much less than the gas pressure. The result is to remove light waves from the system which removes the explicit stability condition of resolving the transit time of an electromagnetic wave across the cell. Since the bulk flows are expected to not be relativistic and the contribution from radiation pressure is negligible for the wire array problem the approximation is valid. The effect of removing displacement current is to change the relationship between current density and the magnetic field. When neglecting displacement current as an approximation to the Maxwell system, the magnetic field is updated through an induction equation where the electric field from Ohm's law is substituted into Faraday's equation and the current density is determined from the curl of the magnetic field. The result of this approximation is that the induction equation contains parabolic and dispersive terms when collisions and two-fluid physics are included. We now show why it is advantageous to maintain the hyperbolicity of the conservation system by keeping displacement current for the two-fluid system.

First we consider the resistive MHD case where a parabolic induction equation is implicitly updated due to the stringent explicit time-step limitation of

$\Delta t < \Delta x^2/D_{max}$ where $\Delta t$ is the time-step, $\Delta x$ is the grid spacing, and $D_{max}$ is the maximum value of the diffusion coefficient equal to the plasma resistivity divided by the magnetic constant. In the resistive MHD model a large diffusion coefficient, typically of order $10^4$ to $10^6$, is required to keep current from flowing in the numerical vacuum region and to propagate the magnetic field from the boundary to the plasma. This will require a small time-step, which can be more stringent than the hyperbolic speed of light time-step limitation. Computation in this case is only practical if implicit time-stepping is considered. The backward Euler solution of the magnetic field from the linearized resistive induction equation is

$$\frac{\mathbf{B}^{n+1}}{\Delta t} + \nabla \times (\eta \nabla \times \mathbf{B}^{n+1}) = \frac{\mathbf{B}^{n}}{\Delta t} + \mathbf{rhs}^{n} \tag{3.3}$$

whose linear operator is of curl-curl form. Efficient iterative solution of this particular PDE operator is difficult due to the large null space and the highly discontinuous nature of the diffusion coefficient when the vacuum resistivity model is used. A highly convergent solution of the analogous curl-curl operator for the eddy current approximation is possible when compatible discretization is employed along with an algebraic multi-grid solution method [38]. For practical 3D computation of the wire-array problem this forces the use of algebraic-multigrid (AMG) solvers in a massively parallel environment which will limit the scalability of any resultant algorithm. Additionally, it is not clear how to extend this method to other solution spaces such as the Finite Volume method.

In [39] the complication of implicit solution of the induction equation is removed by including displacement current in the resistive MHD model. The speed of light for the resistive MHD with displacement current system is reduced to 10 times the fastest information velocity determined from either the Alfven speed or flow velocity. This approach is similar to that of the Boris [40]

where the full contribution of displacement current to the momentum equation is also included and the system retains its hyperbolic nature.

We now consider the two-fluid case where electron inertia is limiting the current flow at the plasma-vacuum interface. Under the neglect of displacement current the two-fluid induction equation is formed by taking the curl of the generalized Ohm's law and rewriting the time derivative of the current density in terms of the magnetic field. The implicit advance for the electron inertia physics has a linear operator of the form 3.3 whose coefficient scales inversely with the number density. The same complications of a curl-curl operator with nearly discontinuous coefficient appear in the two-fluid induction equation.

$$\mathbf{B}^{n+1} + \nabla \times (\lambda_e^2 \nabla \times \mathbf{B}^{n+1}) = \mathbf{B}^n + \nabla \times (\lambda_e^2 \nabla \times \mathbf{B}^n) - \Delta t \nabla \times (\eta \nabla \times \mathbf{B}^n) + \Delta t \mathbf{rhs}^n \quad (3.4)$$

When displacement current is retained, the time evolution of the current density is found from the generalized Ohm's law Equation 2.23 and the spatially coupled stiffness of the curl-curl operator is transformed to the local stiffness of the plasma frequency in the source term of 2.23. We take this approach to advance the GOL-Maxwell system as the implicit integration of the stiff source term is straightforward and requires no massively parallel linear algebra. We expect the scalability of such a code to be similar to that of other domain decomposed purely explicit methods [41].

## 3.2 The Relaxation Method Applied to the Two-Fluid Plasma Approximation

The semi-discrete relaxation method of Jin and Xin [36] is a Riemann solver free approach that has been successfully applied to conservation systems including problems of hydrodynamic [42] and ideal magnetohydrodynamic evolution [43]. This method has the desirable property that hyperbolic problems with stiff source terms can be consistently treated. The main advantage of this method is its ability to transform a nonlinear advection system

$$\frac{\partial U}{\partial t} + \frac{\partial f(U)}{\partial x} = 0 \tag{3.5}$$

into a pair of linear equations describing the evolution of the conservation variables in terms of an auxiliary vector

$$\frac{\partial U}{\partial t} + \frac{\partial V}{\partial x} = 0 \tag{3.6}$$

and an equation describing the evolution of the auxiliary vector in terms of the conservation variable with stiff source term. We assume 1D for simplicity. The generalization to higher dimensions is straight-forward.

$$\frac{\partial V}{\partial t} + c^2 \frac{\partial U}{\partial x} = -\frac{1}{\epsilon}(V - f(U)) \tag{3.7}$$

In the limit that the relaxation parameter $\epsilon$ goes to zero the original conservation system is recovered. This has the effect of linearizing the Riemann problem

in a "blackbox" manner for a given set of conservation laws provided that the sub-characteristic condition

$$\frac{max(f'(U)^2)}{c^2} \leq 1 \qquad \forall U \tag{3.8}$$

is satisfied, where $c^2$ is a diagonal matrix of freezing speeds that are greater than the maximum eigenvalue of the flux Jacobian. The flux Jacobian is the Jacobian matrix for the linearized hyperbolic fluxes $\mathbf{F}$ in our conservation system. We use the "relaxed" limit given in [36] in which we assume that $\epsilon$ is zero and the relationship between the auxiliary vector and the conservation variables is $V \approx f(U)/c$. The end result is that the relaxed limit gives us an approximation for the left and right going waves in the system. The right moving flow is determined from

$$U_R = \frac{1}{2}(U + V) \tag{3.9}$$

and the left moving flow is determined from

$$U_L = \frac{1}{2}(U - V) \tag{3.10}$$

which when substituted in to the coupled conservation-auxiliary variable Equations 3.6-3.7 transforms the conservation system in to linear advection equations where the upwind direction is known from

$$\frac{\partial U_R}{\partial t} + \frac{\partial (cU_R)}{\partial x} = 0 \tag{3.11}$$

$$\frac{\partial U_L}{\partial t} - \frac{\partial (cU_L)}{\partial x} = 0 \tag{3.12}$$

where Equations 3.11- 3.12 are right and left advection equations at speed c, and $f(U_R) = cU_R$ and $f(U_L) = cU_L$. Since $U = U_R + U_L$, adding Equations 3.11-3.12 gives

$$\frac{\partial U}{\partial t} + \frac{\partial f(U_R)}{\partial x} - \frac{\partial f(U_L)}{\partial x} = 0 \tag{3.13}$$

which is the combined advection system.

Since the upwind directions are known, the system of conservation laws is advanced with the TVD-MUSCL method described in [42]. This method is revisited for the convenience of the reader in the next section. Unlike [43] we advance the equations in a dimensionally unsplit manner which requires a more stringent sub-characteristic condition in two dimensions that $\frac{f'(U)^2}{c^2} + \frac{g'(U)^2}{c^2} \leq 1$ where g describes the y component of the fluxes. To accurately evolve the magnetic field, it is essential that dimensionally unsplit integration is performed when the solenoidal nature of **B** is preserved by the constrained transport method [44] discussed in the next section.

We extend the use of this method to the generalized Ohm's law Maxwell system of Equations 2.20 - 2.25 in a two-dimensional Cartesian coordinate system. The extension of the relaxation method to the subset of equations in the two-fluid system, corresponding to those of compressible gas dynamics, Maxwell's equations, and the generalized Ohm's law is discussed in the following sections. Finally the derivation of an implicit integration over the electron inertia and Hall terms is discussed along with the boundary conditions.

### 3.2.1 Review of MUSCL-Relaxation Schemes for Conservation Laws

For the readers convenience, we revisit the analysis and explanation of TVD-MUSCL-relaxation schemes given in [42]. When time advancing hyperbolic partial differential equations, it is desirable that our numerical scheme is total variation diminishing (TVD). We use the indexing of [42] where the volume averaged conservation variables are located at cell $U_i$ and the fluxes are located at $f_{i+1/2}$. For our finite volume representation of the conserved variables $U_i$, the time advance is given by

$$U_i^{n+1} = U_i^n - \frac{\Delta x}{\Delta t}\left(f_{i+\frac{1}{2}}^{n+\frac{1}{2}} - f_{i-\frac{1}{2}}^{n+\frac{1}{2}}\right) \tag{3.14}$$

and we want estimates of $f_{i\pm\frac{1}{2}}^{n+\frac{1}{2}}$ such that $U$ at the next time level, $n+1$, is free from spurious oscillation. For our model equation 3.5, the total variation $T_V$ of the discrete form of the solution $U$ is given by

$$T_V = \Sigma_i |U_{i+1} - U_i| \tag{3.15}$$

which gives a metric for the number of oscillations in the solution. Differencing of hyperbolic systems of equations can give rise to nonphysical oscillations in the discrete solution, so it is desirable to keep the total variation of the solution at the advanced time level equal to or less than the total variation of the current time level. This property prevents the creation of local extrema and allows for the stable integration of hyperbolic systems. Given the "upwind" direction of the flow, a first order accurate estimate of the flux in this direction is TVD. For a predictor-corrector time advance, the first order estimate of the right moving flux $f_{i+1/2}^{R,1st}$ is

$$f_{i+\frac{1}{2}}^{R,1st} = (f(U) + cU)_i \tag{3.16}$$

and the first order estimate of the left moving flux $f^{L,1st}_{i+1/2}$ is given by

$$f^{L,1st}_{i+\frac{1}{2}} = (f(U) - cU)_{i+1} \tag{3.17}$$

With the first order fluxes known, a first order monotone time advance of our conservation system to the predictor time level is given by

$$U^{n+\frac{1}{2}}_i = U^n_i - \frac{\Delta t}{2\Delta x}\left(f^n_{i+\frac{1}{2}} - f^n_{i-\frac{1}{2}}\right) \tag{3.18}$$

where we have used the definition that $f^n_{i+\frac{1}{2}} = \frac{1}{2}\left[f^{R,1st}_{i+1/2}(U^n) - f^{L,1st}_{i+1/2}(U^n)\right]$. This scheme is too diffusive to advance our equations, so a second order correction to the flux is required. A linear second order correction to the upwind flux can be constructed from $\Delta f^{n+1/2}_{i+\frac{1}{2}}\left(U^{n+\frac{1}{2}}_i\right)$ which when added to the first order fluxes at the n+1/2 time level gives $f^{n+\frac{1}{2}}_{i+\frac{1}{2}}$. We now derive the non-TVD and TVD estimates of $f^{n+\frac{1}{2}}_{i+\frac{1}{2}}$ which along with Equation 3.14 will allow us to time advance the system. The total second order flux for the right moving waves is found from adding the first order right moving flux $f^{R,1st}_{i+1/2}$ at the n+1/2 time level to the second order correction given by

$$\Delta f^{R,2nd}_{i+\frac{1}{2}} = \frac{1}{2}\left(f^R_{i+\frac{3}{2}} - f^R_{i+\frac{1}{2}}\right) \tag{3.19}$$

and for left going waves we add $f^{L,1st}_{i+1/2}$ at the n+1/2 time level to the second order correction

$$\Delta f^{L,2nd}_{i+\frac{1}{2}} = \frac{1}{2}\left(f^L_{i+\frac{1}{2}} - f^L_{i-\frac{1}{2}}\right) \tag{3.20}$$

which results in a fully second order estimate of the fluxes. If this scheme is used to advance a hyperbolic system, unwanted oscillations in the solution will occur. According to Godunov's Theorem [35], linear schemes which are monotone can be at most first order accurate. Unfortunately, the desired TVD property is in conflict with the need for second order convergence of the solution. The MUSCL scheme provides a solution to the conflict between stability and

accuracy through the use of non-linear flux limiters. The flux limiter lets us interpolate the flux approximation through a combination of the first and second order corrections. First we define the flux ratio $r$

$$r_{i+\frac{1}{2}} = \frac{\Delta f^{L,2nd}_{i+\frac{1}{2}}}{\Delta f^{R,2nd}_{i+\frac{1}{2}}} \tag{3.21}$$

which is the ratio of the left and right going second order flux corrections. We now define a flux limiter function $\Phi(r)$ which will nonlinearly interpolate between our first order flux approximation which is TVD for all regions and our second order flux approximation which is stable for smooth regions. For the problems explored in this thesis, we use the superbee flux limiter [45] and the van Leer flux limiter. The van Leer flux limiter is given by

$$\Phi(r) = \frac{2r}{r+1} \tag{3.22}$$

which performs well for problems explored in this thesis. However, the superbee limiter appears superior in most cases. Given the flux ratio $r$ and the flux limiter function $\Phi(r)$ the TVD flux $\bar{\Delta f}^{2nd}_{i+\frac{1}{2}}$ at the cell interfaces is found by the formula

$$\bar{\Delta f}^{2nd}_{i+\frac{1}{2}} = \Phi\left(r_{i+\frac{1}{2}}\right) \Delta f^{2nd}_{i+\frac{1}{2}} \tag{3.23}$$

where f can be either the right going fluxes or left going fluxes. The TVD final right going fluxes and final left going fluxes can now be found by adding the first order flux estimates $f^{1st}_{i+1/2}$ at the predictor time level n+1/2 to the TVD second order flux estimates $\bar{\Delta f}^{2nd}_{i+\frac{1}{2}}$ at the predictor time level. This is performed for both the left and right going wave cases and the final second order TVD total flux $f^{n+\frac{1}{2}}_{i+\frac{1}{2}}$ is found by subtracting the final right moving flux estimate from the final left moving flux estimate. Equation 3.14 may then be used to advance the system to the next time level. The overall scheme is second order in time and

second order in space for smooth solutions. In the following sections we will derive the sub-characteristic constraint c and special numerical techniques needed in addition to the TVD time advance of the generalized Ohm's law system.

### 3.2.2 Maxwell's Equations

As discussed in section 3.1.2 it is advantageous to keep displacement current and evolve the full Maxwell system in step with the gas dynamics and generalized Ohm's law. This approach is formulated under the relaxation scheme in terms of a two-dimensional conservation system where for this example we just consider the evolution of the transverse electric mode in non dimensional form given by

$$\frac{\partial U_m}{\partial t} + \frac{\partial f(U_m)}{\partial x} + \frac{\partial g(U_m)}{\partial y} = S(U_m) \tag{3.24}$$

along with the field variables to integrate,

$$U_m = \left[E_z, B_x, B_y\right] \tag{3.25}$$

the flux function for derivatives with respect to the x dimension,

$$f(U_m) = \left[\left(-\frac{c}{V_{a0}}\right)^2 B_y, 0, -E_z\right] \tag{3.26}$$

the flux function for derivatives with respect to the y dimension,

$$g(U_m) = \left[\left(\frac{c}{V_{a0}}\right)^2 B_x, E_z, 0\right] \tag{3.27}$$

and finally the source terms

$$S(U_m) = \left[\left(-\frac{c}{V_{a0}}\right)^2 j_z, 0, 0\right] \tag{3.28}$$

which gives Maxwell's equations in the form of a conservation system. Ampere's law along with Faraday's law in the corresponding form can be evolved

with the TVD-MUSCL relaxation method described in the previous section given that the sub-characteristic condition is satisfied by setting the freezing speed to maximum eigenvalue of the flux Jacobian, which for this system of equations is the speed of light.

Additional constraints exist in the Maxwell system, most notably that the magnetic field is solenoidal or $\nabla \cdot \mathbf{B} = 0$. This constraint is not automatically satisfied by the relaxation system, and as such divergence errors will accumulate in time. The importance of keeping the magnetic field divergence free is noted by Toth [46] where it is shown divergence errors will lead to anomalous flows along the magnetic field and to numeric instability. When Maxwell's equations coupling with gas dynamics and generalized Ohm's law is considered, one finds that the current density source term of Ampere's law is the only way in which information is passed into Maxwell's equations. Thus, it is advantageous to only determine the evolution of the magnetic field from Faraday's law as a surface integral of the electric field. In this manner the magnetic field may be updated such that given an initially divergence free field, the magnetic field will remain divergence free, to the extent that roundoff error allows, over all time. In typical MHD codes where an induction equation is advanced, this leads to staggering of the electric and magnetic fields such that the magnetic field remains solenoidal when updated from the line integral of $\mathbf{E} \cdot dl$. For simplicity we apply the cell centered Flux-CT scheme of [46] to the Maxwell equations time advance.

$$B_x^{n+1}(i,j) = B_x^n(i,j) - \frac{\Delta t}{\Delta y}\left[E_{z^*}^{n+1/2}(i,j+1) - E_{z^*}^{n+1/2}(i,j-1)\right] \tag{3.29}$$

$$B_y^{n+1}(i,j) = B_y^n(i,j) + \frac{\Delta t}{\Delta x}\left[E_{z^*}^{n+1/2}(i+1,j) - E_{z^*}^{n+1/2}(i-1,j)\right] \tag{3.30}$$

where the electric field $E_{z^*}$ is determined from the cell averaged 2nd order accu-

rate relaxation flux in Faraday's law at the $n+1/2$ time level. The electric field $E_{z^*}$ used to update the magnetic field is averaged around each of its cell neighbors through the upwind fluxes $\bar{f}$ and $\bar{g}$, this found from

$$E_{z^*}^{n+1/2}(i,j) = \frac{1}{4}\left[-\bar{f}\left(B_y^{n+1}(i-1,j)\right) - \bar{f}\left(B_y^{n+1}(i,j)\right) + \bar{g}\left(B_x^{n+1}(i,j-1)\right) + \bar{g}\left(B_x^{n+1}(i,j)\right)\right] \tag{3.31}$$

and in this manner the line integral is calculated over the cell centers of the three cell by three cell block centered on the updated field at grid location (i,j). This averaging allows for a constrained transport update based on cell centered fields that preserves the divergence of the magnetic field in full Maxwell's equations in a manner similar to the algorithm applied to the induction equation in [46].

### 3.2.3 Compressible Gas Dynamics

We now discuss specific issues for the numerical solution of the hyperbolic fluxes of the continuity, momentum, and energy density equations of an inviscid ideal ionized gas in the wire array parameter regime. The general treatment for the ionized gas dynamic equations in a relaxation scheme is given in [43], and we discuss modifications to the algorithm that allow for computation in the wire array parameter regime. Since the role of viscosity is assumed minimal from estimation from typical plasma parameters and the neglect of boundary layer flow, the viscosity closure for the gas dynamic system is instead replaced by the entropy closure of the conservation system. Formally, this is performed by using a numerical method that will produce the correct entropy state when the equations of continuity, momentum, and total energy are advanced in time.

Since all three of these quantities are conserved over the discontinuity formed by the under-resolved viscous scale length of the shock, the correct jump conditions will exist in the numerical system and the resultant shock speeds will be calculated.

Because we have included displacement current, the jump conditions are considered for each individual species. For generalized Ohm's law with an induction equation the shock interface conserves the total energy

$$W = \frac{B^2}{2\mu_0} + \frac{m_e j^2}{2n_e e^2} + \frac{\rho u^2}{2} + \frac{P}{\gamma - 1} \tag{3.32}$$

which is the sum of the magnetic energy density, the electron kinetic energy, the ion kinetic energy, and the internal energy density. For this formulation, the pressure is determined from the total energy equation which for low beta plasmas involves the subtraction of two large numbers. This results in small negative pressures and must be handled through methods such as those discussed in [47] which evolve both an entropy density and total energy equation.

The inclusion of displacement current poses the evolutionary equations in terms of coupled ion and electron Euler equations and the electromagnetic energy no long directly plays a role in the numerical determination of the correct entropy state. All that is required is to satisfy the entropy condition for the ion fluid when evolving the gas dynamics. As a simplification, instead of the internal energy density equation we evolve the entropy density of the system, which along with the ideal equation of state is used to determine the plasma pressure. Since the entropy is not conserved over the shock interface, this will lead to incorrect shock speeds. We apply the entropy density equation to the conservation system noting that numerical experiment conducted with the code gives shock speed errors of order ten percent.

The second approximation made in the system is due to the inclusion of displacement current in the model and the fact that the current density is derived from the generalized Ohm's law. For the two-fluid system of equations the hyperbolic flux is only calculated for the fluid stress tensors of each species and the Lorentz force contribution is due to source terms of the conservation system. In the center-of-mass formulation for the GOL system, a more exact momentum equation, analogous to the full two-fluid system, is

$$\frac{\partial \rho \mathbf{u}}{\partial t} + \nabla \cdot \left[ \rho \mathbf{u}\mathbf{u} + \left( \frac{\lambda_{e0}}{L_0} \right)^2 \frac{\mathbf{j}\mathbf{j}}{n} + \mathbf{I}(\beta P) \right] = \rho_c \mathbf{E} + \mathbf{j} \times \mathbf{B} \tag{3.33}$$

and for regimes of interest in pulsed power we can directly neglect terms of order $m_e/m_i$ and the momentum contributions due to free charge and displacement current. We keep the magnetic and embedded displacement current contribution of the Lorentz force as a source term but neglect the electrostatic contribution.

The relaxation algorithm requires an estimate of the maximum eigenvalue of the flux Jacobian for the system to satisfy the sub-characteristic constraint and thus guarantee its TVD nature. For the equations involving the evolution of the ion gas dynamics, this value can be derived and is given by the maximum of the ion velocity plus the sound speed and the hall velocity plus the ion velocity. If electron self advection is included, as in 3.33, then the sub-characteristic condition is

$$c_{fr} = max \left[ \left| v_x \pm c_s \right|, \left| v_x \mp \frac{j_x}{e n_e} \right| \right] \tag{3.34}$$

which only differs from the full two-fluid eigenvalues through the neglect of the electron thermal velocity. Equation 3.34 will serve as the freezing speed for the mass continuity, ion momentum, and entropy density equations to satisfy the sub-characteristic condition for the relaxation system. We find that it

is important to use a separate freezing speed for each cell instead of the global maximum. This minimizes the artificial diffusion in the scheme which is especially important for wire array systems where the minimum and maximum wave speeds can vary by orders of magnitude.

The corresponding time step will be determined from decreasing the speed of light to a few times the fastest wave traveling in each cell of the system under the Boris correction. If we do not consider the role of the Hall term, then the fastest wave will typically be the fast wave velocity modified by electron inertia in the fluid frame which has for its phase velocity

$$\frac{\omega}{k} = \sqrt{c_s^2 + \frac{V_a^2}{1 + k^2 \lambda_e^2}} \tag{3.35}$$

In the next section, the evolutionary equation for electrons is considered.

### 3.2.4 Ohm's Law

When displacement current and electron inertia are included, Ohm's law plays the role of determining the time evolution of the current density. This is in stark contrast to any code using a lower order approximation such as Hall MHD, where higher order derivatives result from the electric field being determined from Ohm's law which is then substituted into Faraday's law which determines the evolution of the magnetic field and from its curl the current density. The numerical solution of two-fluid physics in the induction equation framework is of considerable interest to the plasma physics community, and implicit techniques for integrating these systems poses significant challenges [48, 49]. Instead of addressing the implicit integration of a non-linear operator equation containing dispersive derivatives we numerically integrate the system without making

the standard approximation of neglecting the electron inertia term and displacement current. The result is the GOL of Equation 2.23 which only contains first derivatives and a stiff source term. For this equation the flux corresponds to the electron stress tensor which plays the role of advecting current on scale lengths of order the electron inertial length.

As we have previously shown the time derivative on the current density will retard the growth of current in a plasma where the timescales are less than the inverse of the collision frequency. The hyperbolic fluxes associated with flow of electrons are advanced with the relaxation scheme in the presence of the source terms which scale with the plasma frequency. Since these terms would limit explicit integration of the system to the inverse of the plasma frequency we will implicitly integrate them.

Before approaching the implicit integration of the source terms, the appropriate sub-characteristic condition for the current density flux is required. We also must know which plasma waves exist in the system so that the speed of light can be reduced accordingly. The sub-characteristic condition depends upon the fastest speed at which information can propagate in a cell for the hyperbolic part of the electron equation of motion, Equation 2.23. The relaxation scheme only provides the sub-characteristic based on the flux Jacobian, not the maximum phase speed for each equation in the conservation system. For the full two-fluid system this corresponds to the eigenvalues of the Euler equation for electrons. For the electron fluid velocity $V_e$ and electron thermal velocity $V_{the}$ the eigenvalues are $\lambda_{electron} = [V_e, V_e \pm V_{the}]$. The generalized Ohm's law model is in the center-of-mass frame and we have neglected the role of electron pressure and electron self advection. This leaves only terms which transport current den-

sity at the ion fluid velocity. The sub-characteristic condition is then satisfied for reconstruction at the absolute value of the center-of-mass fluid velocity **u**.

## 3.3 Linear Two-Fluid Dispersion Relations

We now wish to understand the linear propagation of waves in the reduced model. This will allow us to lower the speed of light in a stable manner. For the general case of a warm low beta plasma that also considers the source terms, we turn to Stringer's dispersion relation [50] for the two-fluid system,

$$\left[\left(\frac{\omega}{k}\right)^4 - \left(\frac{w}{k}\right)^2\left(\frac{c_s^2+V_a^2}{1+k^2\lambda_e^2}\right) + c_s^2\left(\frac{V_a^2}{1_k^2\lambda_e^2}\right)\cos^2\theta\right] * \left[\left(\frac{\omega}{k}\right)^2 - \left(\frac{V_a^2}{1+k^2\lambda_e^2}\right)\cos^2\theta\right] - \left[\frac{V_a^2\omega}{\Omega_i\left(1+k^2V_a^2\right)}\right]^2\left[\frac{\omega^2}{k^2} - c_s^2\right]\cos\theta = 0 \tag{3.36}$$

where $\theta$ is the angle between the wave propagation vector and the magnetic field. The global maximum phase velocity for the roots of this dispersion relation are required, and we first consider the parallel propagation case where $\cos\theta = 0$. The roots of interest determined from symbolic numeric solution are

$$\omega = \pm\frac{1}{2}\frac{\left[k^2V_a^2+2\left(1+k^2\lambda_e^2\right)\Omega_{pi}^2 \pm \left(k^2V_a^2+4\left[1+k^2\lambda_e^2\right]\Omega_{pi}^2\right)^{\frac{1}{2}}kV_a\right]^{\frac{1}{2}}2^{\frac{1}{2}}kV_a}{\left(1+k^2\lambda_e^2\right)\Omega_{pi}}, \pm c_s k \tag{3.37}$$

and for propagation across the magnetic field with $\cos\theta = 1$ the roots of interest are given by the electron inertia modification to the fast wave seen in Equation 3.35. We may stably integrate the generalized Ohm's law Maxwell system if

pick a speed of light that is a few times the maximum predicted group velocity for these waves in our experiment.

These roots also demonstrate the benefit of including electron inertia. The beneficial contribution of electron mass in a low $\beta_e$ plasma is found from the term $1 + k^2\lambda_e^2$. The electron inertia provides resonances for propagation both perpendicular and parallel to the magnetic field. This results in the whistler wave resonance at the electron cyclotron frequency and the fast wave rollover to the lower hybrid frequency. In both cases the phase velocities are significantly lower when electron inertia is included. If we neglected terms of order the electron inertial length considered the Hall, the whistler mode would increase without bounds with phase velocity

$$\frac{\omega}{k} = \frac{kV_a^2}{\Omega_i} \tag{3.38}$$

giving an overall scaling proportional to the grid spacing squared $\Delta t \propto \Delta x^2$. This means that the shortest waves propagating in our system have the highest phase velocity which can lead to numerical instability. For the generalized Ohm's law of 2.23 electron inertia limits the frequency to the electron cyclotron frequency for parallel propagation.

The advantage of this formulation is slower wave velocities and lower order derivatives. This formulation introduces stiff source terms associated with the electron plasma frequency and the electron cyclotron frequency. This allows us to implicitly integrate over these two timescales while still resolving the whistler wave for our wave numbers of interest. Dimensionally, the source terms for generalized Ohm's law 2.23 along with Ampere's law can be considered under the approximate system

$$\frac{\partial \mathbf{j}}{\partial t} \approxeq \omega_{pe}^2 \epsilon_0 \left(\mathbf{E} - \eta \mathbf{j}\right) - \mathbf{j} \times \mathbf{\Omega_e} \tag{3.39}$$

$$\frac{\partial \mathbf{E}}{\partial t} \approxeq \frac{\mathbf{j}}{\epsilon_0} \tag{3.40}$$

where $\epsilon_0$ is the dielectric constant of free space. This system of equations imposes a numerical constraint that electron plasma oscillations due to the electric and magnetic fields are resolved in time. The details of physics on this timescale is unimportant for our simulation so it is advantageous to implicitly integrate over this time scale. This is the most fundamental and important result of our generalized Ohm's law formulation. We have limited the previously unbounded phase velocity of the whistler wave for large wave number $k$ by introducing a stiff timescales that are independent of $k$ and dependent of the number density and magnetic field magnitude. However, the physics of these stiff sources are of no physical interest to our system. The reduced phase velocity of the whistler can then be resolved explicitly over the implicit integration time required for the electron cyclotron and electron plasma frequencies. Whereas if we solved a system without the stiff source terms, we would need to implicitly treat the spatially coupled induction equation Hall term whose frequency goes like $k^2$.

## 3.4 Semi-Implicit Advance for Stiff Source Terms

We now address the issue of time integration for the generalized Ohm's law Maxwell system and in particular focus on the numerical time integration of the stiff source terms in our conservation system. The semi-discrete nature of the relaxation system used along with the TVD-MUSCL algorithm lends itself to a method of lines treatment. The method of lines [51] is a numerical technique where we discretize all but one dimension, in this case time. We then time ad-

vance our partial differential equations as a set of coupled ordinary differential equations. In particular higher order time integration through predictor corrector methods provides a reasonable stability domain and storage overhead if the system is to be extended to massively parallel three dimensional problems via simple domain decomposition on a uniform grid. Implicit-Explicit (IMEX) Runge-Kutta methods have been applied to the relaxation scheme [52] to integrate over the stiff source terms of the auxiliary vector when the relaxed limit is not used. We apply this technique to the stiff physical source terms which, as discussed in the previous section would require that our explicit time-steps be limited by the plasma frequency. The spatial order of the TVD-MUSCL system is 2nd order due to the linear reconstruction, and we now derive a second order in time IMEX Runge-Kutta scheme for the generalized Ohm's law Maxwell system.

The model Equations 3.39 - 3.40 demonstrate that the numerically stiff plasma frequency terms occur from the relationship of the electric field and current density in Ohm's law and Ampere's law. Our goal is to implicitly advance all of the timescales in the system that form linear operators which implies implicitly advancing the electric field and current density. In the generalized Ohm's law system this will mean that we are implicitly integrating over the plasma frequency timescales and the magnetic diffusion timescales. For the IMEX Runga-Kutta method under the second order implicit-explicit midpoint scheme [53] the explicit stage tableau given in Butcher notation which for the

coefficient table

$$\begin{array}{c|cccc} c_1 & a_{11} & a_{12} & \dots & a_{1s} \\ c_2 & a_{21} & a_{22} & \dots & a_{2s} \\ c_s & a_{s1} & a_{s2} & \dots & a_{ss} \\ \hline & b_1 & b_2 & \dots & b_s \end{array} \tag{3.41}$$

defines the stages of the Runge-Kutta update

$$U^{n+1} = U^n + h \sum_{i=1}^{s} b_i k_i \tag{3.42}$$

$$k_i = f\left( t_n + c_i h, U^n + h \sum_{j=1}^{s} a_{ij} k_j \right) \tag{3.43}$$

under these definitions the explicit tableau for the two stage system is given by

$$\begin{array}{c|cc} 0 & 0 & 0 \\ \frac{1}{2} & \frac{1}{2} & 0 \\ \hline & 0 & 1 \end{array} \tag{3.44}$$

and the implicit stage tableau is

$$\begin{array}{c|cc} 0 & 0 & 0 \\ \frac{1}{2} & 0 & \frac{1}{2} \\ \hline & 0 & 1 \end{array} \tag{3.45}$$

with the semi-implicit discretization at time level $n$ for generalized Ohm's law is given by

$$\frac{j_x^{n+1} - j_x^n}{\Delta t} + \nabla \cdot \mathbf{f}_{jx}^{n*} = \left( \frac{L_0}{\lambda_e^{n*}} \right)^2 \left[ E_x^{n+1} + (\mathbf{u} \times \mathbf{B})^{n*} \cdot \hat{x} - \eta j_x^{n+1} - \frac{\lambda_{i0}}{L_0} \left( j_y^{n+1} B_z^{n*} - j_z^{n+1} B_y^{n*} \right) \right] \tag{3.46}$$

$$\frac{j_y^{n+1} - j_y^n}{\Delta t} + \nabla \cdot \mathbf{f}_{jy}^{n*} = \left( \frac{L_0}{\lambda_e^{n*}} \right)^2 \left[ E_y^{n+1} + (\mathbf{u} \times \mathbf{B})^{n*} \cdot \hat{y} - \eta j_y^{n+1} - \frac{\lambda_{i0}}{L_0} \left( j_z^{n+1} B_x^{n*} - j_x^{n+1} B_z^{n*} \right) \right] \tag{3.47}$$

$$\frac{j_z^{n+1}-j_z^n}{\Delta t}+\nabla\cdot\mathbf{f}_{jz}^{n*}=\left(\frac{L_0}{\lambda_e^{n*}}\right)^2\left[E_z^{n+1}+(\mathbf{u}\times\mathbf{B})^{n*}\cdot\hat{z}-\eta j_z^{n+1}-\frac{\lambda_{i0}^n}{L_0}\left(j_x^{n+1}B_y^{n*}-j_y^{n+1}B_x^{n*}\right)\right] \tag{3.48}$$

where the hyperbolic flux terms for the electron stress tensor are represented by $F_j(U)$ and * denotes that the time level is estimated at n+1 from the split explicit terms. The discretized Ampere's equation with the electric field flux $F_E(U)$ is

$$\frac{E_x^{n+1}-E_x^n}{\Delta t}=\left(\frac{c}{V_{a0}}\right)^2\left(\nabla\cdot\mathbf{f}_{Ex}^{n*}-j_x^{n+1}\right) \tag{3.49}$$

$$\frac{E_y^{n+1}-E_y^n}{\Delta t}=\left(\frac{c}{V_{a0}}\right)^2\left(\nabla\cdot\mathbf{f}_{Ey}^{n*}-j_y^{n+1}\right) \tag{3.50}$$

$$\frac{E_z^{n+1}-E_z^n}{\Delta t}=\left(\frac{c}{V_{a0}}\right)^2\left(\nabla\cdot\mathbf{f}_{Ez}^{n*}-j_z^{n+1}\right) \tag{3.51}$$

and we can exploit the form of coupling between GOL and Ampere's equation given by

$$\begin{bmatrix} X & X & X & X & 0 & 0 \\ X & X & X & 0 & X & 0 \\ X & X & X & 0 & 0 & X \\ X & 0 & 0 & X & 0 & 0 \\ 0 & X & 0 & 0 & X & 0 \\ 0 & 0 & X & 0 & 0 & X \end{bmatrix}\begin{bmatrix} j_x^{n+1} \\ j_y^{n+1} \\ j_z^{n+1} \\ E_x^{n+1} \\ E_y^{n+1} \\ E_z^{n+1} \end{bmatrix}=\begin{bmatrix} rhs_{j_x} \\ rhs_{j_y} \\ rhs_{j_z} \\ rhs_{E_x} \\ rhs_{E_y} \\ rhs_{E_z} \end{bmatrix} \tag{3.52}$$

to simplify the linear system resultant from the IMEX-Runge Kutta update for the electric and magnetic fields. The electric field in Ampere's law is solved for

in terms of the current densities then substituted into the generalized Ohm's law. This reduces the implicit update to a three by three algebraic system for each cell with no spatial coupling. The 3x3 system must be solved twice when advancing to the next time level, once for the predictor and once for the corrector. For this semi-implicit system, the new explicit CFL will be determined from the Hall term through the whistler wave with its bounded propagation.

## 3.5 Initial Conditions and Boundary Conditions

In order that our numerical description of the time evolution of an ablating wire array be well posed, we require the proper initial conditions and boundary conditions that describe the physical phenomena. The generalized Ohm's law Maxwell system is a set of four vector fields $\mathbf{U} = [\mathbf{E}, \mathbf{B}, \mathbf{j}, \rho\mathbf{u}]$ and two scalar fields $(\rho, \epsilon)$. Since the model is limited to describing the fluid regime of the plasma, we require initial conditions for these fields that are later than the initial time of the experiment. That is, in the real experiment the solid wires experience a resistive heating phase that results in a coronal plasma column surrounding a core of higher density material. The details of the evolution to the plasma state require a kinetic description and complex equation of state which can take in to account phase transitions. Modeling of this phase is beyond the scope of the thesis, so our initial condition will be that of cold plasma columns. Since the physical wires have diameters on the order of tens of microns and the system size is in the tens of millimeters it is computational expensive to have a uniform grid that is of order the core diameter. The plasma core is instead represented by a single

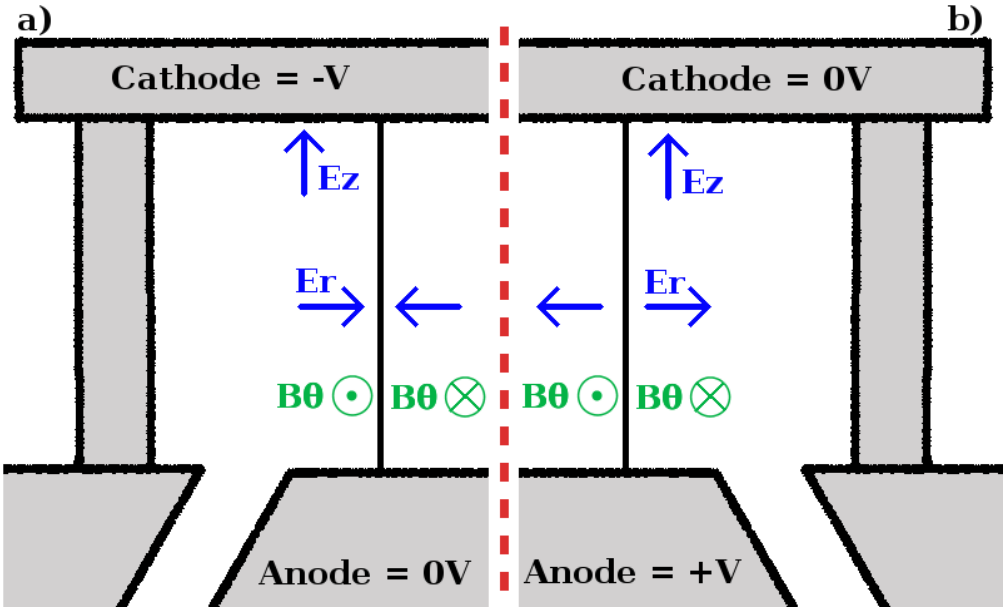


Figure 3.1: Anode-cathode geometry for wire array Z-pinch in a) negative polarity and b) positive polarity

.

cell in the simulation domain whose line density $\rho_l$ is given by

$$\rho_l = \frac{\rho_{wire}\Delta x \Delta y}{\pi r_{wire}^2} \tag{3.53}$$

where $\rho_{wire}$ is the density at standard temperature and pressure for the wire material, $(\Delta x, \Delta y)$ represents the x and y grid spacing, and $r_{wire}$ is radius of the wire to be represented by the grid. The temperature is uniform across the domain and is set close to zero eV. Additionally, the electric field, magnetic field, current density, and momentum are all set to zero. This initial condition does not correspond exactly to the experiment initial conditions since it neglects the details of phase transitions. Due to this approximation, it is not reasonable to expect that the simulation will include the breakdown time of the wire which usually occurs 15 ns into the experiment.

Open boundary conditions are applied to the system except for the magnetic

field which we will now give the details of. Figure 3.1 shows a cartoon cross section of the load region of a pulsed power machine. The magnetic field boundary condition drives the current in the system given an ideal current source. The current source approximates the pulsed power driver as $I(t) = I_0 \sin(t\pi/2t_r)^2$ where $t_r$ is the current rise time usually set to 100 ns and $I_0$ is the peak current of 1 MA. The tangential component of the magnetic field on the boundary is then determined from the far field approximation that the wire array is a line source of current. The well known formula for the magnetic field of an infinitely long wire and our drive input $I(t)$ is given by $B_{theta}(t) = \mu_0 I(t)/2\pi r$ where r is the distance from the center of the simulation domain to that of the boundary. The normal component, $B_n$, is determined from the constraint that the magnetic field is divergence free.

CHAPTER 4

# CODE TESTS

If we are to gain physical insight from the numerical model discussed in the previous chapter, we must first verify and validate the code. Verification of software is a broad term, but for this thesis we consider it to be the task of proving that the implementation of the algorithm is consistent with the derived numerical algorithms. We consider three tests for our algorithm. The first looks at the phase velocity of linear waves propagating in the system versus the mode number for a static grid. The second test involves mapping out the dispersion relation for the whistler wave and its resonances, while making sure that each mode is resolved by varying the grid size. The final test considers the shock capturing nature of the code and recovery of the MHD limit. We now present these verification tests. The validation of the code, along with the appropriateness of the GOL approximation, will be considered through comparison to experimental wire array results in the next chapter.

## 4.1 Whistler Wave Phase Velocity Convergence

We now approach the problem of verification of the numerical approximation to a system of nonlinear partial differential equations. Since the general solution to the system of nonlinear differential equations is not known, we are limited to comparing code results to the known solutions from small linear perturbations of the system. The two-fluid plasma system has a multitude of waves, so we select the waves which will play the largest role in the evolution of the system. The fast branch contains the whistler wave, which corresponds to propagation

parallel to the magnetic field, and the lower hybrid wave, which corresponds to propagation perpendicular to the magnetic field. The whistler will typically be the fastest propagating wave in the simulation and will determine the time step. The whistler dispersion relation is found from the parallel propagation roots 3.37 of the Stringer system, and for this test we use a simplified form of its phase velocity

$$\frac{\omega}{k} = \frac{V_a}{\sqrt{1 + k^2 \lambda_e^2}} \tag{4.1}$$

If the electron inertial length $\lambda_e$ asymptotically approaches zero, then the phase velocity increases without bound as the wave vector increases. This dispersive behavior will cause numerical instability in simulations that include the whistler wave because the shortest wavelength waves will also have the largest phase velocity. The $\lambda_e = 0$ limit is the Hall MHD model in which the behavior of the whistler mode has been studied [54]. As a test of the code we consider the linear propagation of a whistler wave with finite $\lambda_e$, which will limit the phase velocity to the electron cyclotron frequency as the wave number increases. In a similar manner to [54], we initiate a whistler wave propagating parallel to an ambient magnetic field $B_x$ with a strength of 0.1 T. For a low beta plasma the background number density is set to a background level of $10^{12}\,\mathrm{cm}^{-3}$ and the system length is 0.2 m. The ion inertial length is 1.16 m, the electron inertial length is 0.0271 m, and the simulation domain consists of 128 points in the x dimension. In this regime the whistler phase velocity will be limited by electron inertia for most modes. The goal of this test is to understand how many grid points are required to resolve the whistler wave. The simulation results of frequency versus mode number for the GOL-Maxwell system are plotted in Figure

4.1 using plus marks. As the wavelength of the wave decreases, the dispersion characteristics match those of the combined Hall and electron inertia analytic model represented by the solid line. This is presented in comparison to the Hall MHD dispersion relation whose analytic value is given by the dashed line. As the wavelength tends toward the grid scale, the phase velocity errors increase in a similar manner to [54]. From Figure 4.1 we conclude that when explicitly resolved, the numerical algorithm of the previous chapter reasonably captures the linear propagation of whistler waves for modes resolved by ten or more grid points. This test only offers a small sample of the possible wave numbers typically found in pulsed power experiments, so we now apply the linear test to the asymptotic electron cyclotron limit.

In addition to testing the propagation in the vacuum region for constant grid size, we explore the propagation of plane waves while keeping each mode resolved by the same number of grid points. We perform this test for coronal plasma with a number density of $10^{17}\,\mathrm{cm}^{-3}$. Since we wish to only evolve the linear modes associated with the whistler wave, we require a more exact dispersion relation that takes into account the role of displacement current in addition to the Hall and electron inertia terms. Also, we want to avoid exciting hydrodynamic modes since the linear regime for the coronal plasma exists only for extremely small amplitudes. We can remove the possibility of exciting hydrodynamic modes by freezing the flow in the ion frame and evolving only the electric field, magnetic field, and current density. The ions will then provide a static background for the dynamics of the electrons, evolving the code under the electron MHD (EMHD) model. The reduced set of equations under this constraint is given by

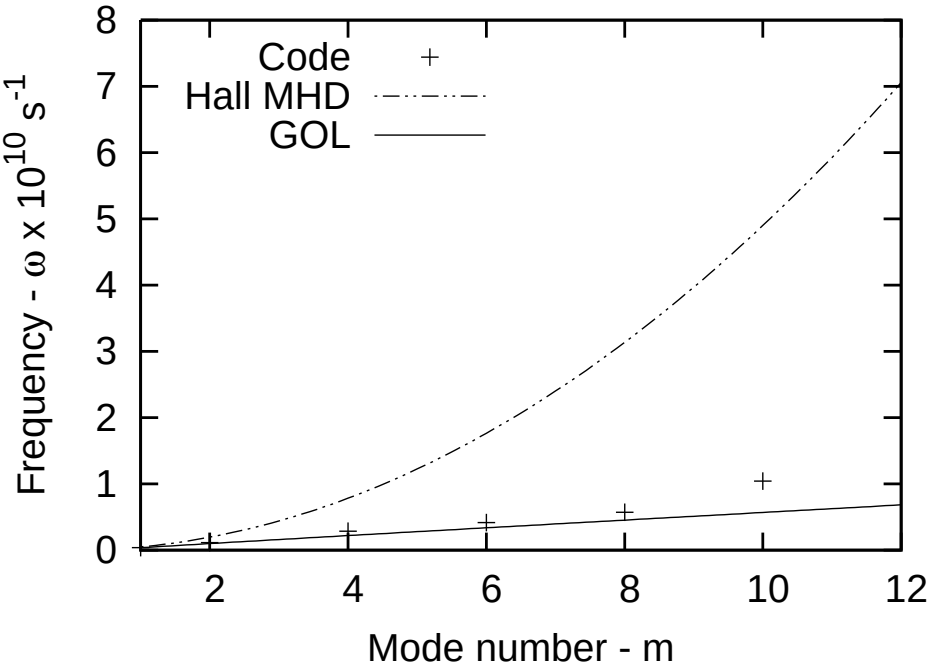


Figure 4.1: Frequency versus mode for a whistler wave propagating parallel to $B_x$. The analytic dispersion relation for Hall MHD is given by the dashed line, the analytic dispersion relation for full generalized Ohm's law is given by the solid black line, and the calculated frequencies are represented by the plus marks.

$$\frac{\partial \mathbf{j}}{\partial t} = \frac{L_0^2}{\lambda_{e0}^2} n_e \left[ \mathbf{E} - \frac{\lambda_{i0}}{L_0 n_e} \mathbf{j} \times \mathbf{B} \right] \tag{4.2}$$

$$\frac{\partial \mathbf{E}}{\partial t} = \frac{c^2}{V_{a0}^2} \left[ \nabla \times \mathbf{B} - \mathbf{j} \right] \tag{4.3}$$

$$\frac{\partial \mathbf{B}}{\partial t} = -\nabla \times \mathbf{E} \tag{4.4}$$

where variables with '0' denote the dimensional terms whose ratios define the dimensionless parameterization of our system of equations.

The EMHD equations are then linearized for wave modes propagating parallel to $\mathbf{B} = B_0 \hat{x}$ which results in a set of six equations evolving the variables $B_y, B_z, E_y, E_z, j_y, j_z$. This provides us with the initial amplitudes and dispersion

relation for the linear perturbation, which are found by solving the linear system for the following equations in which we have set the system length relative to $2\pi$

$$-i\omega j_y = \frac{L_0^2}{\lambda_{e0}^2} n_e E_y - \Omega_{e0} t_0 j_z \tag{4.5}$$

$$-i\omega j_z = \frac{L_0^2}{\lambda_{e0}^2} n_e E_z - \Omega_{e0} t_0 j_y \tag{4.6}$$

$$-i\omega E_y = \frac{c^2}{V_{a0}^2}\left[-ik_x B_z - j_y\right] \tag{4.7}$$

$$-i\omega E_z = \frac{c^2}{V_{a0}^2}\left[ik_x B_y - j_z\right] \tag{4.8}$$

$$-i\omega B_y = ikE_z \tag{4.9}$$

$$-i\omega B_z = -ikE_y \tag{4.10}$$

The dispersion relation found from the determinant of the linearized model is given in dimensionless form by

$$\omega^2\left[1 + \frac{\omega_{pe0}^2 t_0^2 \omega_{pe}^2}{k^2 \frac{c^2}{V_{a0}^2} - \omega^2}\right]^2 = \Omega_{e0}^2 t_0^2 \Omega_e^2 \tag{4.11}$$

There are six roots of $\omega$, four of which correspond to left and right traveling light waves, and two that correspond to the left and right traveling whistler wave. The whistler wave in this formulation has a resonance at the electron cyclotron frequency due to the inclusion of electron inertia. We now test the code in this regime by initializing the electromagnetic field along with the current density with small amplitude perturbations determined from solving Equations 4.5 - 4.10.

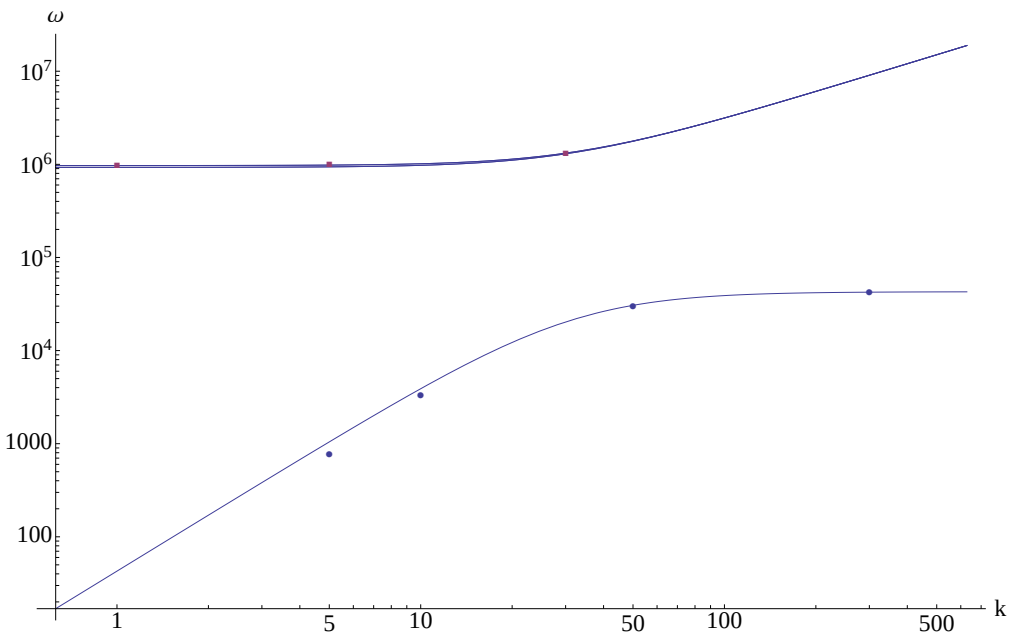


Figure 4.2: Frequency versus mode for a whistler wave propagating parallel to $B_x$, where each wave number is resolved by the same number of grid points. The red squares represent the numerical results for the light wave branches and the blue dots represent the numerical results for the Whistler branch. Both are performed for explicit time steps.

The results of the numerical test with explicit time stepping are shown in Figure 4.2. For this regime, both branches of light waves nearly overlap, and we test the fastest light wave branch. The results of the test for light waves are given by the red squares. The blue dots show the wave frequency calculated by the code for the whistler branch. Since the same number of grid points were used to resolve each mode, the error is larger for smaller wave number. This is caused, in part, by the increase in the separation of time scales between the light and the whistler waves as seen in Figure 4.2. The result of this test is that the code recovers the correct phase velocities for the regions numerically tested. Also, the electron cyclotron cutoff to the whistler propagation mode is present. This greatly decreases the required time step as compared to the Hall MHD model.

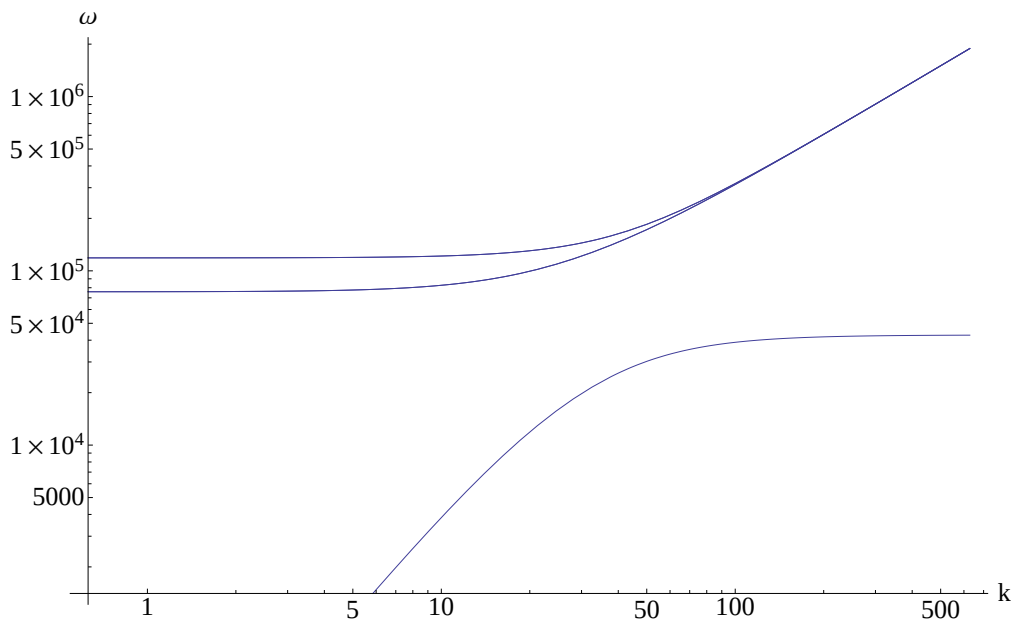


Figure 4.3: Frequency versus mode for a whistler wave propagating parallel to $B_x$ where the speed of light has been reduced by a factor of ten.

The previous tests were performed with the speed of light set to its physical value. As mentioned in Subsection 3.1.2, it is advantageous to decrease the speed of light to a few times the timescales of interest. The dispersion curve that results from decreasing the speed of light by a factor of ten is shown in Figure 4.3.

As the speed of light is decreased even further, the dispersion curves for light waves and the whistler wave merge. Figure 4.4 shows the dispersion curve for the speed of light reduced by a factor of one hundred. In this case, the speed of light is approximately 3000 km $s^{-1}$, or about ten times the fastest MHD velocity of interest for a wire array on COBRA.

The primary effect of decreasing the speed of light is the merger of the light wave and whistler wave branches at large wave numbers. Because these

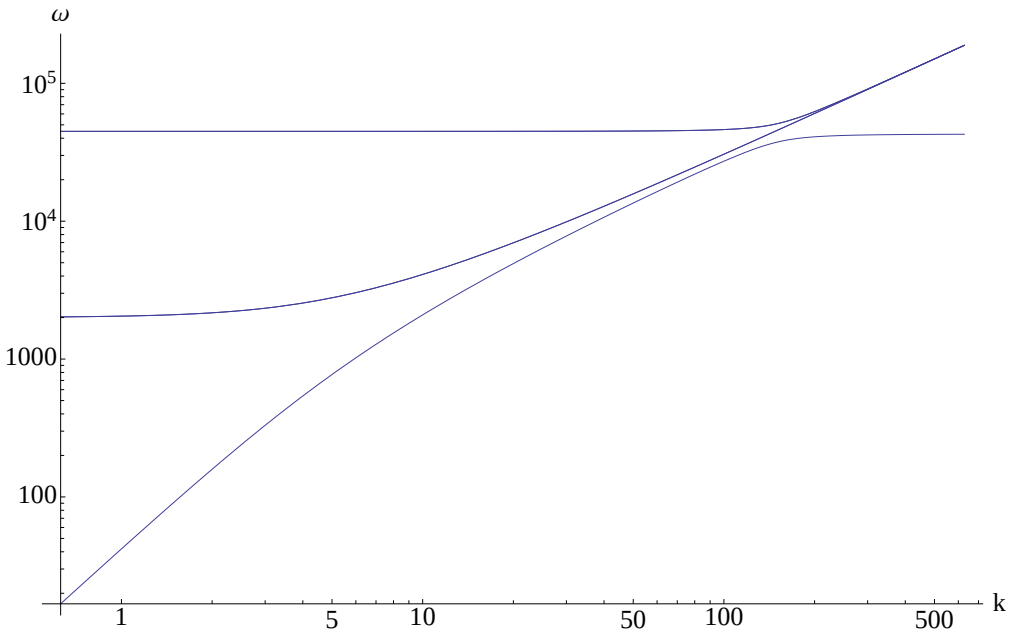


Figure 4.4: Frequency versus mode for a whistler wave propagating parallel to $B_x$ where the speed of light has been reduced by a factor of one hundred.

branches merge as we increase the dielectric constant for the system, testing the phase velocities for these branches in the linear regime becomes increasingly difficult. The main result of the linear wave tests is that for explicit time stepping the code properly represents the whistler wave propagation in the presence of electron inertia and displacement current.

## 4.2 Collisionless Plasma Shock Tube Test

Many of the systems we desire to model will contain both regions where the ideal plasma description is suitable and regions where two species effects are important. It is important that the code can describe the transition between these asymptotic states. We now consider the verification of the two-fluid algo-

rithm for both limits. The first case we consider is when the ion and electron inertial lengths are much smaller than any region of interest. For practical computation of wire array problems the electron inertial length will be hundreds, or even thousands, of times smaller than the shortest wavelength resolved by the numerical grid, and in this limit ideal MHD must be recovered. This situation is tested using the Brio-Wu shock tube problem [55]. The Brio-Wu shock tube gives initial conditions for a discontinuity between two plasma states separated by a membrane which is removed at the start of the simulation. The system evolves in a manner closely connected to the eigenstructure of the hyperbolic equations describing the motion of the plasma. This allows us to test the convergence of the generalized Ohm's law system to that of the MHD Riemann problem. This test is important since the system of equations we are integrating lies in between the two-fluid and ideal MHD models. For the full two-fluid equations, as in [28], a discontinuity is posed in terms of a jump in the separate ion and electron species. The eigenstructure of the Euler equation for each species gives right and left traveling waves that propagate at their thermal velocities in the species fluid frames. The Riemann problem for this model is determined in a similar manner by the structure of the eigenvalues and eigenvectors of the flux Jacobian, and the electric and magnetic fields are determined from the separate set of Maxwell's equations. Starting with the two-fluid model and taking the electron and ion inertial lengths to zero does not directly result in the MHD system. Under the MHD approximation, the hyperbolic system describes the evolution of the plasma in a different set of variables posed in the center-of-mass frame and under the quasi-neutral assumption. Additionally, the induction equation determines the evolution of the magnetic field, and a discontinuity in the magnetic field is coupled with the momentum and energy

equations. The generalized Ohm's law model lies in between these two systems but has an eigenstructure more closely related to the two-fluid model. It is described in the center-of-mass formulation but the neglect of electron pressure and advection terms reduces the unique set of eigenvalues to the center-of-mass fluid velocity and sound speed. Due to these simplifications of the physics, it is not clear if the MHD limit for a discontinuity can be exactly recovered or approximated, so we now numerically test this approximate system.

The initial conditions correspond to a plasma with two species in the center-of-mass frame whose non-zero values for the left state are

$$\begin{bmatrix} \rho \\ P \\ B_x \\ B_y \end{bmatrix} = \begin{bmatrix} 1 \\ 1 \\ 0.75 \\ 1.0 \end{bmatrix} \tag{4.12}$$

and non-zero values for the right state are

$$\begin{bmatrix} \rho \\ P \\ B_x \\ B_y \end{bmatrix} = \begin{bmatrix} 0.125 \\ .1 \\ 0.75 \\ -1.0 \end{bmatrix} \tag{4.13}$$

The dimensionless system has length 1.0 and the ratio of the cell size to the electron inertial length is varied from $\Delta x \approx 30\lambda_e$ to $\Delta x \approx 500\lambda_e$. Thus, for both cases the inertial length is unresolved, which will be the case when high density plasma is present in the simulation. The system is then evolved to a dimensionless time of 0.1. In these tests, the under-resolved inertial length is compared to

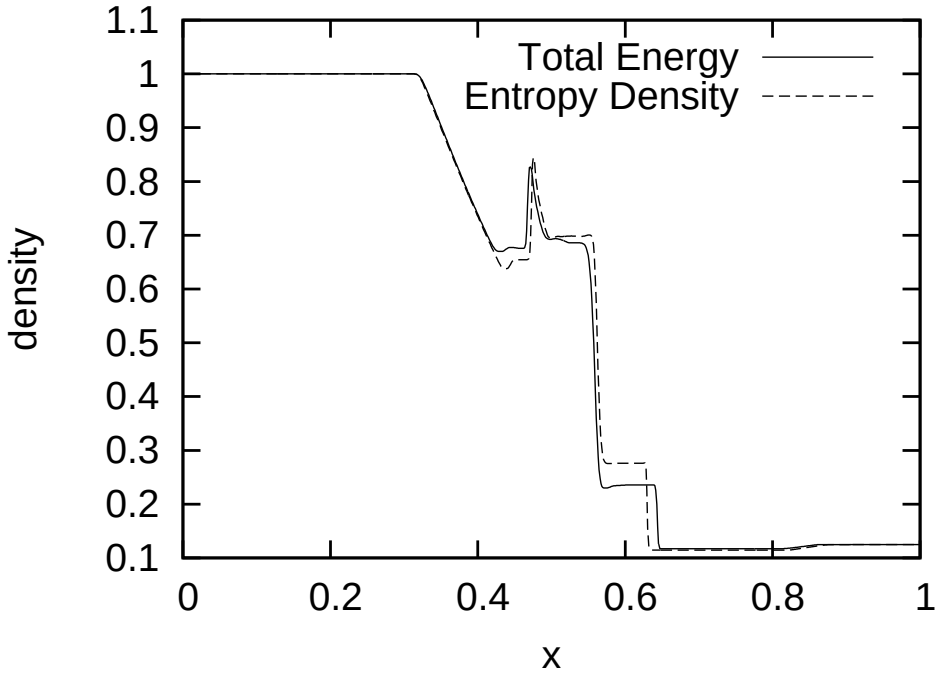


Figure 4.5: Number density at time t=0.1 from simulation of the Brio-Wu shock tube problem. The solid line represents MHD limit under the total energy density formulation, while the dashed line shows the approximate entropy density solution.

a reference solution calculated using the ideal MHD model. For both the ideal MHD and generalized Ohm's law systems, the previously discussed entropy density approximation is used. The entropy density approximation can be compared to the ideal MHD solution where the total energy is evolved. Figure 4.5 details the differences between the shock tube problem for each formulation.

In Figure 4.6 the shock tube results for the y component of the magnetic field are presented. The resultant magnetic field from the solution of Maxwell's equations along with generalized Ohm's law recovers the ideal MHD limit when the grid spacing is thirty times the electron inertial length. For much larger grid spacing, the error is large and diffusive. This result makes sense in terms of the

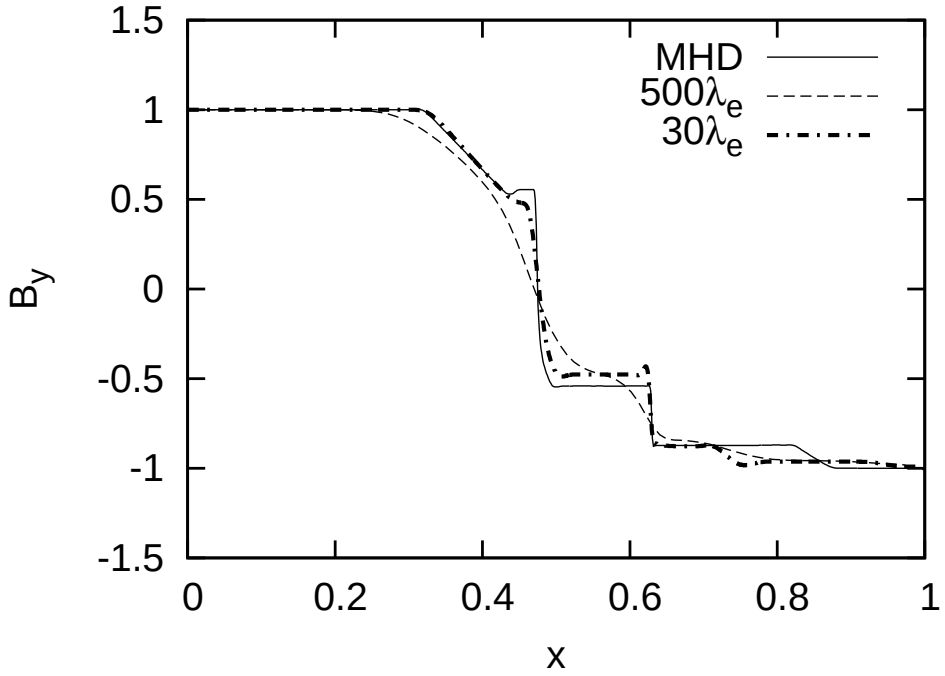


Figure 4.6: Magnetic field ($B_y$) result from simulation of Brio-Wu shock tube problem using the generalized Ohm's law model at dimensionless time t=0.1 in the limit that the electron inertial length $\lambda_e$ is under-resolved for grid spacings of 500 and 30 inertial lengths. Solid line represents MHD limit under the entropy density approximation.

implicit advance of the electric field and current density. Figure 4.7 shows the number density at time t=0.1 for the shock tube problem. For a greatly under-resolved grid, the resultant time step for a reduced speed of light will greatly exceed the inverse of the plasma frequency. Still, many of the structures are recovered, such as, from left to right: the fast rarefaction wave, the contact discontinuity, the slow compound wave, the slow shock, and the fast rarefaction. The largest error from the approximate system is in the fast rarefaction wave. The recovery of these structures shows that implicit integration over the plasma frequency in the generalized Ohm's law formulation can approximate the ideal MHD limit. This is a remarkable result, in that it shows that we do not need to

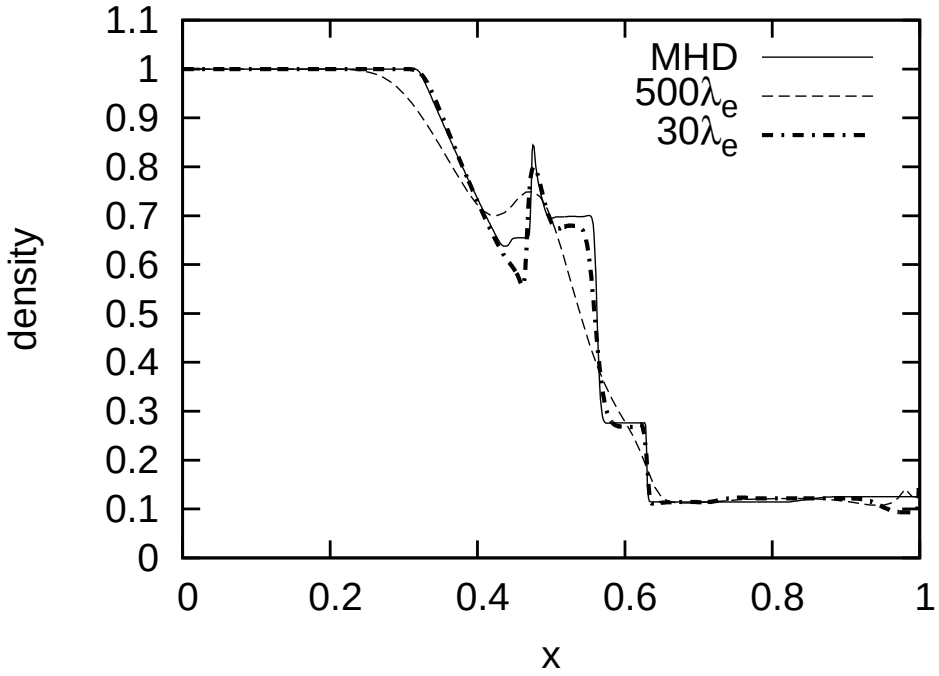


Figure 4.7: Number density ($\rho$) result from simulation of Brio-Wu shock tube problem using the generalized Ohm's law model at dimensionless time t=0.1 in the limit that the electron inertial length $\lambda_e$ is under-resolved for grid spacings of 500 and 30 inertial lengths. Solid line represents MHD limit under the entropy density approximation.

resolve the electron inertial length with our grid spacing to correctly simulate the MHD flows. While taking MHD scale time steps, the code will naturally recover the MHD limit in regions where two-fluid effects are negligible. As the density decreases as we move into the coronal regions, the grid will resolve the ion and electron inertial lengths and in these regions two-fluid waves will propagate. This is a unique way of handling the multi-scale physics inherent in plasma flows into a vacuum.

Next we test the regime where electron inertia limits current flow in the system. The inertial length is set to 100 times the system size with the same initial

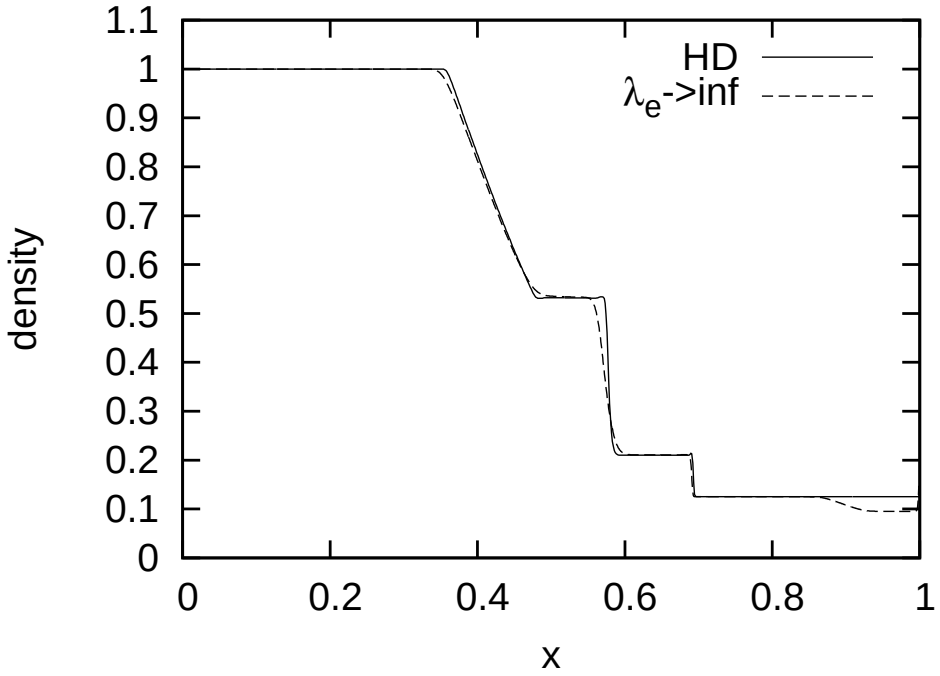


Figure 4.8: Number density ($\rho$) result from simulation of Brio-Wu shock tube problem using the generalized Ohm's law model at dimensionless time t=0.1 in the limit that the electron inertial length goes to infinity. The solid line represents the hydrodynamic solution to the Brio-Wu shock tube problem with initial left and right magnetic field set equal to zero. Dashed line is the generalized Ohm's law solution with magnetic field included in left and right states with the inertial length set larger than the system size.

conditions as before. At time t=0.1 the large inertial length solution is compared to the solution of the shock tube problem where only the gas dynamics are evolved. This uses the previously shown left and right states, except the magnetic field is set to zero. Since the electrons are decoupled from the flow, the system shows only hydrodynamic evolution and recovers the gas dynamic solution.

If we pose these results in terms of the wire array problem relative to the in-

ertial lengths applied, the system would be analogous to a region of aluminum plasma at solid density. This is then an extreme example, and we can expect to integrate a wire array system where most of the streaming ablation dynamics occur at lower density and longer inertial lengths. The overall results of both the implicit shock tube tests is that for our implicit formulation we can recover the ideal MHD limit up to some certain limitations. These limitations are mostly due to the discrepancy between the fast rarefaction velocities and numerical overshoot in the shock profile. Further exploration is required to understand the impact of these differences. Now that we have a self-consistent theoretical and numerical basis for exploring the physics of pulsed power loads, we can increase our physical understanding of these systems. In the next chapter we begin our exploration of the physics of wire arrays by first considering how the resistive MHD model represents streaming ablation.

CHAPTER 5

# RESISTIVE MHD STUDY OF ABLATION ACCELERATION REGION IN CYLINDRICAL WIRE ARRAYS

In the following chapters, we will use the previously introduced numerical and theoretical models to address issues specific to pulsed power loads commonly fielded on COBRA. We begin our exploration of the physics of pulsed power loads by first considering the Resistive MHD description of ablative flows in the wire array Z-pinch configuration. This will serve as a reference to the two-fluid results so that we may compare and contrast the differences and gain a greater understanding to the physical origin of the dynamical evolution of these plasmas. In dense Z-pinch experiments such as those on the pulsed power COBRA accelerator [56], a cylindrical array of wires is driven with 1 MA peak current over a 100 ns rise-time. The individual wires initially experience resistive heating, voltage collapse, corona formation, ablation on to the geometric axis, implosion, and finally stagnation when the majority of x-ray emission occurs [57]. Each individual step in the process leading to a dense Z-pinch has its own modeling challenges. In this chapter we concentrate on the region of time after voltage collapse and before the implosion of the array, focusing on the transition from discrete plasma columns to ablating wires. Several analytic and numerical models [58, 59, 15, 60, 61, 62, 63] have been proposed to predict important aspects of the ablation phenomenon in cylindrical wire arrays and have been successfully applied in experimental settings when predicting implosion times and other useful parameters. However, the nature of the acceleration region and the means by which the system organizes into an ablation configuration when the wire's local magnetic field contribution are considered is still not clearly understood for the resistive MHD model. We consider the early time be-

havior of the dynamics for sparse wire arrays. Specifically we consider the time prior to reaching the ablative streaming regime for arrays in which the current carrying coronal plasma does not overlap with neighboring wires. During this interval the magnetic field just inside the array radius and within the corona is such that $\mathbf{J}\times\mathbf{B}$ is locally towards the wire, referred to as the closed or local magnetic field configuration. In the closed field configuration the only local force in this region that can push the plasma towards the axis is plasma pressure. When the current carried by this pressure driven plasma is sufficiently far from the wire, the magnetic field threading the core is in the global or open magnetic field configuration such that the $\mathbf{J}\times\mathbf{B}$ force can accelerate the plasma towards the array axis. The basic mechanisms that occur before steady state ablative streaming are described and the role of a wire's local or private contribution to the magnetic field compared to the global magnetic field generated from the entire array.

Previous research on ablative streaming has focused on the small inter-wire gap limit using one-dimensional models describing the steady state ablation flow profile. These models are appropriate in this case due to the weak local field contribution to ablation dynamics and the existence of an interval in which the ablation flow is approximately steady state. As the inter-wire gap of the array increases, the one-dimensional approximation is invalid due to the inherent two-dimensional nature of the magnetic field configuration. Importantly and in contrast to previous work [15, 62], we consider the time before steady state flow during which two-dimensional geometry plays a crucial role. Specifically, we address how a wire array makes a transition from one in which the magnetic field is locally closed around the wire to one in which the magnetic field globally encloses the geometric axis by means of a current sheet partially extending from

the core to the array axis. That is, we examine the physics of the transition from a "closed" magnetic configuration to one which is "open". It is the open configuration that is relevant to the steady-state ablation configuration discussed by Yu et al. and Sasorov et al. [15, 62]; and hence our results are expected to be valid for a time interval preceding the ablation phase. We also discuss the role of a time varying current drive in the competition between the expansion forces from Joule heating and the compression forces due to the magnetic field.

It has been previously found, [64] and we have confirmed, that resistive MHD simulation predicts that current will distribute itself radially inward from the wires, extending the $\mathbf{J} \times \mathbf{B}$ acceleration area well beyond the coronal radius. The process by which ablation initiates and its relation to the formation of a current sheet inside the array is still an open issue. Before moving to a full two-fluid description of wire arrays in the next chapter, we analyze these flows with the GORGON resistive MHD code [64] and use it to track the evolution of the magnetic field configuration between initiation and implosion for 8 wire, 20 mm array diameter, 12.5 micron wire diameter aluminum cylindrical arrays on COBRA and numerically investigate the transition to wire ablation. The results provide a clear explanation of the process by which the global magnetic field makes a transition from a vacuum configuration to an ablation configuration.

In Section 5.1 we discuss how the two-dimensional magnetic field undergoes a transition from a locally closed magnetic field to one with a global magnetic field resulting from a current sheet extending away from the core towards the array axis. In Section 5.2 we address how the plasma and magnetic field decouple in the low magnetic Reynolds number limit to allow pressure expansion of the plasma. In Section 5.2 we use the one-dimensional resistive MHD model to

examine the basic one-dimensional physics of plasma expansion into the vacuum. It is shown that the plasma-vacuum transition is characterized by a jump in plasma beta to approximately unity. These results are used to motivate the analysis in Section 5.3 that explicitly accounts for the two-dimensional geometry. We give scaling relations that provide the required Joule heating rate such that the current carrying plasma vacuum interface will advance far enough to switch the magnetic field to an open configuration before the 0-D implosion time. In Section 5.4 the requirement for ablative streaming is tested through numerical experiment with the GORGON code.

## 5.1 Global Field Penetration as a Requirement for High Mach Number Ablative Streaming

We initialize the resistive MHD wire array simulation using GORGON with plasma density distributed in equally spaced wires around a common geometric axis at radius $R = 10$ mm. A vacuum resistivity, an anomalous collisionality applied at the density floor, allows all of the applied field on the simulation boundary to diffuse inward and form currents in the wires corresponding to the vacuum magnetic field configuration. In the vacuum magnetic field configuration, all of the current density ($J_z$ into plane) in the system is local to the wires and distributed around the wire cores in a hot corona [65]. Field lines extending from the core-corona structure are locally closed around the wires and at the separatrix converge at a magnetic x-point on the geometric axis [Figure 5.1].

This configuration corresponds to a $\mathbf{J} \times \mathbf{B}$ force pointed toward the wire core at all points around the corona with magnitude varying azimuthally around

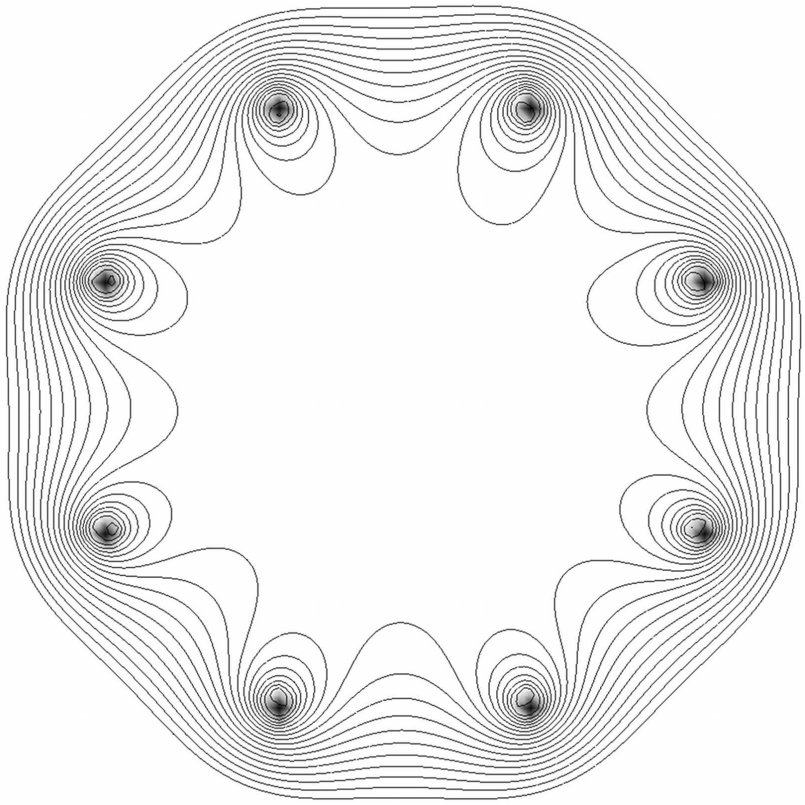

Figure 5.1: Isocontours of magnetic vector potential ($A_z$) for wire array in vacuum field configuration in x-y plane. Magnetic field lines encircle the corona of each wire such that $\mathbf{J} \times \mathbf{B}$ is directed toward the core around its entire circumference. The field configuration is locally closed.

each wire. A wire experiences Joule heating during this phase and it is thought that each wire maintains this field configuration until the thermal pressure can overcome the magnetic pressure. The magnetic pressure is weakest and the plasma expansion is greatest along the line from the core pointing to the geometric axis. This results in large radially inward flux of plasma, and since the vacuum resistivity causes the current to follow the density, a filament and subsequently a sheet are formed [Figure 5.2]. The local magnetic flux associated with the current filament that has detached from the wire is advected toward the ge-

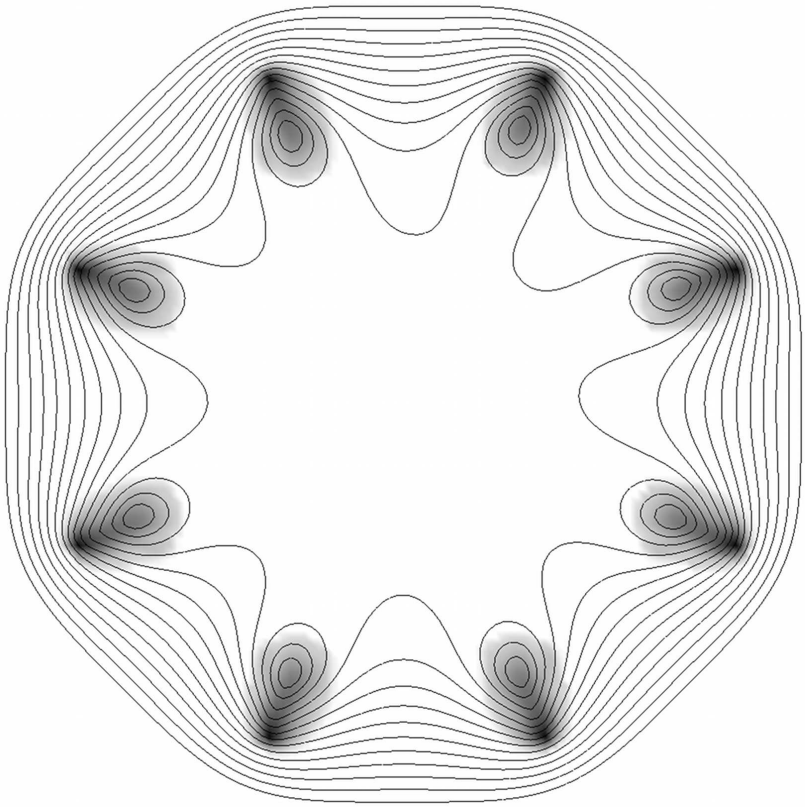

Figure 5.2: Magnetic vector potential ($A_z$) and mass density in gray-scale during the initial expulsion of plasma from the corona at 45 ns. Global field has reached the wire core and $\mathbf{J} \times \mathbf{B}$ region around the wire points toward the geometric axis. The magnetic filament still experiences a compressive $\mathbf{J} \times \mathbf{B}$ force. The field configuration now is considered to be open around the wire core in that global field threads the corona.

ometric axis and takes much of the initial current delivered to the array downstream. When the current distends into a sheet and penetrates sufficiently far towards the axis, the magnetic field near the core becomes open as it is threaded with global magnetic flux.

The current sheets merge on-axis, annihilating the local flux following the plasma-vacuum interface. The existence of null points in the magnetic field forming near the corona in an ablation configuration has been mentioned in lit-

erature [60, 66, 67]. The nature of the advection of the initial plasma is discussed in Section 3.

The global field contribution from the other wires can now diffuse through the core while the locally closed flux moves toward the geometric axis. The current filament reaches the axis and merges creating precursor plasma, at which time the overall field configuration is one of the entire magnetic field encircling the geometric axis. See Figure 5.3 for the evolution of the azimuthal magnetic field during this process. With the new field configuration, current not only surrounds the corona but is distributed in a sheet directed radially inward, along the fully-developed path of the previously expelled plasma [Figure 5.4]. In its ablation configuration, the field lines all enclose the geometric axis and the magnetic field curvature along the ablation stream bends toward the axis. The length and magnitude of the current sheet sets the amount of plasma acceleration inside the array radius.

For ablation flow to occur the current must be constrained to follow density by some means. The current follows the mass flow, creating current sheets extending along a strip from the wires to array axis. The resultant global magnetic field in the ablation configuration encircles the array axis with no reversals [Figure 5.5]. The $\mathbf{J}\times\mathbf{B}$ acceleration of the ablation flow is therefore distributed along this strip. Between the wire corona and the current filament the magnetic field lines curve in such a manner that $\mathbf{J}\times\mathbf{B}$ is directed toward the axis and focused to points on a line between the wire core and geometric axis. This change in field configuration appears to be intrinsic to cylindrical array ablation and appears over a wide range of array parameters modeled using resistive MHD. We now apply the idea of global field penetration into the array as a requirement

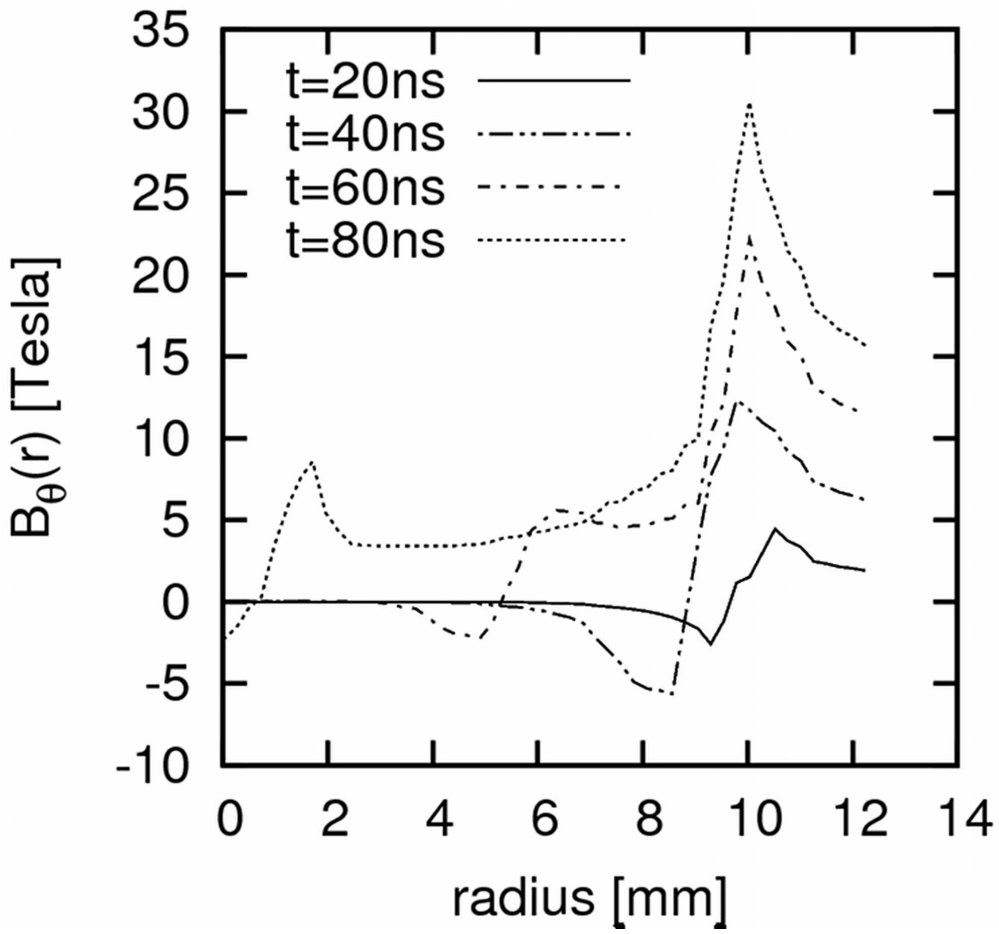


Figure 5.3: Azimuthal component of magnetic field along a chord extending from geometric axis of wire array through center of ablation stream. Global field penetrates the wire core as the local field current loop is advected toward the geometric axis.

for a transition from a pinch magnetic field configuration to an ablation magnetic field configuration, which we call the $\mathbf{J} \times \mathbf{B}$ ablation regime. This regime is described reasonably well by the models of [59, 15, 62]. We are concerned with a description of the physical processes that allow a transition into the $\mathbf{J} \times \mathbf{B}$ ablation regime.

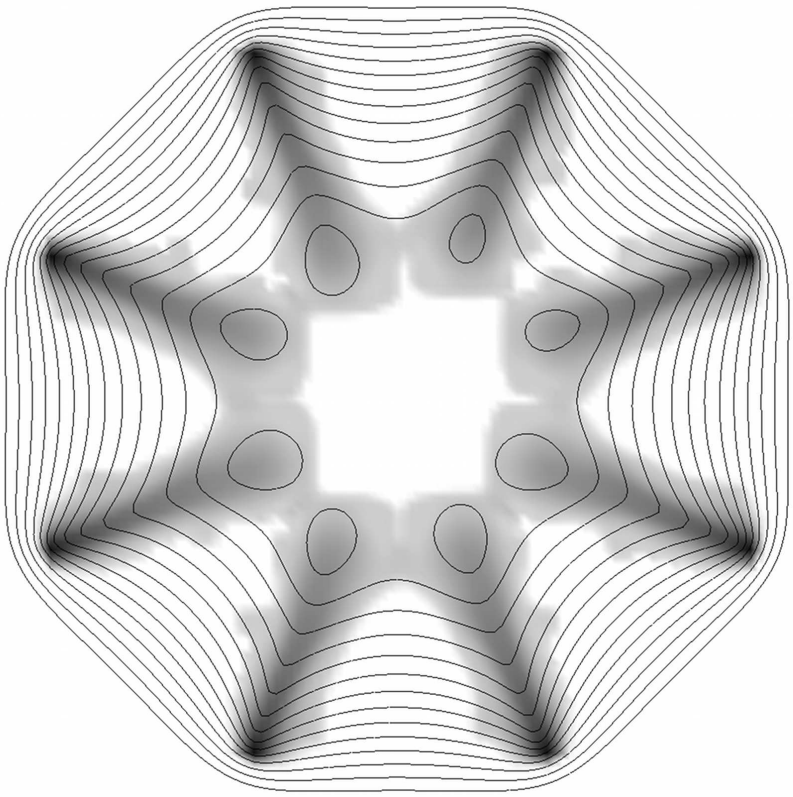

Figure 5.4: Isocontours of magnetic vector potential ($A_z$) and mass density in gray-scale at 64 ns. Magnetically confined current loops just before annihilation and overall configuration change when merging on geometric axis.

## 5.2 Early time physics

Based on the preceding GORGON two-dimensional simulations, in order that $\mathbf{J} \times \mathbf{B}$ acceleration of ablating plasma towards the axis take place, it is clear that the initial magnetic field configuration of local field enclosing the wire cores must undergo a transition to a state in which the globally linked magnetic flux threads the wire cores. Prior to this configuration change the magnetic forces are such as to pinch the coronal plasma towards a magnetic O-point. The question we now address is what process moves global field inside the array by allowing

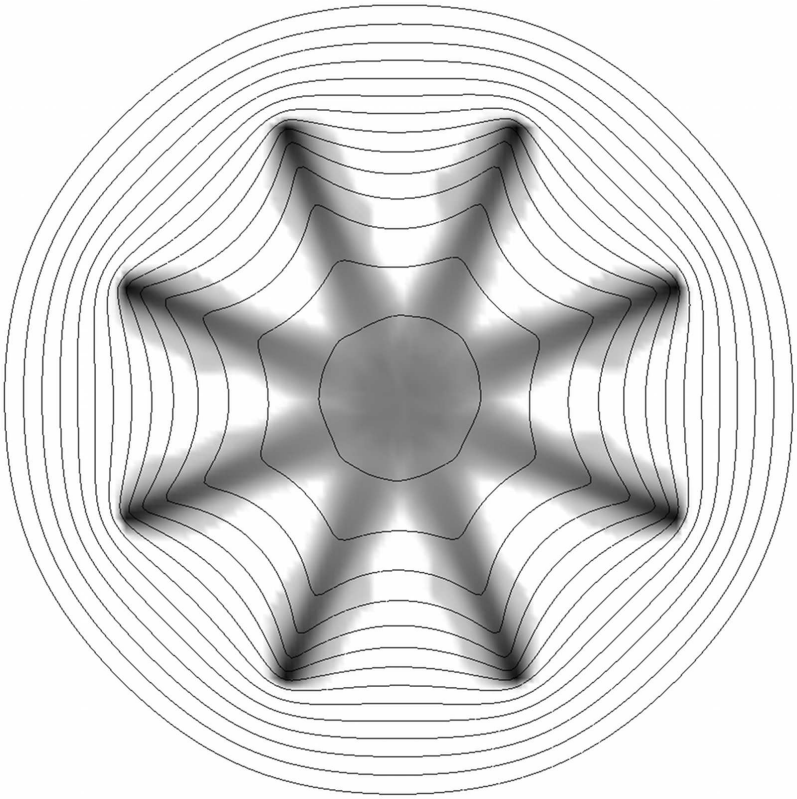

Figure 5.5: Magnetic vector potential ($A_z$) for ablation field configuration of wire array with mass density in gray-scale at 84 ns. Distributed $\mathbf{J} \times \mathbf{B}$ force is radially inward at all points along the ablation stream. Current filaments have merged into a precursor column on the geometric axis.

the corona to expand away from the core into a region of increasing magnetic field.

For magnetic Reynolds number much greater than unity, the global $\mathbf{J} \times \mathbf{B}$ contribution from the other wires will pull the expanding wire corona in a vacuum configuration towards the axis [60]. For this process to be viable for plasma streaming and precursor formation the initial coronal mass and the rate of coronal mass production $\dot{m}$ must be small enough so that the ionized plasma can be moved far enough to effect configuration change in a time sufficiently

short to agree with experiments. This mechanism can be tested using a form of the rocket model [58]. This possibility for the mechanism of the configuration change arises from a simple ideal MHD picture of the dynamics, based on flux-advection. Defining the plasma beta, $\beta$, as the ratio of the plasma pressure to the magnetic pressure, the coronal plasma confined in the closed flux very quickly develops $\beta > 1$, and expands against the closed magnetic field. At the same time, the radially-inward magnetic force due to the large global field at the outer boundary of the corona accelerates the entire coronal mass inward. The time at which the field opens at the core location then depends just on the rate of acceleration and displacement of the closed flux inward, as determined by the coronal mass and the driving force. So, in the simplest model one can consider the corona to be an object with total mass per unit length $m_c(t)$, an increasing function of time as mass is continuously ablated from the core into the corona. The driving force is the global field pressure based on the field at the array radius, $R$, due to the total current $I$. Taking the coronal mass to be axisymmetrically distributed, the velocity $v$ of the corona is then determined from

$$m_c \dot{v} = \frac{\mu_0 I^2}{4\pi R} \tag{5.1}$$

Numerically solving with this equation with the actual coronal mass as a function of time generated by two-dimensional resistive MHD simulation shows that the distance to which the coronal plasma is moved by the global force is too short to account for the coronal motion and field penetration that occur in the simulations analyzed. Therefore the magnetically-driven sweeping of the coronal mass inward is not the mechanism of opening the field and establishing ablation in these simulations given the observed mass ablation rate. The

mass ablation rate is simply the rate at which the dense, cold core of the wire loses mass over time. Hence, global magnetic forces gives an acceleration that is too slow, and field opening times that are too long, to account for the coronal motion at early times.

We put forth another hypothesis that we subsequently test by means of one-dimensional MHD simulations and simple scaling analysis. We hypothesize that Ohmic heating of the coronal plasma increases the local plasma pressure to initiate an acoustic wave that propagates towards the axis carrying density and hence current. After the current penetrates a critical distance, the global field is embedded in the wire core and corona without any local field component and streaming ablation can proceed by direct $\mathbf{J} \times \mathbf{B}$ acceleration of the coronal plasma.

This hypothesis is motivated by the expectation that in a highly resistive magnetized plasma the plasma flow and magnetic field will decouple such that the fast magnetosonic wave will degenerate into an acoustic wave. Consider the dispersion relation for perpendicular propagation in a resistive MHD plasma with sound speed $c_s$ and Alfvén velocity $v_A$.

$$\omega[\omega^2 - k^2(v_A^2 + c_s^2)] + ik^2 D(\omega^2 - k^2 c_s^2) = 0 \tag{5.2}$$

where $D = \eta/\mu_0$. This cubic can be solved exactly, but an approximate root is found to be

$$\omega = kc_s\left(1 + \frac{v_A^2}{2ikc_sD - v_A^2}\right) \tag{5.3}$$

We see that acoustic waves can propagate relatively undamped when $kc_sD \gg v_A^2$, and in this case the fast wave has disappeared. If the Ohmic heating is sufficiently rapid and the resistivity sufficiently large, a pressure pulse will launch an acoustic wave that will nonlinearly steepen into a discontinuity. The jump in density will decrease the vacuum resistivity to permit plasma current to follow the plasma-vacuum interface. For large magnetic Reynolds number, the only structure propagating out of the corona is a fast wave front with a small jump in density.

A necessary condition for ablative streaming, which we call the decoupling condition, follows from the dispersion relation Equation 5.3 and is

$$\eta \gg \frac{\mu_0 v_A^2 d}{c_s} \tag{5.4}$$

where $d$ is a scale representing the size of the propagating disturbance. For the $\beta = 1$ surface in Figure 5.6, this decoupling condition is a statement that the magnetic Reynolds number be less than unity. From these statements, we expect that the decoupling will hold over a volume moving inward from the core toward the array axis. Moving from the core outward, the decoupling condition is met until moving past the $\beta = 1$ surface into a region of strong global magnetic field. Using typical Z-pinch parameters for a scale of a few millimeters the inequality in Eq. (5.4) is well satisfied.

A one-dimensional numerical simulation of an Ohmically heated initially cold slab has been done to verify this scenario. We formulate a one-dimensional slab geometry problem in which the magnetic Reynolds number is of order unity and the expansion of the plasma is against the magnetic pressure gradient.

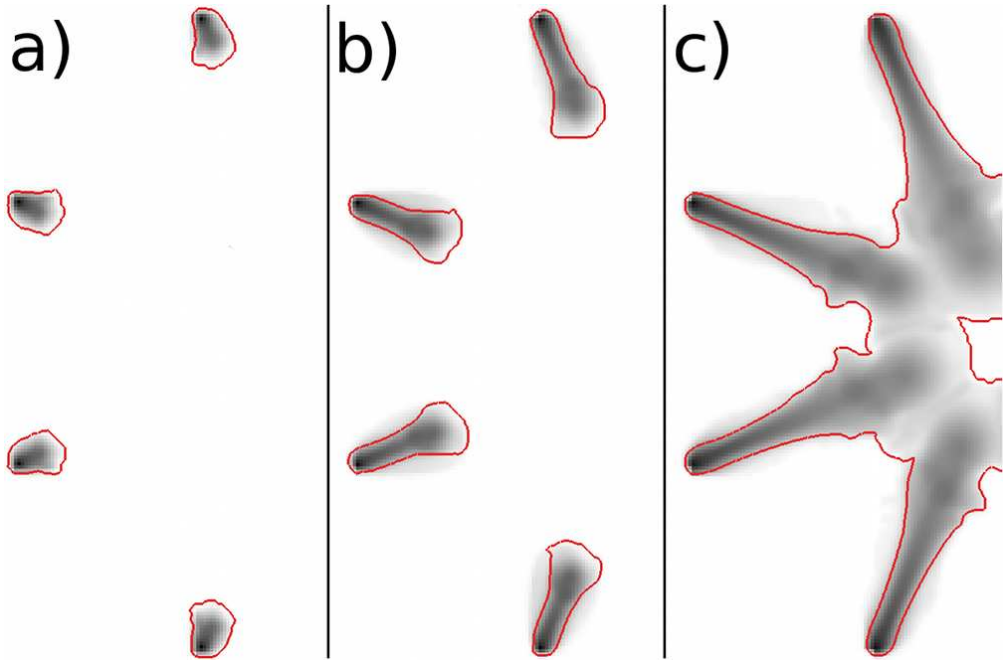


Figure 5.6: Contour for plasma $\beta = 1$ surface in red with log mass density in gray-scale at a) 20 ns, b) 60 ns, and c) 80 ns. Array axis is on the right side in each case.

That is the $\mathbf{J} \times \mathbf{B}$ force is opposite to the plasma pressure force and tends to compress the plasma. Thus plasma expansion can only occur as a result of plasma pressure for conditions in which the plasma and magnetic field are sufficiently decoupled.

The model describing the propagation of the plasma-vacuum interface consists of the one-dimensional resistive MHD equations using a polytropic equation of state for a slab geometry which we write in conservation form where

$$\partial_t \rho = -\partial_x (\rho u_x) \tag{5.5}$$

$$\partial_t(\rho u_x) = -\partial_x\left(\rho u_x^2 + P + \frac{B^2}{2\mu_0}\right) \tag{5.6}$$

$$\partial_t U = -\partial_x\left[u_x\left(\frac{\rho u_x^2}{2} + \frac{\gamma P}{\gamma - 1}\right) - E_z B_y\right] \tag{5.7}$$

$$\partial_t B_y = \partial_x E_z \tag{5.8}$$

$$E_z = -u_x B_y + \eta J_z \tag{5.9}$$

With the total energy $U = \frac{\rho u^2}{2} + \frac{P}{\gamma-1} + \frac{B^2}{2\mu_0}$, we may replace energy conservation by the pressure equation in the form

$$\partial_t P + u_x \partial_x P + \gamma P \partial_x u_x = (\gamma - 1)\eta J_z^2 \tag{5.10}$$

For the above equations, $\rho$ is the mass density, u the velocity, P the pressure, B the magnetic field, E the electric field, $\gamma$ the adiabatic index, and $\eta$ is the plasma resistivity. We desire to make progress analytically so we invoke simplifying assumptions and scaling arguments based on the form of the model. We assume a diffusion process in which pressure force increases due to Ohmic heating to drive the plasma flow through the magnetic field by diffusion.

The simulations were performed with a dimensional reference for time was 5 ns, length scale was 1 mm, and mass density was $2.7 g/cm^3$. The reference flow velocity is equal to the reference Alfvén velocity at 200km/s.

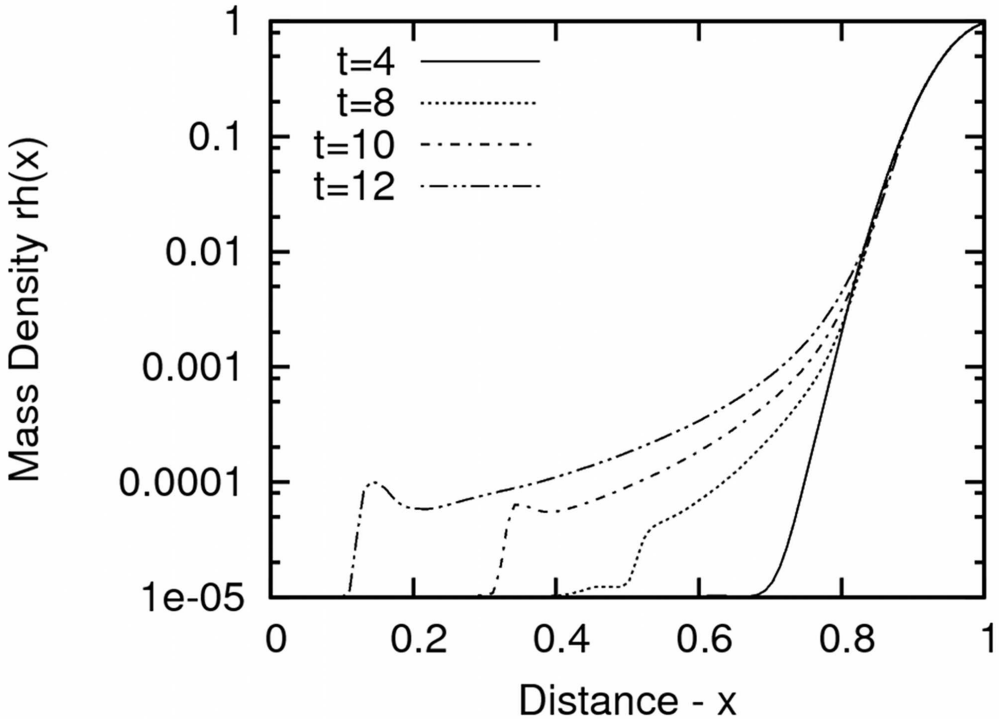


Figure 5.7: Time evolution of mass density for vacuum expansion simulation. The $sin^2(t)$ driver increases until t=8 and is then held constant.

For this model we have used a resistivity of the form

$$\eta = \eta_0 \left(1 + \frac{V\rho_0}{\rho}\right) \tag{5.11}$$

where $\eta_0$ is a constant resistivity of the plasma, $\rho_0$ is the floor density, $V$ is the vacuum resistivity, and $\rho$ is the plasma density. For the case shown in Figures 5.7-5.8 we have used $\eta_0 = 0.5$ and $V = 100$. This particular model, having the inverse dependence of the vacuum resistivity on the plasma density, is typical of resistive MHD codes such as GORGON. Shown in Figure 5.7 is a sequence of the log of plasma density at four time intervals. The initial density profile is a Gaussian whose amplitude varies from 1E-5 to 1 times peak density. The density

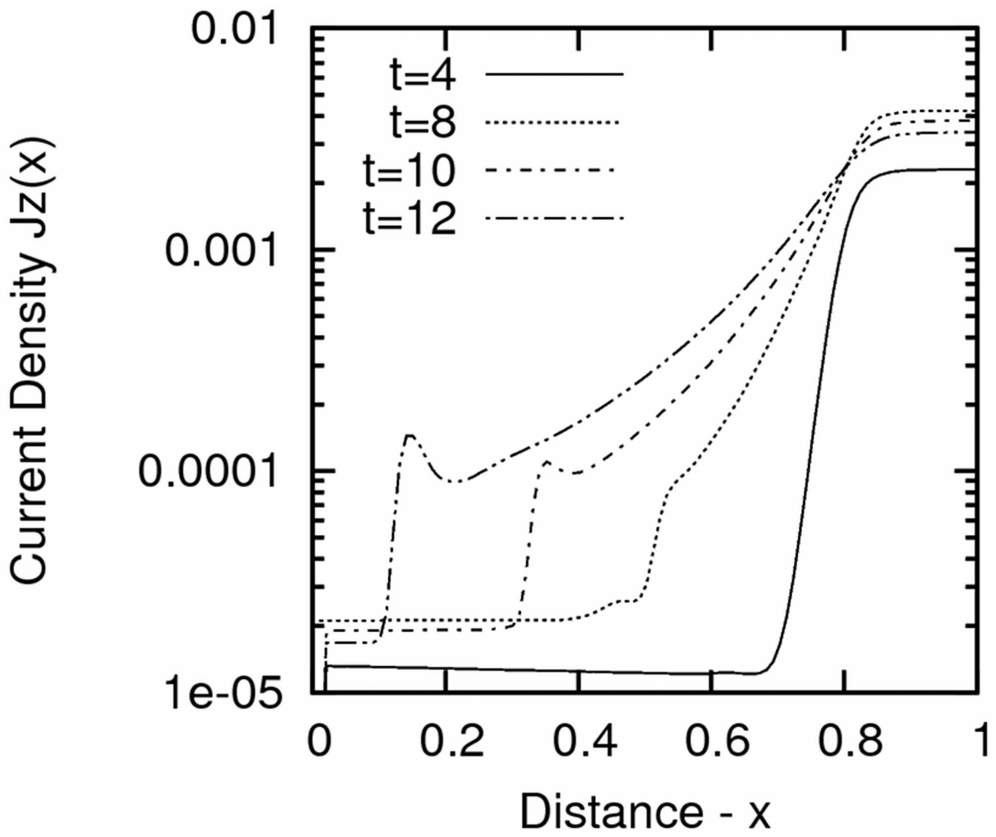


Figure 5.8: Time evolution of current density for plasma expanding into a vacuum. Current is confined to regions of plasma density above 1E-5 through use of vacuum resistivity.

has formed a jump which is about ten times the floor density. The velocity of the plasma-vacuum interface is approximately twice the sound speed. In Figure 5.8 is the plasma current which is seen to follow the plasma-vacuum interface. The acoustic speed is about 0.05 in dimensionless units, which for the reference parameters given above corresponds to about 10 km/s.

We have shown using one-dimensional simulations that plasma expansion into a vacuum is due to plasma pressure, which is against the direction of the $\mathbf{J} \times \mathbf{B}$ force, and takes the form of a propagating jump in density, pressure, and current corresponding to a plasma beta jump up to a value close to unity. Our

results are entirely consistent with earlier work on the subject. We now make the argument that the same process occurs in the two-dimensional wire array geometry and show this to be the case by tracking the $\beta = 1$ surface that characterizes the plasma-vacuum interface as it did in the one-dimensional simulations. Figure 5.6 gives the plasma $\beta = 1$ contour for three different times during the initial mass expulsion for the GORGON simulation. This surface where magnetic and gas pressure are equal traces the front of both the coronal radius of each wire and the leading edge of the vacuum interface that brings the first plasma to the array axis. This shock-like structure carries the current that alters the field around the core which reverses the magnetic field through the core leading to streaming ablation.

We can exploit this observation that the high density plasma lies within the $\beta = 1$ surface where beta is larger than unity. We define the coronal radius as the distance from the wire where the local beta is unity.

$$P = \frac{B^2}{2\mu_0} \tag{5.12}$$

We can use this relation to determine the scaling of the coronal radius, $a$, using appropriate dimensional forms for the magnetic field and the pressure.

The scaling of the global magnetic field at the coronal radius $B_a$ is found from Ampere's law $B_a \sim \mu_0 I/a$, and the pressure at $a$ due to Ohmic heating scales as

$$P_a \sim \frac{(\gamma - 1)\eta}{a^4} \int_0^t I^2(t')dt' \tag{5.13}$$

which is inferred from Equation 5.10 and the scaling of the current density $J_a \sim$

$I/a^2$. The coronal radius is determined from the definition

$$P_a \equiv \frac{{B_a}^2}{2\mu_0} \tag{5.14}$$

We introduce a dimensionless constant $C$ determined by simulation or experiment such that the definition Equation 5.14 holds given the scalings of $B_a$ and $P_a$. The coronal radius is then found to be

$$a = C\sqrt{\frac{(\gamma-1)\eta}{\mu_0 I^2}\int_0^t I^2(t')dt'} \tag{5.15}$$

In most simulations and Z-pinch modeling, the current time function is taken to be of the form $I(t) = I_0 \sin^2(\pi t/2\tau)$ where $I_0$ is peak current at the rise time $\tau$. Using this function we find the integral in Equation 5.15 is approximately

$$f(t) = \frac{1}{I^2}\int_0^t I^2(t')dt' \approx \frac{t}{5} + \frac{\pi^2 t^3}{105\,\tau^2} \tag{5.16}$$

which is very accurate for $t < 0.6\,\tau$. Thus we have

$$a(t) = C\sqrt{\frac{(\gamma-1)\eta f(t)}{\mu_0}} \tag{5.17}$$

The expression for the coronal radius Equation 5.17 can only be expected to hold for times well less than the time to the onset of ablation and to only characterize the distance to the $\beta = 1$ boundary outside the array radius from the wire core. At the end of this approximately cylindrical expansion phase of

the coronal radius, the outward expansion of the coronal radius will cease as the inward motion of the discontinuity approaches the characteristic propagation speed. At this time all ablating plasma will begin to move towards the array axis. We discuss this next phase in the following section.

## 5.3 Initiation of Ablative Streaming

We have established that for the initial plasma expansion to occur, and hence high Mach number streaming ablation to follow, the Ohmic heating rate must be sufficiently fast so that plasma pressure exceeds the compressive magnetic pressure in a region where the plasma flow decouples from the magnetic field. For this case, we expect that the plasma density and hence the current will propagate as an acoustic wave towards the array axis. In order to arrive at a predictive relation for this process to occur, several factors must be taken into account. Initially we expect that plasma pressure will lag magnetic pressure, and thus the coronal plasma will pinch down towards the wire. Eventually the plasma pressure will locally exceed the magnetic pressure since heating is increasing with time faster than magnetic pressure. If the heating rate is sufficiently fast, then the plasma will expand enough within the current rise time to initiate the streaming ablation process. The heating rate depends upon $\eta$, $\gamma$, the scale length of the current density in the corona, and the current rise time. These conditions affect the total pressure force that initiates the ablative flow.

The ablation stream will begin to form when the current density has penetrated sufficiently far towards the array axis. The time required to penetrate this critical distance ($d_c$), which we call the penetration time ($t_c$), depends on

the propagation speed of the plasma into a vacuum, which as we have seen depends upon the acoustic speed and is approximately $2c_s$. The dynamics of the expansion of a plasma into a vacuum has been previously explored by [68]. An estimate of the penetration time is $t_c \approx d_c/2c_s$, where $c_s$ is the acoustic speed behind the front of the discontinuity. If it happens that the penetration time is greater than the implosion time then ablative streaming cannot occur.

There is another condition that must be satisfied in order to access the ablative streaming regime. This condition is that is the Ohmic heating rate must be sufficient that the $\beta = 1$ transition from vacuum to plasma is achieved. We argue that the $\beta = 1$ criterion imposes restrictions on array parameters that allow access to the ablative streaming regime. Firstly we postulate that the critical distance to which the current must expand towards the array axis to allow the onset of ablation streaming will scale with the array radius $R$. This seems to be the only possibility from a dimensional analysis perspective. Thus we assume the critical distance scales as $d_c \sim Rg(m)$, where $g(m)$ is some function of the wire number. The simplest reasonable possibility is that $g(m) = 1/m$.The critical distance provides the length of a current sheet whose magneto-static solution has only magnetic field in the global direction intersecting the core corona structure.

We can test this relation by the following procedure. Using a code that computes the static field configuration based on a resistivity distribution and an imposed magnetic field on the boundary we can drive currents in any desired configuration. We model the current distribution of an ablating array by taking a constant resistivity in a region consisting of a wire core and a strip extending a distance $d$ from the core towards the array axis. We vary the distance $d$ for a fixed wire number and determine the value of $d$ at which the last closed mag-

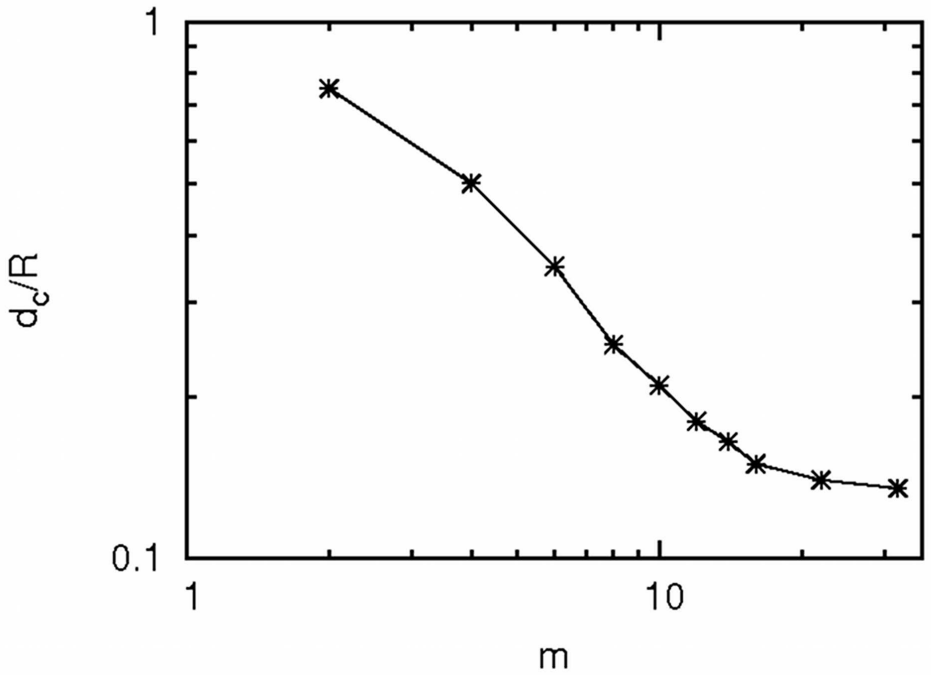


Figure 5.9: Plot of critical penetration distance $d_c$ of a current strip versus wire number $m$ required to create open magnetic flux at the core.

netic flux contour falls inside the wire core. We call this distance $d_c$, the critical distance to which the ablation stream must penetrate to open the magnetic geometry to access the $\mathbf{J} \times \mathbf{B}$ regime. This is done for a number of configurations with different wire numbers $m$. Shown in Figure 5.9 is a log-log plot of the ratio $r_c/R$ versus $m$. For wire numbers in the range $4 \leq m \leq 16$ Figure 5.9 shows that $d_c$ scales inversely with $m$. For $m > 16$, the $d_c$ asymptotes to a constant fraction of the coronal radius. The result confirms our expectation that for small wire numbers the approximate scaling of the critical penetration distance is $d_c \sim R/m$. For a constant number of wires, the critical distance also scales with the coronal radius. For arrays with core radius much smaller than the coronal radius, as the coronal radius of each wire is increased the global field will completely envelop an ablating core when the inter-wire gap is of order the coronal diameter.

If the Ohmic heating rate is sufficient to allow the plasma pressure to support the magnetic field at $d_c$ within a time comparable to the implosion time, then

$$P_c > \frac{{B_c}^2}{2\mu_0} \tag{5.18}$$

where $P_c$ and $B_c$ are the pressure and magnetic field at the critical distance $d_c$. If condition 5.18 is satisfied within an implosion time we expect that ablative streaming will occur. We arrive at an explicit condition by assuming the following scalings

$$P_c \sim \frac{(\gamma - 1)\eta}{d_c^4} \int_0^t I^2(t')dt' \tag{5.19}$$

$$B_c \sim \frac{\mu_0 I}{d_c} \tag{5.20}$$

Then a condition for ablative streaming ($\mathbf{J} \times \mathbf{B}$ ablation regime formation) is

$$\frac{(\gamma - 1)m^2\eta f(t)}{\mu_0 R^2} > C' \tag{5.21}$$

for a time $t < t_{imp}$. The constant $C'$ is empirically determined from simulation or experiment. If the condition 5.21 is not satisfied then the Ohmic heating rate is too slow to allow expansion of the corona towards the array axis during an implosion time and we expect that the corona will pinch back towards the wire.

We summarize the results of this section. One-dimensional simulations show that an ablation front makes a transition to unity beta. We define the out-

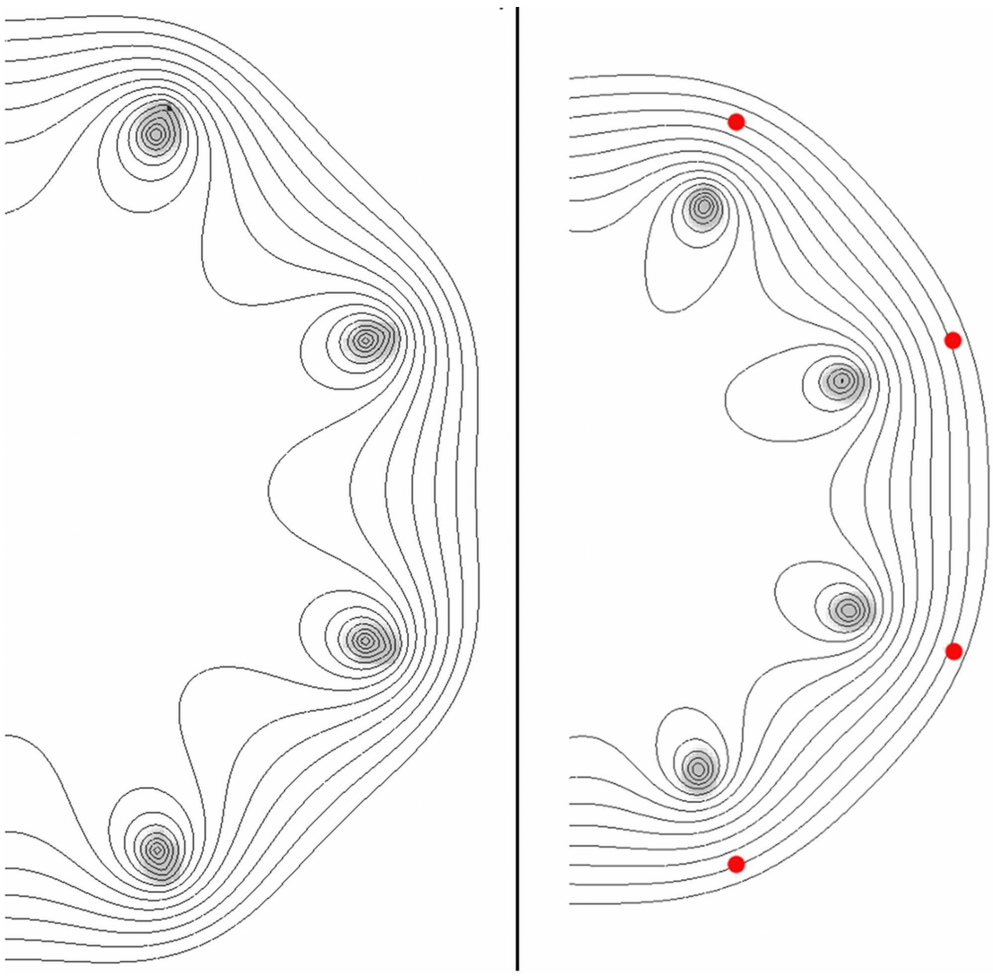

Figure 5.10: (Color online) Magnetic vector potential ($A_z$) and mass density in gray-scale for Run 6 at 84 ns. The wires are still located in their original position. The ablation constraint (Equation 5.15) is not satisfied due to the array radius being doubled (left). The $\mathbf{J} \times \mathbf{B}$ ablation regime never occurs and the wires implode discretely without ablating at 140 ns. Red dots show position of wires at t=0 (right).

side coronal radius to be the point at which unity beta is achieved. The distance to which the plasma must diffuse towards the axis to allow magnetic configuration change scales as $R/m$. The position of the $\beta = 1$ front scales as $\sqrt{t}$. If the Ohmic heating rate is not sufficiently fast the plasma will not penetrate this distance within an implosion time and the coronal plasma will self-pinch. The

Table 5.1: Runtime parameters for GORGON test of ablation constraint Equation 5.15 on 12.5$\mu$ aluminum wire array.

| Run ID | Current Drive Waveform | $R_m$ Multiplier | $\frac{R}{m}$ (mm) | $m$ | JxB ablation regime formed |
|---|---|---|---|---|---|
| Run 1(reference case) | $\sin^2$ rise to $1MA$ peak in 100ns | 1 | 1.25 | 8 | True |
| Run 2 | $\sin^2$ rise to $1MA$ peak in 100ns | 4 | 1.25 | 8 | False |
| Run 3 | $\sin^2$ rise to $1MA$ peak in 100ns | 4 | 0.625 | 16 | True |
| Run 4 | exponential rise to $0.1MA$ peak in 25ns | 1 | 1.25 | 8 | False |
| Run 5 | exponential rise to $0.1MA$ peak in 100ns | 1 | 1.25 | 8 | True |
| Run 6 | $\sin^2$ rise to $1MA$ peak in 100ns | 1 | 2.50 | 8 | False |

result is discrete wire-like implosion, a structure with 0D trajectory and no ablative streaming [Figure 5.10]. In the next section we test these results using the GORGON MHD code.

## 5.4 GORGON Test of Ablation Transition

Relation (5.21) can be easily violated and can be tested by computer simulation. We present results from GORGON in which all the adjustable parameters were varied to test the prediction for a transition into the $\mathbf{J} \times \mathbf{B}$ ablation stream acceleration regime. The testing proceeds as follows: We first establish the base case (run 1) in which normal ablation and acceleration occurs (see Table 5.1 for simulation parameters). Next we decrease the resistivity until we find no transition into the $\mathbf{J} \times \mathbf{B}$ ablation regime and the array implodes as discrete wires without ablation streams. We find that this happens when the resistivity is reduced by about a factor of four. From run 2 we can determine the constant $C'$ to be close to unity.

In run 3 we use this 4x reduced resistivity together with doubling the number of wires from 8 to 16, for which Equation (5.21) predicts a transition to the

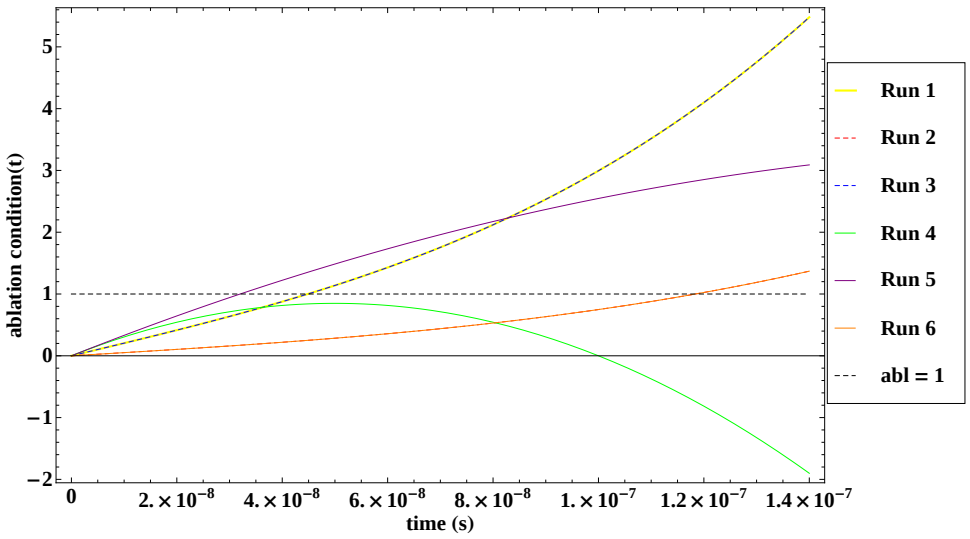


Figure 5.11: Plot of the discrete wire implosion criterion versus time for simulations labeled in Table 5.1.

$\mathbf{J} \times \mathbf{B}$ ablation regime configuration. We indeed find that this does occur. At this point we have tested the prediction of the $\mathbf{J} \times \mathbf{B}$ ablation regime transition with respect to resistivity and wire number.

Next we compare run 4 and run 5, which have an exponentially increasing current rise. For run 4 we have a 25 ns rise to 0.1 MA and in the other a 100 ns rise to 0.1 MA (run 5). We compare the two runs and find that the case with the faster rise and larger current (run 4) has not entered the $\mathbf{J} \times \mathbf{B}$ ablation regime, whereas the slower rise time case (run 5) is ablating normally. This is in agreement with the I dot scaling prediction.

Finally, in run 6 we consider the base case but double the array radius from 1 cm to 2 cm. This modifies the geometric factor such that the array should not ablate. For this case we needed to double the spatial resolution to keep the numerical resistivity the same between the two runs. We find that the case with larger array radius does not enter the $\mathbf{J} \times \mathbf{B}$ ablation regime.

## 5.5 Conclusions of Resistive MHD Analysis Using GORGON Code

In this chapter have investigated the role of a cylindrical wire array's magnetic configuration in the onset of streaming ablation. From this analysis, we determine that the $\mathbf{J} \times \mathbf{B}$ acceleration of high Mach number ablation streams requires a transition of the magnetic field from a vacuum configuration where local field surrounds the coronal plasma to an ablation field configuration where only global field intersects the core-corona structure, creating a collimated acceleration of plasma toward the geometric axis of the array. This ablation configuration is achieved through a uniform current sheet extending from the corona in the direction of the array axis with minimum length equal to the critical distance, $d_c$, which is the ratio of array radius to number of wires. Since a vacuum resistivity constrains current flow to the plasma density, the propagation of a plasma-vacuum interface past the critical distance is a necessary condition for fully developed ablation streams. In resistive MHD, radially inward expansion of the plasma-vacuum interface originates from $\mathbf{J} \times \mathbf{B}$ momentum production in the vacuum configuration and thermal expansion from Joule heating of the plasma. For low magnetic Reynolds number flows, the dominant mechanism is thermal expansion where the vacuum interface is defined by a $\beta = 1$ surface, with $\beta > 1$ inside the plasma. The propagation velocity is determined from resistive decoupling of the flow from the magnetic field. The conclusions presented provide a picture of the physical evolution of a wire array in the time after breakdown through the onset of ablation.

The analytic model introduced relates the rate of change over time of the

current driver, the plasma resistivity, and the geometry of the array to the condition that pressure from Joule heating of the plasma must overcome the magnetic pressure trying to pinch the wire. This criterion for ablative streaming is in agreement with resistive MHD simulation for the cases presented. Important details still exist that must be explored further. We note that the simulation and analysis of this chapter only considers the two-dimensional picture of the transition to ablation in the x-y plane while three-dimensional simulation results show a layered structure along the z-axis due to the axial instability. It is uncertain what role this inhomogeneity will play when extending these ideas to higher dimension. These results stress the importance of the plasma-vacuum interface in determining the evolution of the ablation streams and thus the overall dynamics of wire arrays. As discussed in Chapter 2, the proper treatment of the interface requires the inclusion of finite electron mass. In the next chapter we will revisit the 1D plasma-vacuum interface results with our generalized Ohm's law model.

CHAPTER 6

# TWO-FLUID PHYSICS OF THE WIRE ARRAY ABLATION FRONT

In the previous chapter we explored the evolution of the plasma-vacuum interface for a plasma slab in sheet pinch configuration under the resistive MHD model. We now revisit this problem with our generalized Ohm's law-Maxwell model. The overall picture resulting from our resistive MHD simulations, that the magnetic configuration change is a requirement for streaming wire ablation, still applies under the two-fluid model. However, the specifics of the propagation of the plasma-vacuum interface differ. Thus, by comparing the evolution of the plasma-vacuum interface as represented by the single-fluid resistive MHD model and the reduced two-fluid model, we can understand the impact of the separate ion and electron physics on the overall ablation dynamics of wire arrays.

## 6.1 Electron Inertia Current Limited Flow in Sheet Pinch

We begin our study by initializing the 1D computational domain with a Gaussian distribution for the number density whose peak value corresponds to cold solid density aluminum. The domain size is 1 mm in length and is divided into 400 cells. A sine squared driver that reaches 1 MA peak in 100 ns is applied though the magnetic boundary conditions to the system. The current is all concentrated in the slab and it immediately begins to heat with an assumed constant adiabatic index of 1.14 and expands into the vacuum. We concentrate on the expansion phase, when the gas pressure sourced from Joule heating is greater than the magnetic pressure. Unlike the previous study, we do not turn

Table 6.1: List of reference dimensional numbers.

| Variable Name | Variable Symbol | Dimensional Reference ($\Xi_0$) |
|---|---|---|
| Length | $L_0$ | 1.0 mm |
| Time | $t_0$ | 1.0 ns |
| Number density | $n_0$ | 6.0x$10^{22}$ cm$^{-3}$ |
| Velocity | $V_{a0}$ | 1.0x$10^{4}$ m s $^{-1}$ |
| Magnetic field | $B_0$ | 580 T |
| Electric field | $E_0$ | 5.8x$10^{6}$ V m$^{-1}$ |
| Current density | $j_0$ | 4.6x$10^{11}$ A m$^{-2}$ |
| Temperature | $T_0$ | 14 eV |
| Resistivity | $\eta_0$ | 1.3x$10^{-5}$ ohm-m |
| Electron inertial length | $\lambda_{e0}$ | 22 nm |
| Ion inertial length | $\lambda_{i0}$ | 4.8 microns |
| Electron cyclotron frequency | $\Omega_{e0}$ | 1.0x$10^{14}$ rad s$^{-1}$ |
| Hall velocity | $V_{h0}$ | 48 m s$^{-1}$ |

off the driver early on and track the expansion over the first 20 ns.

The simulations are performed using the dimensionless generalized Ohm's law Maxwell system of Equations 2.8 - 2.18. For the rest of this thesis, the results will be presented in the dimensionless variables. We now list the reference dimensional variables for aluminum in Table 6.1, where for any parameter $\Xi$, $\Xi_{dimensional} = \Xi_{dimensionless}\, x\, \Xi_0$.

In Figure 6.1 we see the evolution versus time for the plasma number density

in a sheet pinch configuration. All of these simulations are performed on a dimensionless system where a number density of 1 corresponds to a dimensional value of $6x10^{22}$ $cm^{-3}$. The reference length scale is 1 mm, the time scale is 100 ns, and the equations are non-dimensionalized with respect to the Alfven velocity. The resistivity for this simulation is a constant $10^{-5}$ ohm-m throughout the entire domain. As expected, the current density is confined to the column as shown in Figure 6.2 through the inclusion of finite electron inertia in the system. The current density has the same profile as the number density, in agreement with the predicted analytic scaling proportional to the inertial lengths squared or one over the number density. These two figures confirm that an anomalous resistivity is not required to constrain the current to follow the density. Instead, the two-fluid physics of the generalized Ohm's law model limits the flow of current at low number densities due to the lack of charge carriers. Finally, in Figure 6.3 we see the temperature of the plasma versus time. A value of 1 corresponds to a dimensional value of 14 eV.

## 6.2 Two-Fluid model versus Resistive MHD model in Slab Geometry

We now compare the evolution of the number density and current density profiles between three plasma-vacuum interface models. The MHD model will be defined as a constant internal resistivity with an instantaneous increase in resistivity by a factor of $10^5$ when the number density falls below a predefined cutoff value of $10^{-9}$. In this model, the current density results from the steady state solution of a system where the magnetic field is applied on the bound-

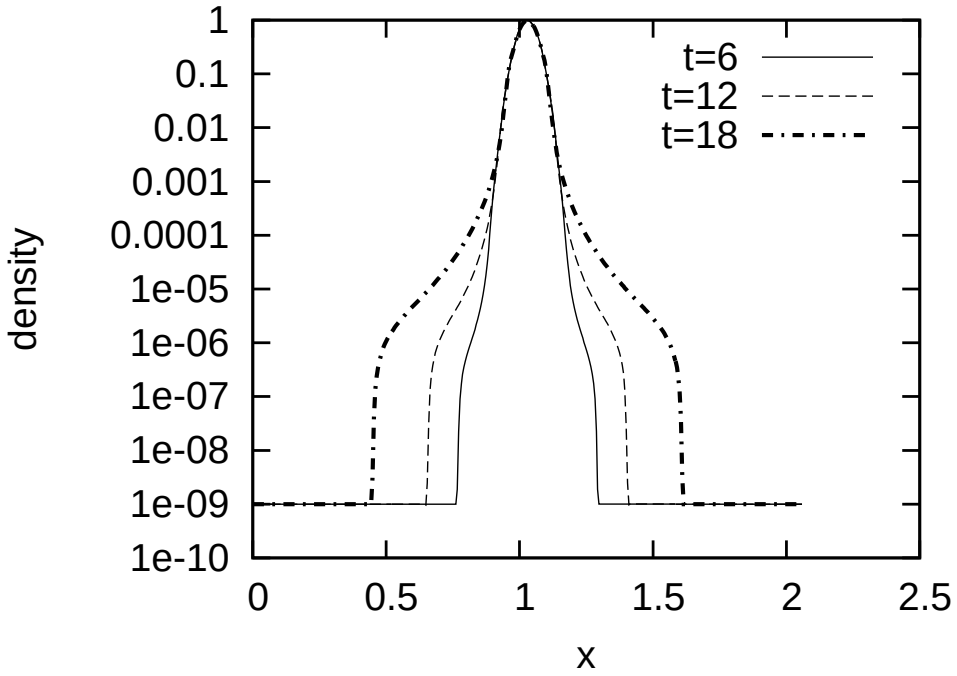


Figure 6.1: Log10 plot of number density at 6 ns, 12 ns, and 18 ns for two-fluid sheet pinch simulation.

ary then propagates through an infinitely resistive vacuum, finally driving current in the plasma located in the center of the simulation domain. Thus, the plasma-vacuum interface is defined through an infinite jump in resistivity beyond the Spitzer value for number densities below a numerical density floor value. The second model is labeled as the vacuum resistivity (VRES) model which is similar to the MHD model except that the transition to resistive background is smoothed with a $1/n$ transition. The explicit form of this resistivity is given by Equation 5.11. This dependency on the inverse or square root of the inverse of the number density is usually invoked for numerical convenience or in an attempt to include the collisional effects of micro-instability. We also consider the generalized Ohm's law electron inertial (EI) limitation of current flow at the interface. Figure 6.4 shows the resultant number density distribution 6 ns

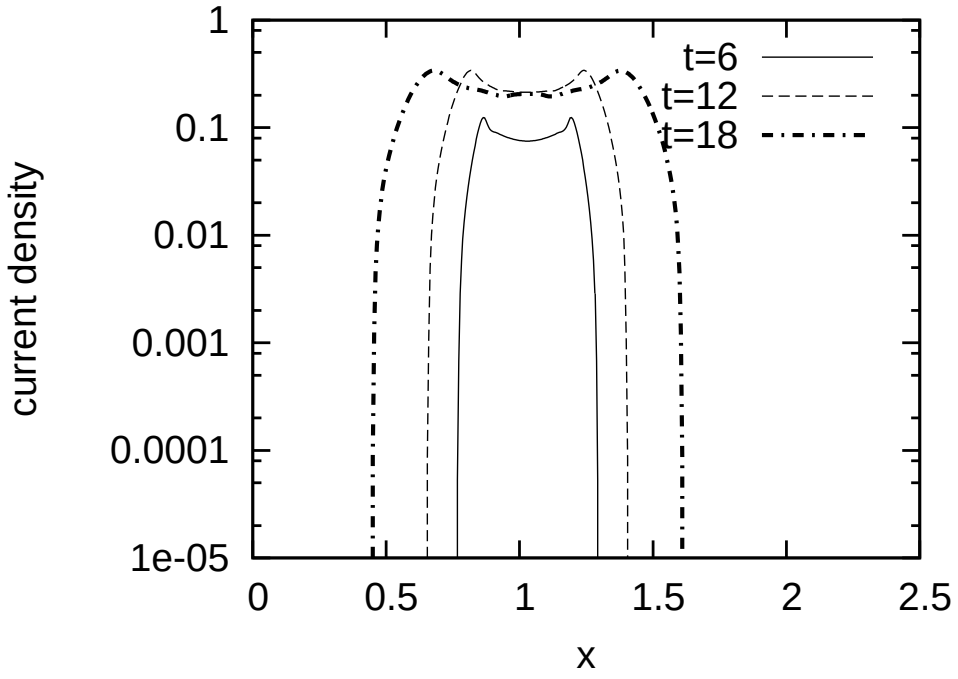


Figure 6.2: Log10 plot of current density at 6 ns, 12 ns, and 18 ns for the two-fluid sheet pinch simulation.

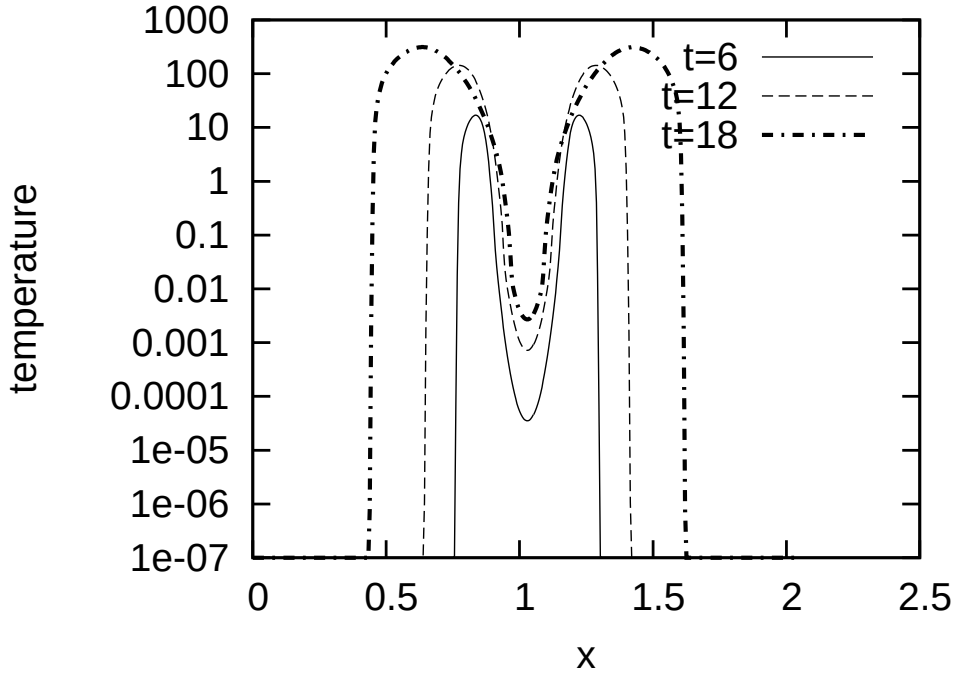


Figure 6.3: Log10 plot of temperature at 6 ns, 12 ns, and 18 ns for the two-fluid sheet pinch simulation.

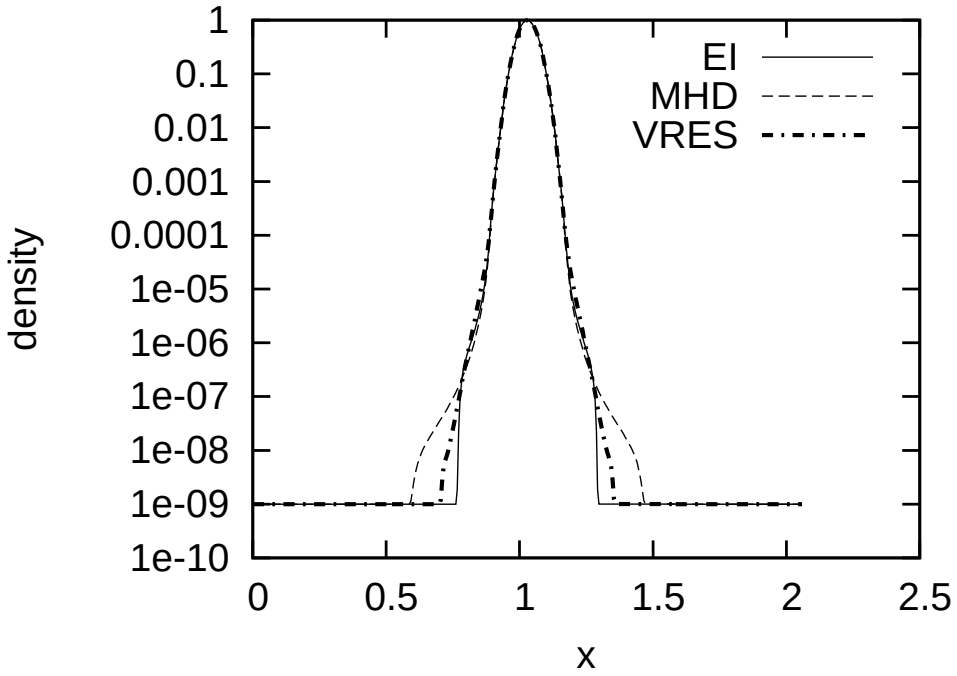


Figure 6.4: Log10 plot of the number density profile for sheet pinch simulation at 6 ns with constant internal resistivity and with current flow limited by electron inertia (EI), vacuum resistivity with instantaneous jump to $10^5$(MHD), and vacuum resistivity increasing with inverse number density dependence (VRES) to a peak value of $10^5$.

after the driver has been turned on to the plasma slab. From this figure it is apparent that each model gives a different propagation velocity for the plasma-vacuum interface. The MHD model gives the fastest expansion velocity. The MHD model uses an instantaneous jump in vacuum resistivity below the cutoff density threshold to represent the interface and confine current to the plasma column. However, this overestimates the amount of current density that the surface plasma can carry. This in turn increases the Joule heating rate and thus the expansion velocity of the interface beyond the other two models. The inverse number density dependency for the vacuum resistivity model moves the density distribution closer to the electron inertia limiting case. This result indi-

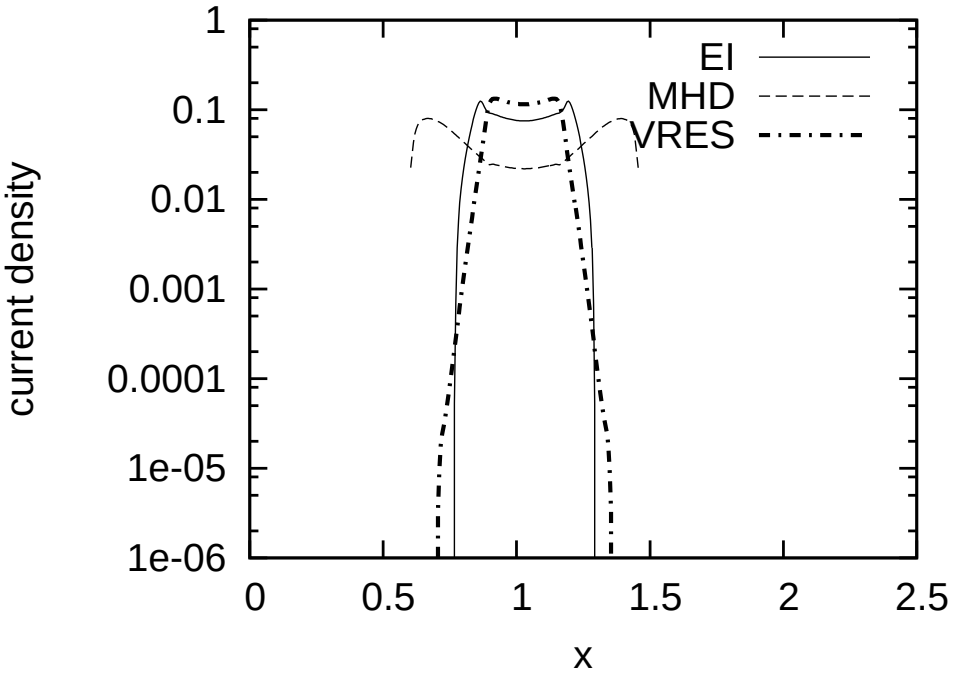


Figure 6.5: Log10 plot of the current density profile for sheet pinch simulation at 6 ns with constant internal resistivity and with current flow limited by electron inertia (EI), vacuum resistivity with instantaneous jump to $10^5$(MHD), and vacuum resistivity with inverse number dependence (VRES).

cates that if the modeling is limited to Resistive MHD, two-fluid theory could be used to generate an anomalous resistivity profile that approximates a collisionless plasma-vacuum interface. On the surface this seems counterintuitive, applying an anomalous collisionality to approximate the interface physics of a collisionless plasma. However, collisions are the only way in which Resistive MHD can limit current flow and thus the only way to tailor the current distribution in the system.

In Figure 6.5 the current density profiles are given for the three models. The current density distribution resultant from the MHD model is peaked near the density floor cutoff. The VRES model results in almost an order of magnitude

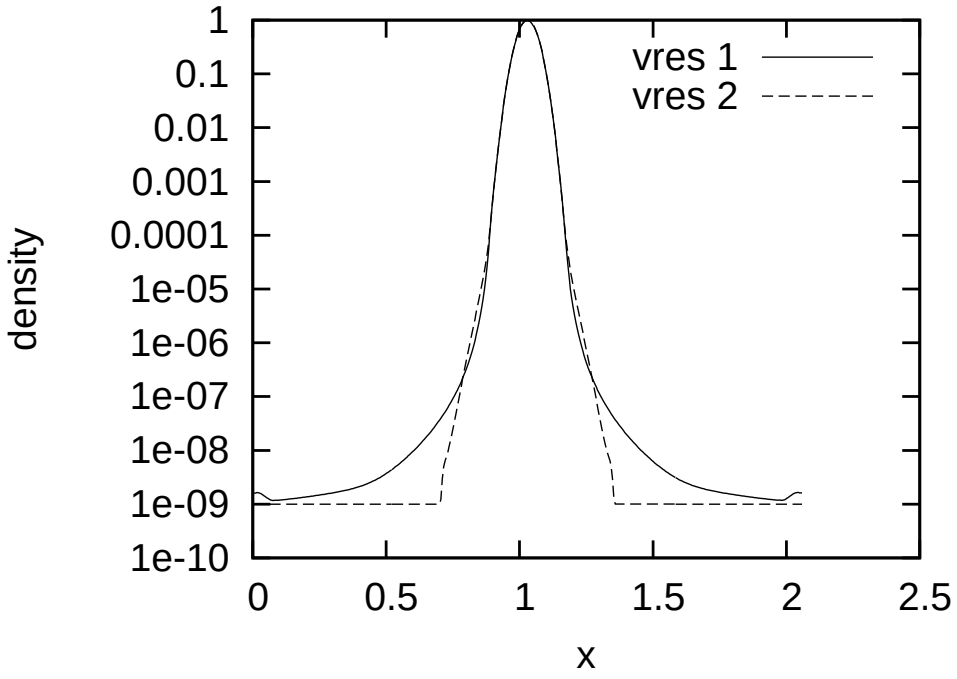


Figure 6.6: Log10 plot of the number density profile for vacuum resistivity at 6 ns with inverse dependence on number density for maximum resistivity of $10^3$ (vres1) and maximum resistivity of $10^5$ (vres2).

greater peak current density in the slab. Finally, the EI model results in an almost uniform distribution of current in the slab, with slight peaks near the interface. These results indicate that under the resistive MHD approximation, the evolution of the plasma slab is determined by the profile of anomalous resistivity. Though invoking anomalous collisionality it may be possible to tailor the results to match experiment, but no unique solution exists. This is to be expected since resistive MHD representation of a plasma is outside its regime of validity for plasma flows characteristic of the vacuum interface region. We next explore the evolution of the slab for the VRES model with varying peak magnitudes.

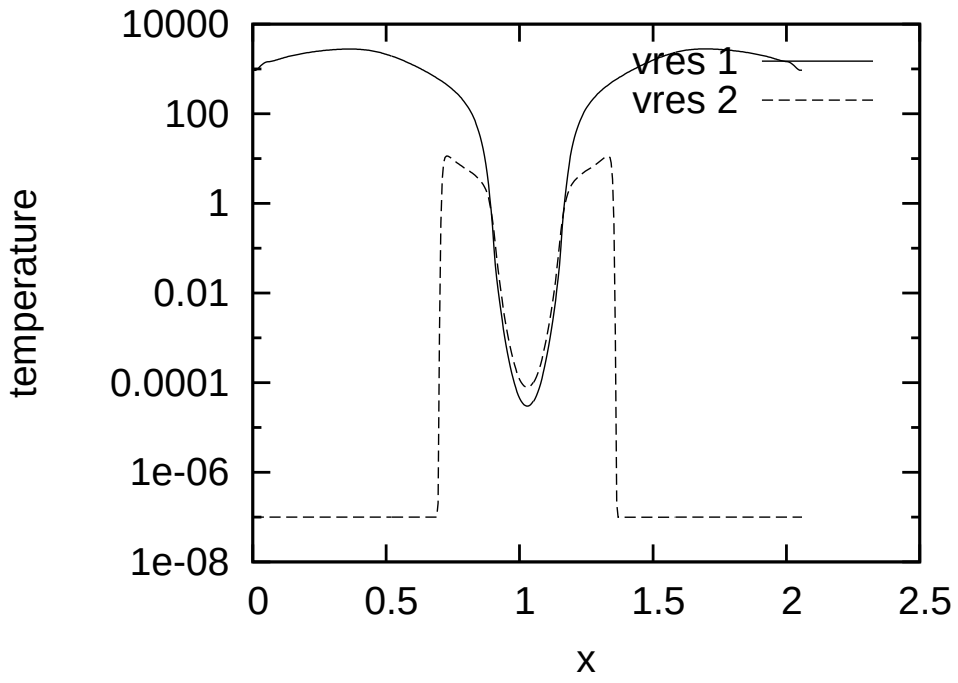


Figure 6.7: Log10 plot of the temperature profile for vacuum resistivity at 6 ns with inverse dependence on number density for maximum resistivity of $10^3$ (vres1) and maximum resistivity of $10^5$ (vres2).

We further test the idea that resistive MHD does not provide a unique and physical answer for the interface problem by decreasing the peak value of the anomalous resistivity from $10^{-5}$ to $10^{-3}$. Due to the instantaneous resistivity jump in the MHD model, we will not consider this case since it is assumed that a large enough resistivity is picked that the resultant current distribution is due to the steady state profile. However, we can still comment on the uniqueness of the MHD model since it requires application of a density floor to define the jump. From the point of view of the magnetics, there is a unique solution corresponding to the steady solution, however the density floor is an arbitrary and required numerical artifact under this model. By picking the density floor, we pick the heating rate of the plasma-vacuum interface since the resultant distri-

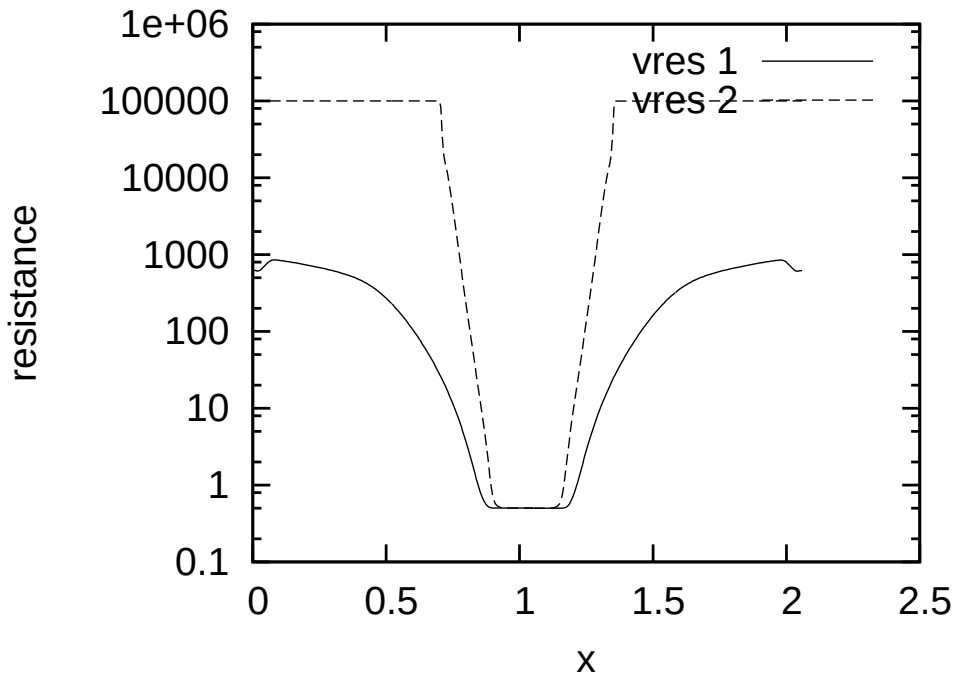


Figure 6.8: Log10 plot of the resistivity profile for vacuum resistivity at 6 ns with inverse dependence on number density for maximum resistivity of $10^3$ (vres1) and maximum resistivity of $10^5$ (vres2).

bution of current density inside the plasma is dependent on the range of densities. For the inverse number dependency (VRES) case, both the density floor and the magnitude of the vacuum resistivity will effect the current distribution. Figure 6.6 shows the difference in the number density profiles 6 ns after turning on the 1 MA driver. The rate of expansion of the plasma slab changes with the peak magnitude of the vacuum resistivity. Additional differences are apparent when changing the magnitude of the vacuum resistivity as seen in Figure 6.7. Both peak values give a numerical steady state current distribution for the system, but the inclusion of the anomalous resistivity inside the plasma changes its evolution. For the $10^{-3}$(vres1) case the plasma has expanded to the wall and has heated orders of magnitude beyond the $10^{-5}$(vres 2) case. This thermal runaway

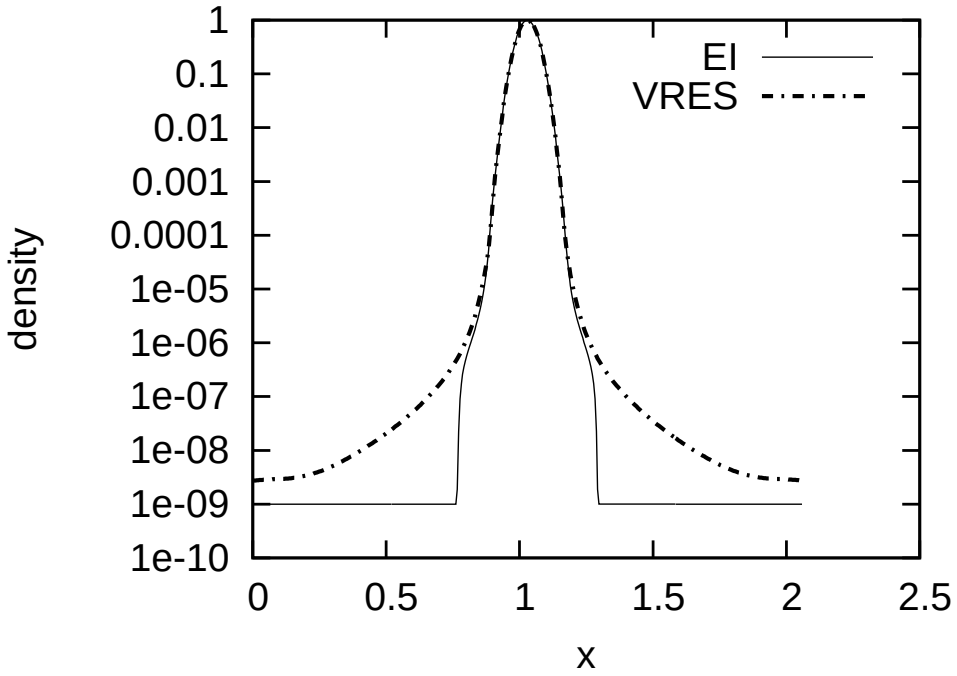


Figure 6.9: Log10 plot of the number density profile for sheet pinch simulation at 6 ns with variable internal Spitzer resistivity along with current flow limited by electron inertia (EI), vacuum resistivity with instantaneous jump to $10^3$(MHD), and vacuum resistivity with inverse number dependence (VRES).

is common when resistive MHD is used to describe flows at low number density and outside its regime of validity. Figure 6.8 shows the resistivity distribution for the two different vacuum resistivity magnitudes. Again it is apparent that by picking a density floor and vacuum resistivity, one predetermines the evolution of the system.

Our final comparison is made between the electron inertial model and the vacuum resistivity cases with a peak resistivity of $10^{-3}$. Figure 6.9 shows the difference between number density distributions 6 ns into the simulation. The two-fluid physics of the generalized Ohm's law model provides a unique current distribution independent of the floor value, whereas the vacuum resistivity

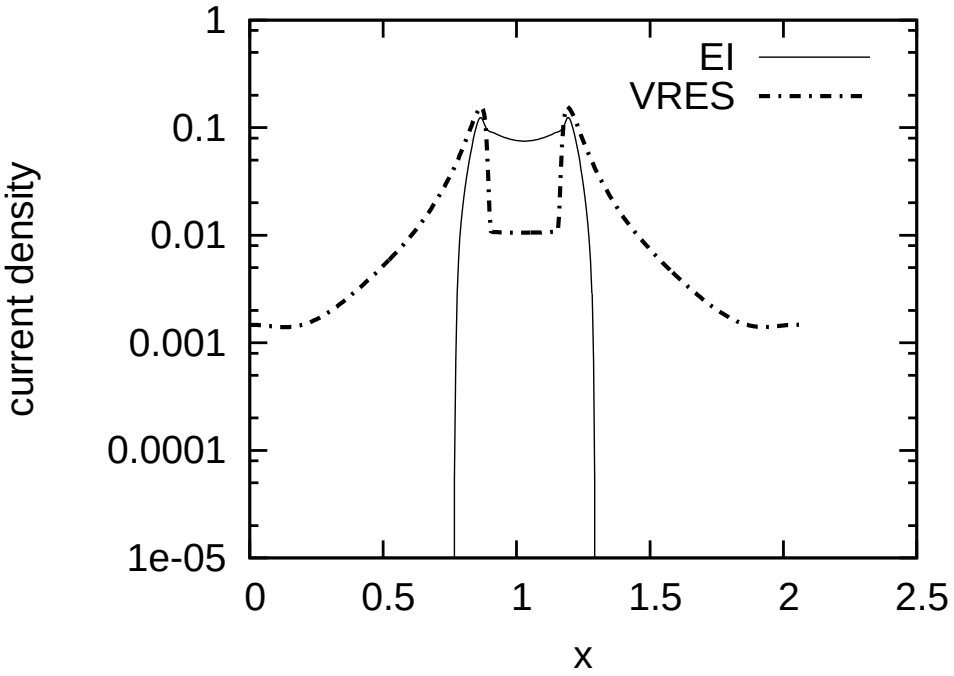


Figure 6.10: Log10 plot of the current density profile for sheet pinch simulation at 6 ns with variable internal Spitzer resistivity along with current flow limited by electron inertia (EI), vacuum resistivity with instantaneous jump to $10^3$(MHD), and vacuum resistivity with inverse number dependence (VRES).

model has a completely different expansion rate. Figure 6.10 gives the current density distribution resultant from the number densities in the previous figure. The overall conclusions from this chapter are as follows. The resistive MHD model in the presence of a plasma-vacuum interface has no unique solution due to the requirement of a density floor in the simulation. The selection of the density floor is a numerical parameter that indicates where the vacuum resistivity is to be applied, and by choosing an arbitrary value one may predetermine the current distribution inside the plasma. For the vacuum resistivity model, both the density floor and the magnitude of the vacuum resistivity act as numerical parameters that predetermine the evolution of the system. Only the two-fluid

model gives a unique answer in the presence of a plasma-vacuum interface since its current density cutoff is independent of external numerical parameters and the density floor does not change the answer as long as the inertial length is resolved at the plasma-vacuum interface.

CHAPTER 7

# WIRE ARRAY SIMULATIONS WITH TWO-FLUID RELAXATION CODE

In this chapter, we explore the physics of wire arrays under our reduced two-fluid model. We use a two-dimensional representation of the array in the x-y plane where the z dimension, along which the wires are aligned, is assumed infinite. In this geometry, we make the assumption that the wires are infinitely long, which removes the possibility of Magneto-Rayleigh-Taylor instability. Our goal is to understand the initiation of streaming ablation under the two-fluid model as we did in Chapter 5 for resistive MHD. We will ignore periodic symmetry planes for all 2D simulations in this thesis. The 1D sheet pinch simulation results of Chapter 6 suggest that the expansion rate of the coronal plasma will differ from the resistive MHD model, and that a low density background gas is sufficient to confine current flow to the wires. The first set of simulations are performed with the generalized Ohm's law model and a constant resistivity of $10^{-5}$ohm-m. Our goal is to explore the evolution of the wire array plasma under our two-fluid model without additional complexity due to variable resistivity, thermal conduction, or radiation transport. The adiabatic index is kept to a constant value of 1.14 which is reasonable for an Aluminum plasma [69].

## 7.1 Simulation of Wire Array on COBRA

The grid and initial condition for our wire array simulation is as follows. The computational domain is a square box 18 mmx18 mm in dimension, divided in to 200 cells in each direction. The wires are initialized with the line density of a 10 micron diameter aluminum wire which located in a single cell. The eight

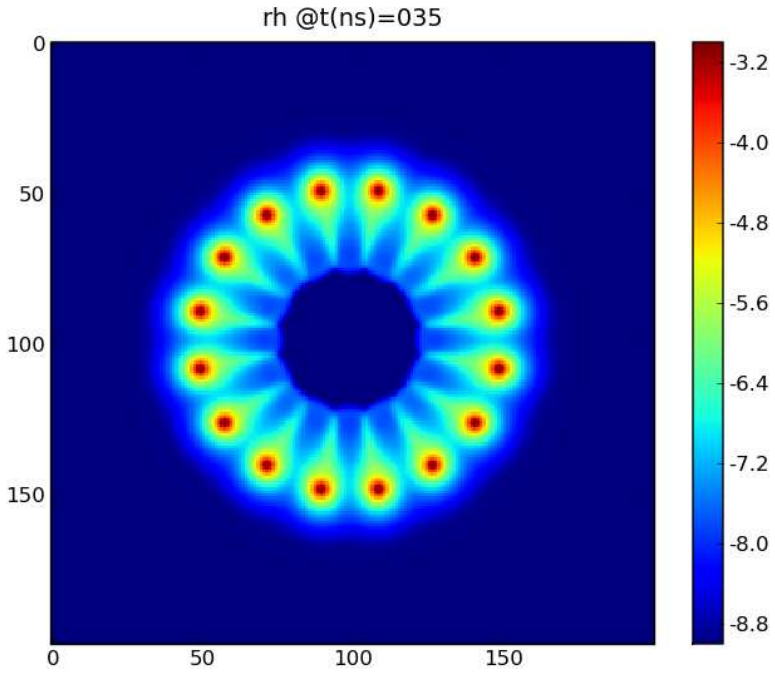


Figure 7.1: Log10 plot of the dimensionless number density at 35 ns into current rise for 8 wire, 9 mm array diameter, 10 micron wire diameter, aluminum array with reference number density of $6x10^{22}cm^{-3}$.

wires are spaced evenly around a 9 mm diameter circle centered in the domain. The initial temperature is set to a constant 1 eV across the domain. The background plasma is initialized to a number density $10^{12}\,cm^{-3}$. This value is determined by successively lowering the background density until the electron inertial length is large enough to constrain current to flow in the wires. This transition is found to occur at number densities around $10^{13}\,cm^{-3}$ to $10^{12}\,cm^{-3}$. All other variables are set to zero in the initial conditions. At time t=0, a sine squared current source with peak output of 1 MA is turned on and applied as a magnetic field boundary condition as discussed in Chapter 3. We now present the results of the simulation using the generalized Ohm's law model at 35 ns

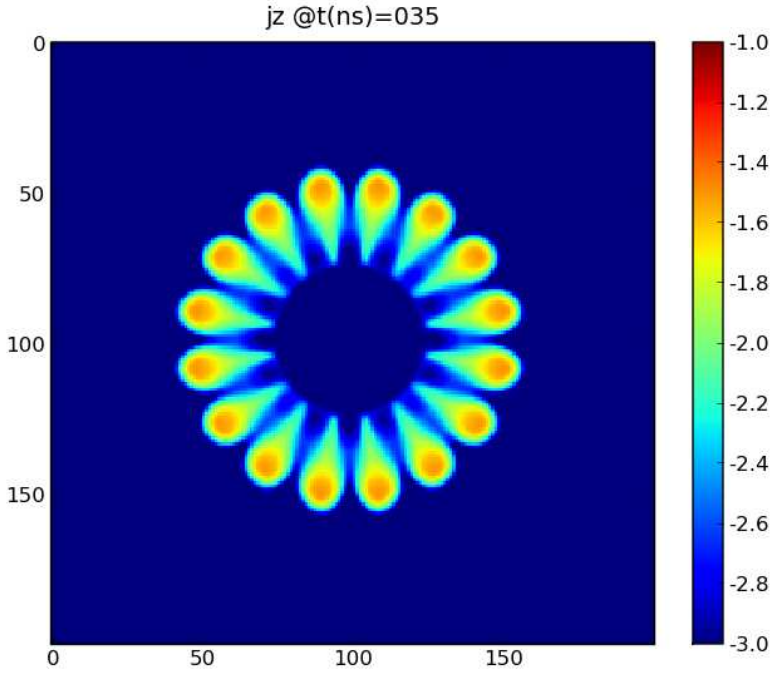


Figure 7.2: Log10 plot of the dimensionless current density at 35 ns into current rise for 8 wire, 9 mm array diameter, 10 micron wire diameter, aluminum array with reference current density of $4.6\text{x}10^{11}\text{Am}^{-2}$.

into the simulation. For all of the two-dimensional simulation results in this thesis, the grid number is explicitly shown in in the figures with the magnitude of the scalar field indicated through a color map. The dimensional system length is described in the introduction to each experiment simulated. We note that since the initiation phase is not modeled, that a time differential of 12 ns to 15 ns is present when compared with experiment.

In Figure 7.1 we see a log plot of the dimensionless number density at 35 ns into the simulation. The reference value is solid density aluminum ($6\text{x}10^{22}\,\text{cm}^{-3}$). The coronal plasma has expanded away from the wire cores and formed a front propagating toward the geometric axis. The coronal plasma ab-

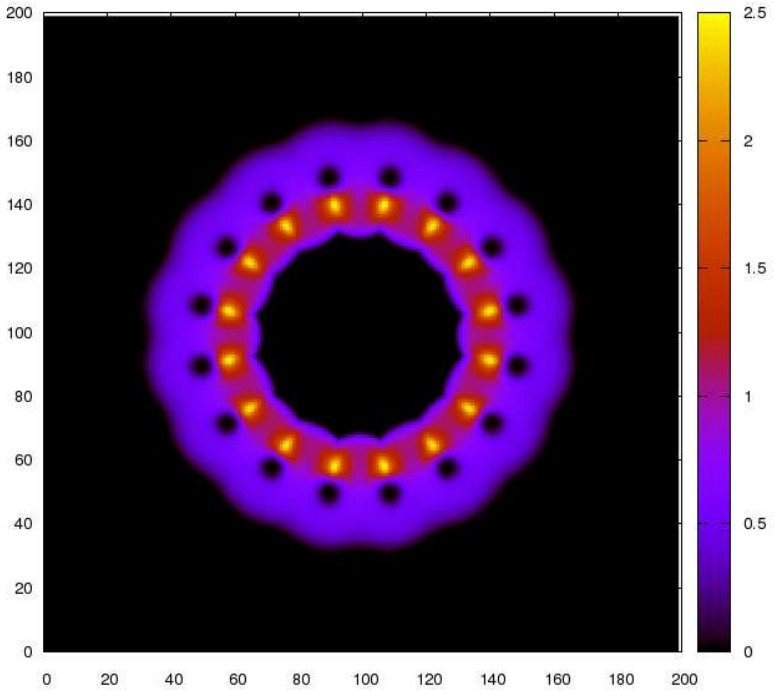


Figure 7.3: Plot of the dimensionless temperature at 35 ns into current rise for 8 wire, 9 mm array diameter, 10 micron wire diameter, aluminum array with reference temperature of 14 eV.

lates in a focused and collimated manner, indicative of a current carrying sheet extending from the core to the geometric axis as in the resistive MHD model of Chapter 5. When the system is evolved further in time, the wire cores run out of mass and the array implodes in accordance with the 0D timing. This 0D timing corresponds to the trajectory of an ideal, infinitely thin shell which does not ablate while imploding due to the compressive magnetic forces. In Figure 7.2, we see the current density distribution for the array with reference value of $4.6 \times 10^{11}$ A m$^{-2}$. Current is flowing throughout the core and coronal plasma regions and on the inside of the wire array. As time evolves, a current carrying precursor column forms. Figure 7.3 shows the existence of a hot coronal plasma that has evolved from the initially cold state. The reference temperature value

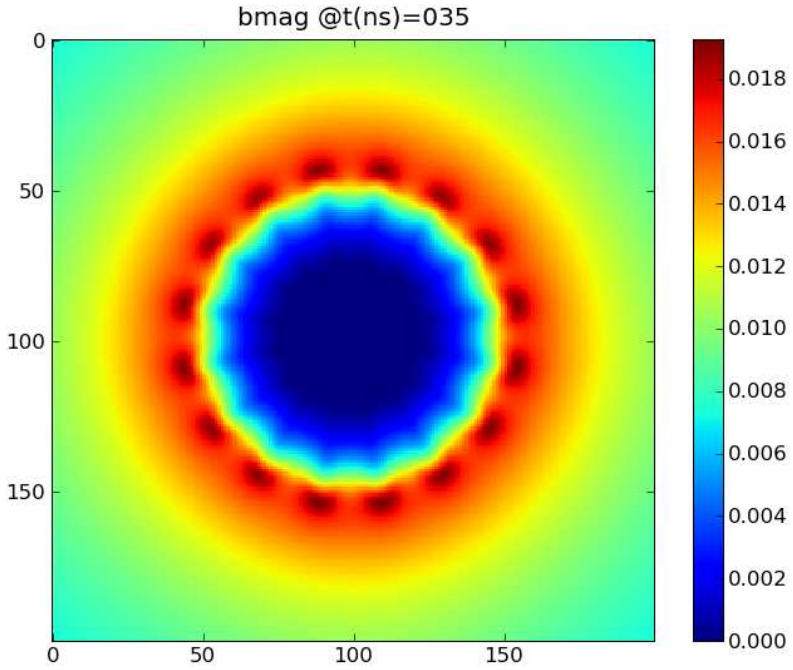


Figure 7.4: Dimensionless magnetic field magnitude at 35 ns into current rise for 8 wire, 9 mm array diameter, 10 micron wire diameter, aluminum array with reference magnetic field of 582 Tesla.

is 14 eV. All of the qualitative features that are expected of a wire array under this symmetry are present, even though the resistivity is held constant throughout the domain. This indicates that the manner in which current organizes itself within the wire array plasma and, thus, the overall dynamical evolution of the system is dependent upon the two-fluid model and, more specifically, finite electron mass.

We now look at the electromagnetic variables that result from our finite volume solution of Maxwell's equations. In Figure 7.4 we see the magnitude of the magnetic field which has a reference value of 582 Tesla. If we examine the divergence of the magnetic field in Figure 7.6 we see that its magnitude is of

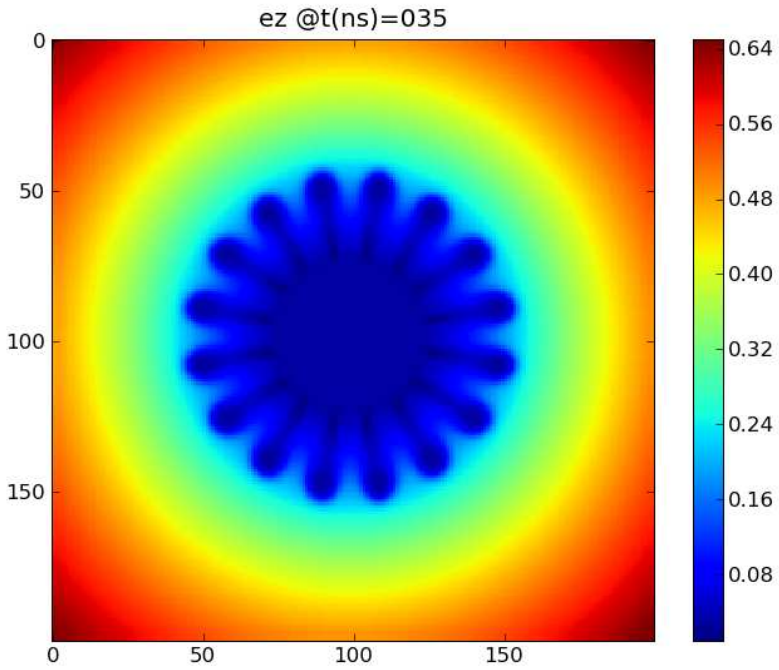


Figure 7.5: Dimensionless electric field at 35 ns into current rise for 8 wire, 9 mm array diameter, 10 micron wire diameter, aluminum array with reference electric field of $5.82 \text{x} 10^{6} \text{Vm}^{-1}$.

order $10^{-15}$ and that our constrained transport update for the magnetic field is working. Figure 7.5 gives the electric field in the array and has a reference value of $5.8 \text{x} 10^{6} \text{Vm}^{-1}$. The time evolution of the system is examined in more detail through synthetic x-ray streaks in the following section.

## 7.2 Time Evolution of the Wire Array

The time evolution of the wire array simulations are presented in this section using a simple synthetic x-ray streak diagnostic. Over each times step, the Rosseland mean opacity of aluminum plasma[69] is tabulated for each cell, which

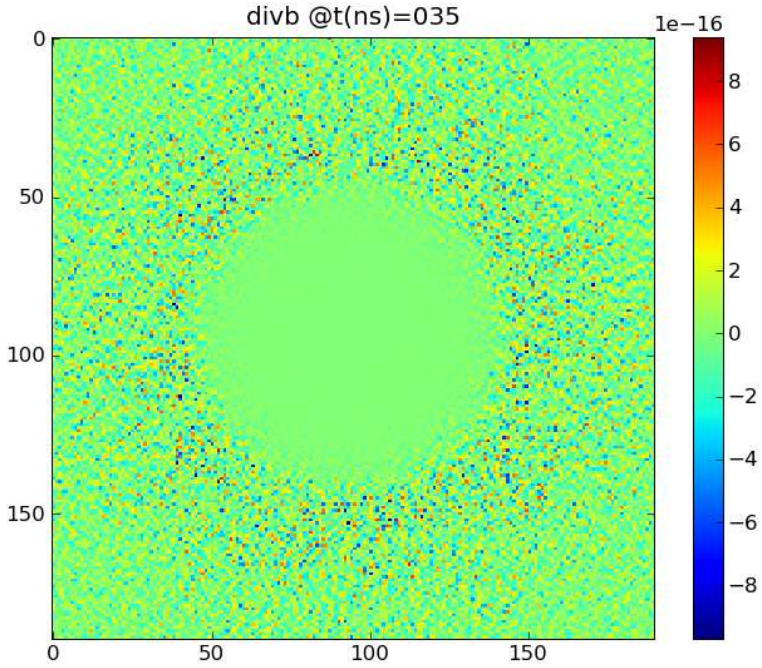


Figure 7.6: Magnitude of the divergence of the magnetic field at 35 ns into current rise for 8 wire, 9 mm array diameter, 10 micron wire diameter, aluminum array.

provides the average opacity over all wave-lengths assuming black body emission. Each cell is considered to be a black body emitter, and the resultant intensity is integrated through the spatially averaged opacity and tallied as a line-out versus time. Since the generalized Ohm's law code does not contain radiative loss, the intensities are overestimated and we stress the simplicity of this model. Our main goal is to look at the time at which the precursor plasma forms on axis and the overall trajectory of the wire array. We simulate three separate arrays from [70] and compare the precursor formation time to that of the experimental visible streak data.

Figure 7.7 shows the streak data for a 16 wire, 9 mm aluminum wire array

on COBRA. The precursor plasma is first visible around 45 ns. The overall trajectory that the wire array takes 0D like. From this streak data we can conclude that the generalized Ohm's law model describes the formation of a radiating precursor plasma and the array implosion phase. When we compare to the experimental value of the precursor formation time found in [70], we see that the timing is off by approximately 15 ns. As previously mentioned, the initial conditions of the simulation assume that voltage collapse has already occurred and at t=0 the wires are already plasma columns. If we take in to account the delay associated with voltage collapse, the precursor timing is in agreement within ±3 ns.

The next array considered is a 16 wire, 4 mm diameter aluminum wire array with 12 micron wire diameter. Again, the implosion trajectory is 0D like and we do not see the delay associated with the rocket model trajectory. The radiating precursor plasma forms within a few nanoseconds of the experimental time, keeping the same time shift when voltage collapse is taken in to account. These results shown in Figure 7.8 indicate that the code predicts the correct precursor timing even when the array diameter is halved. The final wire array considered is a 32 wire, 8 mm diameter aluminum array. Figure 7.9 shows the synthetic streak results for this array. They are consistent with the previous two arrays in the fact that the precursor timing is close to the experimental value but that the array follows a 0D trajectory. The main conclusions of this section are that the generalized Ohm's law model with constant resistivity and no thermal conduction or radiative loss is sufficient to model the formation of coronal plasma and predict the timing of the arrival of precursor plasma to the geometric axis. The implosion trajectories found from this model are different from the delayed implosion path of the rocket model. The differences may be due to the neglect

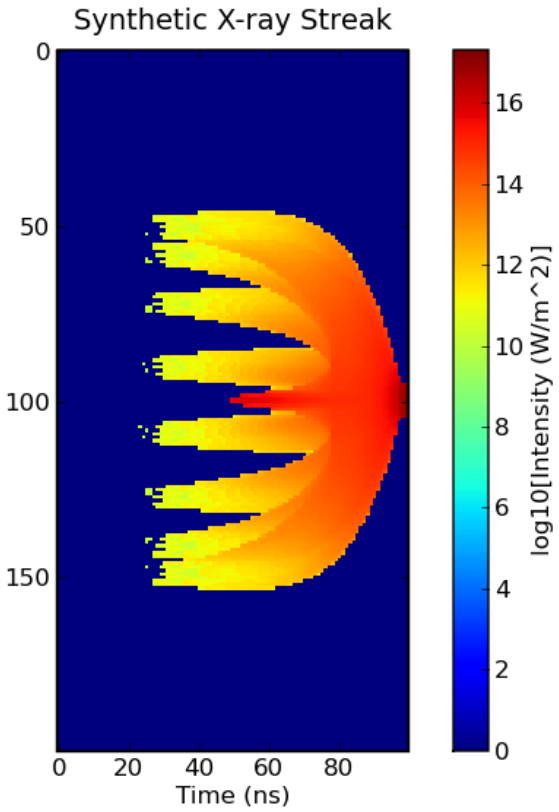


Figure 7.7: Log10 plot of synthetic X-ray streak for 16, 10 micron wires, in a 9 mm diameter array with floor density set to $6x10^{13}cm^{-3}$ and collisionless current confinement.

of radiative transfer. In [15] it is argued that the mass ablation rate of a wire is due to the transfer of energy from the hot coronal plasma to the relatively cold core through radiative means. Let us now explore the mass ablation rate of a wire core in the array and compare to the GORGON code mass ablation rate.

For the following analysis we consider the time evolution of the line density in a core cell which initially contains the entire mass of the wire. Our goal is to understand if the generalized Ohm's law model is sufficient to describe the ablation of mass from the wire into the coronal region. Under the resistive MHD model, the mass ablation rate is much too high and the implosion trajectories

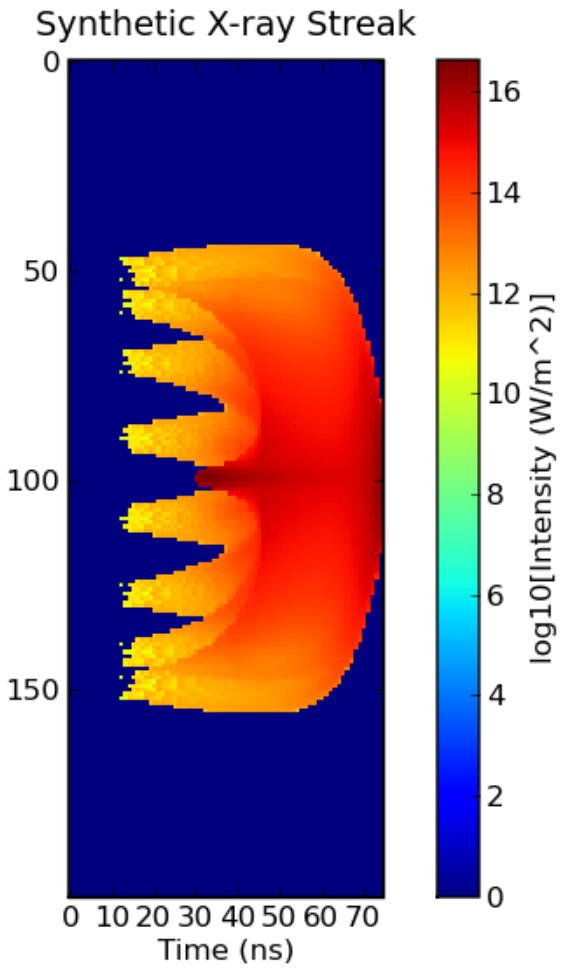


Figure 7.8: Log10 plot of synthetic X-ray streak for 16, 12 microns wires, in a 4 mm diameter array with floor density set to $6x10^{13}cm^{-3}$ and collisionless current confinement.

tend to the 0D solution instead of the delayed rocket model trajectories. The 1D slab results suggest that the electron inertia limited flow results in a different current density distribution through the wire and thus different Joule heating rate. In Figure 7.10 we plot the wire core line density versus time for a 16 wire 9 mm diameter array. The 18 mm domain is subdivided equally in the x and y dimensions and for increasing resolution. These figures show that the generalized Ohm's law model is insufficient to explain the mass ablation rate given

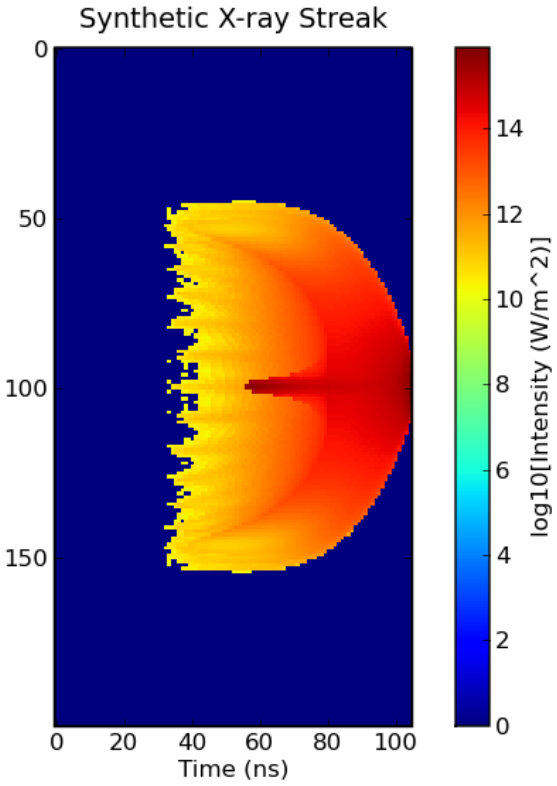


Figure 7.9: Log10 plot of synthetic X-ray streak for 32, 10 micron wires, in a 8 mm diameter array with floor density set to $6x10^{13}cm^{-3}$ and collisionless current confinement.

by the rocket model (the GORGON result), under the approximation that the resistivity is constant within the domain and radiative transfer does not occur.

In Figure 7.11 we change the adiabatic index to decrease the Joule heating rate of the core in an attempt to delay the ablation. For any reasonable value the adiabatic index would take, the core loses mass faster than the reference GORGON solution.

These results make sense in light of the fact that the under any model that does not consider thermal conduction or radiative transfer, Joule heating is the only energy input to the wire core. Thus the core can only expand at its local

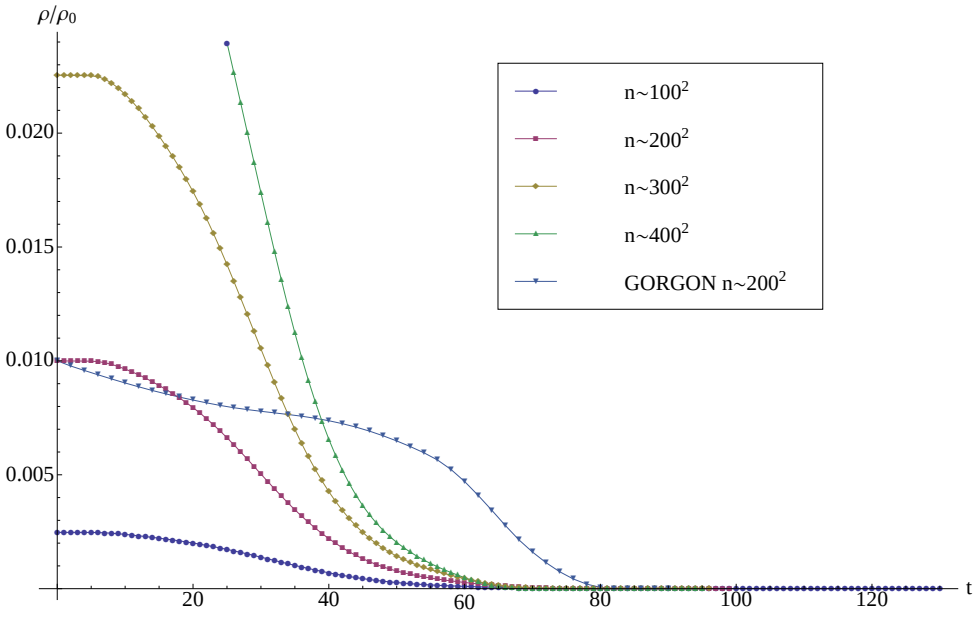


Figure 7.10: Core line density fraction versus time for 16 wire, 9 mm diameter array. The mass over time is shown for n points on a uniform 18 mm x 18 mm grid under generalized Ohm's law model without thermal conduction, radiation losses, or variable resistivity. Calculated mass over time from GORGON code is provided as a reference.

sound speed as determined by the Joule heating input. The overall conclusion is that to correctly model the mass ablation rate of the array under the two-fluid or resistive MHD systems, will require either a thermal conduction or radiative transfer model which is beyond the scope of this thesis.

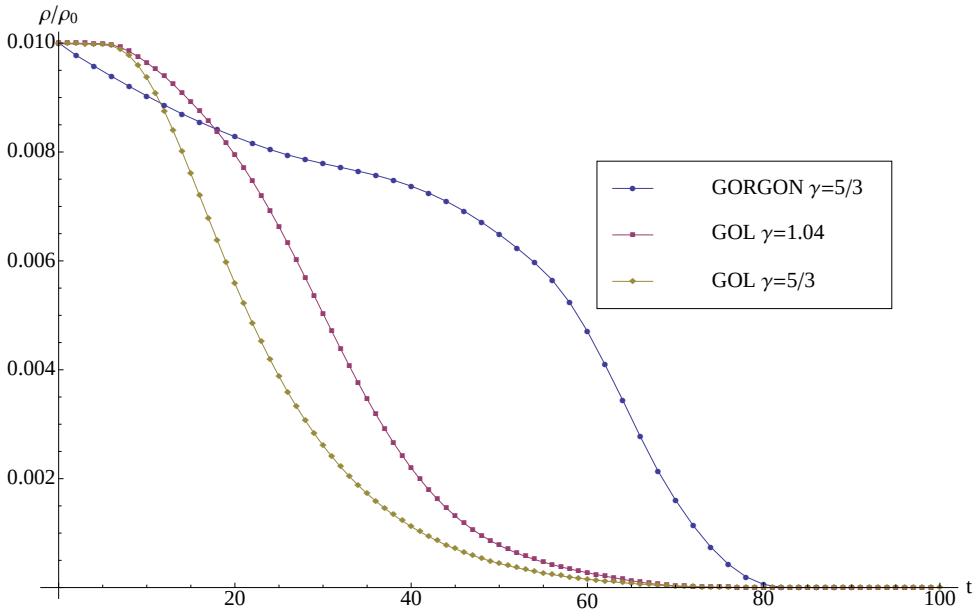


Figure 7.11: Core line density fraction versus time for 16 wire, 9 mm diameter array. The mass over time is shown for 200x200 points on a uniform 18 mm x 18 mm grid under generalized Ohm's law model without thermal conduction, radiation losses, or variable resistivity. Adiabatic index is held constant for each simulation.

## 7.3 Two-Fluid Effects

The introduction of the Hall term to the wire array model couples the out of plane magnetic field and velocity with the evolution of the in plane magnetic field and velocity. The converse is true for the electric field and current densities. The x-y plane simulations under the generalized Ohm's law model will include field components neglected by the resistive MHD model. The first of these fields we discuss, is the radial electric field. The radial electric field is shown in Figure 7.12 at 22 ns into the simulation. Early on, the radial electric

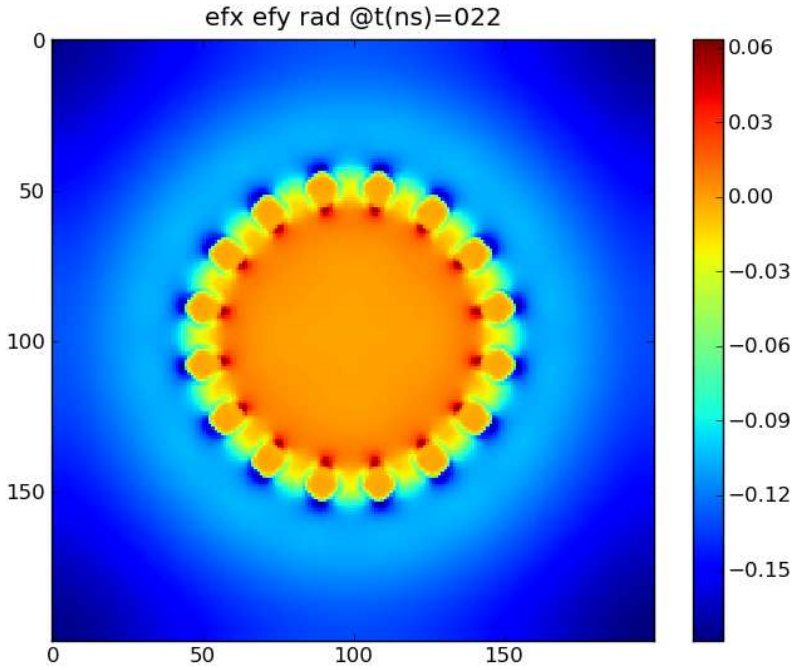


Figure 7.12: Plot of dimensionless radial electric field at 22 ns for the generalized Ohm's law model. The wire array is 9 mm in diameter with 16, 10 micron aluminum wires.

field magnitude can be as much as 25 percent of the z directed driver electric field. This constitutes a significant force, that is not negligible, which the MHD approximation removes from the system. The radial electric field is positive on the inside of the array and negative on the outside of the array. This indicates that the radial current flows toward the wires. We will show in the next chapter that the radial electric field contribution, when the 2D axial slab geometry is considered, leads to a natural anode-cathode asymmetry in the system. Under the infinite wire approximation, the effects of this asymmetry on the plasma dynamics is limited and the precursor timing and implosion trajectory are similar to those when the ion inertial length is taken to be zero. In Figure 7.13 we see the axial velocity driven by inclusion of the Hall term. A result of the radial electric

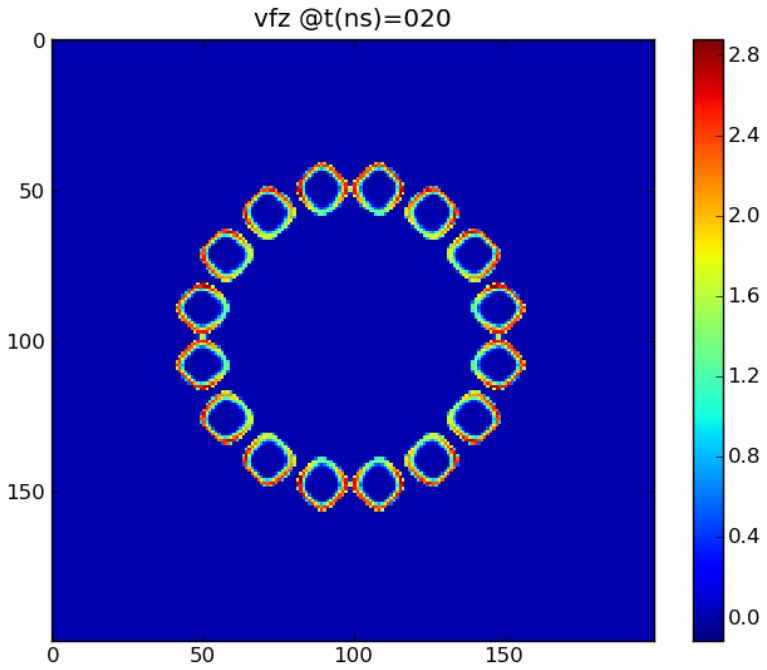


Figure 7.13: Plot of dimensionless out of plane Z velocity for the generalized Ohm's law model at 20 ns. The wire array is 9 mm in diameter with 16, 10 micron aluminum wires.

field is to drive strong axial flows in the low density regions where the ion inertial length is of order 1 mm. The flows are directed from anode to cathode with velocity in the range of 30km $s^{-1}$ to 40km $s^{-1}$. This Hall driven flow breaks the symmetry of MHD and makes the results dependent upon the location of the anode and cathode.

Figure 7.14 shows the axial flow at 60 ns. Its magnitude has saturated and is not much beyond the axial velocity at 20 ns. The formation of the precursor shows that it has a strong axial velocity towards the cathode. As the system evolves, the final pinch column is also subject to Hall driven flows toward the cathode.

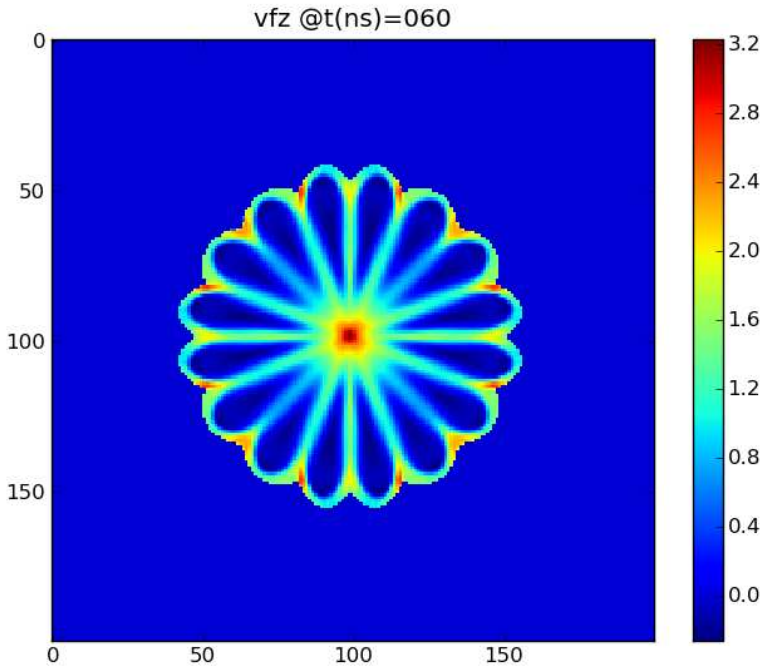


Figure 7.14: Plot of dimensionless out of plane z velocity for the generalized Ohm's law model at 60 ns. The wire array is 9 mm in diameter with 16, 10 micron aluminum wires.

Figures 7.12 through 7.14 show that important physics is lost when the Hall term is neglected from the simulation. Specifically, MHD has an anode cathode symmetry that does not exist in the more physically correct Hall MHD model. The results of the asymmetry will be apparent when we rotate the axis to simulate an imploding plasma slab subject to MRT instability.

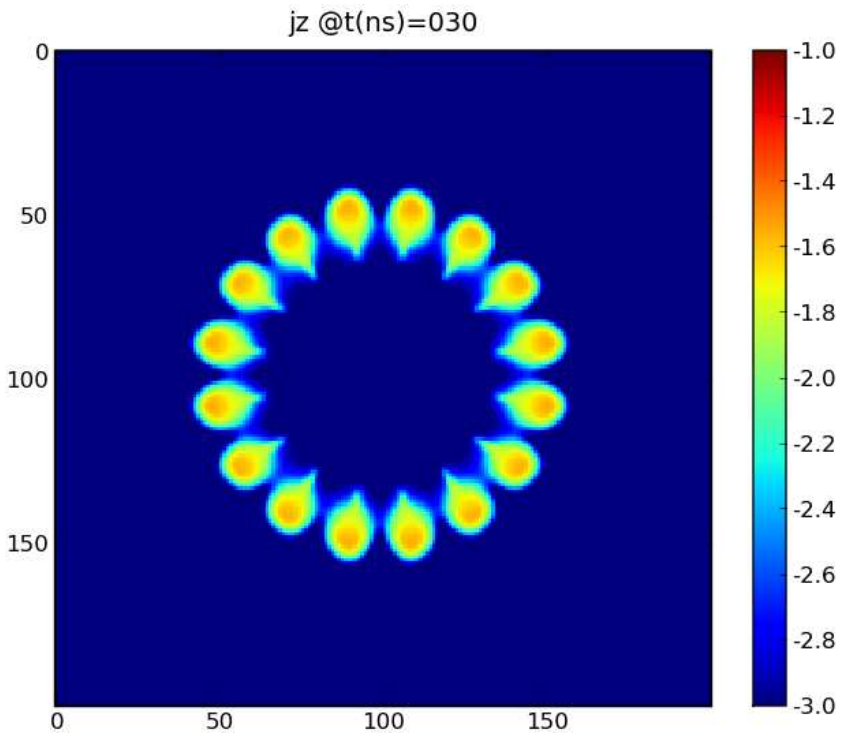


Figure 7.15: Log10 plot of the dimensionless current density at 30 ns with collisionless confinement of current via electron inertia. The initial conditions used a floor density of five orders of magnitude off of solid with a 16 wire, 9 mm array disaster, 10 micron wire diameter, aluminum array with reference current density of $4.6\text{x}10^{11}\text{Am}^{-2}$.

## 7.4 Electron Inertial Current Confinement Comparison with Vacuum Resistivity

We now compare our 2D generalized Ohm's law simulations of wire arrays to the resistive MHD model. In Figure 7.15 the current density is plotted for a 16 wire, 9 mm diameter aluminum wire array with 10 micron wires. The image is from 30 ns into the simulation when the coronal plasma is initially forming the current sheet. We use this as a reference solution for comparing to the resistive MHD model.

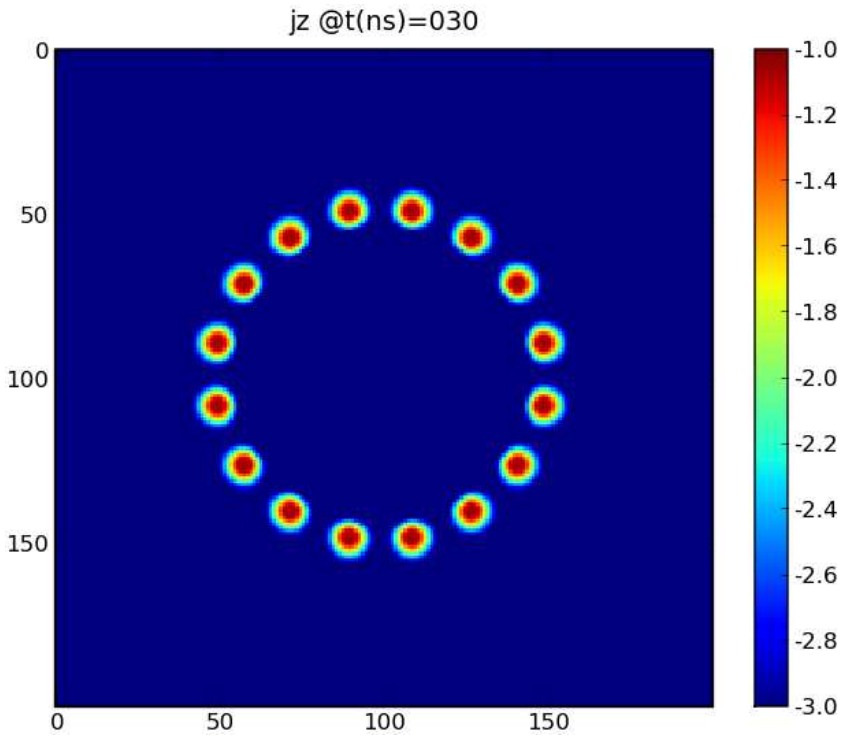


Figure 7.16: Log10 plot of the dimensionless current density at 30 ns where a vacuum resistivity with inverse dependence on number density is used to confine current. Joule heating is cutoff below ten times the floor density of nine orders of magnitude off of solid density. The initial conditions are for a 16 wire, 9 mm array diameter, 10 micron wire diameter, aluminum array with reference current density of $4.6 \times 10^{11} \mathrm{Am}^{-2}$.

The resistive MHD solution to the wire array problem shown in Figure 7.16 has the same initial conditions and density range as the generalized Ohm's law simulation. The only difference is in the application of a vacuum resistivity with inverse dependence on number density to confine current to the wires. The current density profile that results, is much more confined to the wire core, with a peak current density three times the reference solution. The large (nine orders of magnitude) density range along with the resistive MHD model gives unreasonable heating at the plasma-vacuum interface. Temperatures of $10^3$ eV are calculated. The only way to recover a physically reasonable result is to ap-

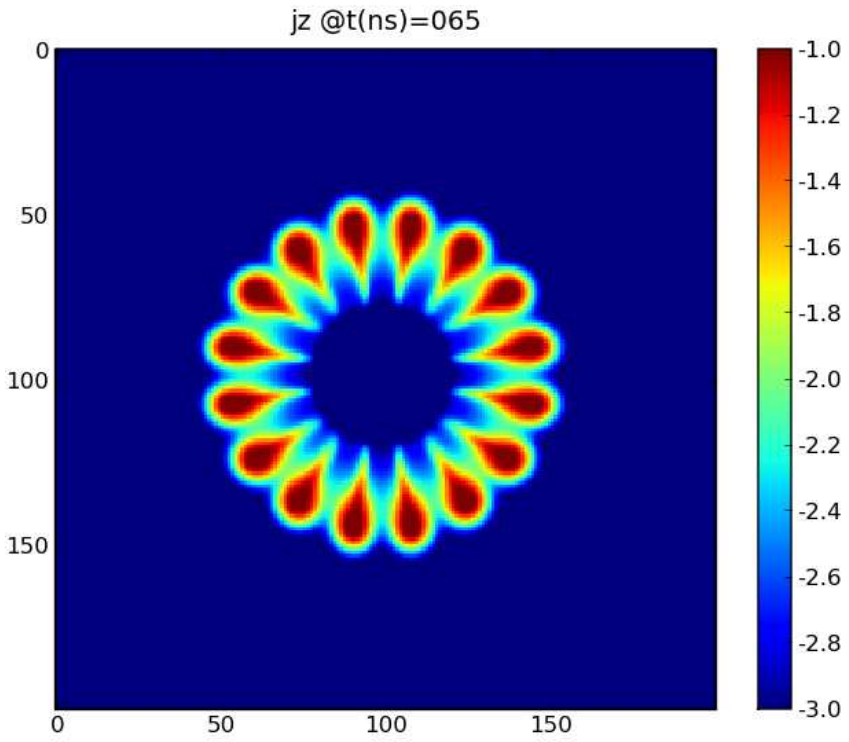


Figure 7.17: Log10 plot of the dimensionless current density at 30 ns where a vacuum resistivity with inverse dependence on number density is used to confine current. The initial conditions used a floor density of nine orders of magnitude off of solid with an 16 wire, 9 mm array diameter, 10 micron wire diameter, aluminum array with reference current density of $4.6\text{x}10^{11}\text{Am}^{-2}$.

ply a cutoff to the Joule heating or to increase the density floor to five orders of magnitude from solid density. In Figure 7.17, the current density profile is shown for the resistive MHD model with the same initial conditions as Figure 7.16, but with Joule heating turned off at number densities below the dimensionless cutoff floor value of $10^{-8}$. Again, we see the effect of applying cutoff values to make the resistive MHD model give reasonable answers. The result is to change the current density distribution drastically. This is the same conclusion derived from the 1D slab problem, where resistive MHD, either with the assumed steady state solution, or a vacuum resistivity with inverse num-

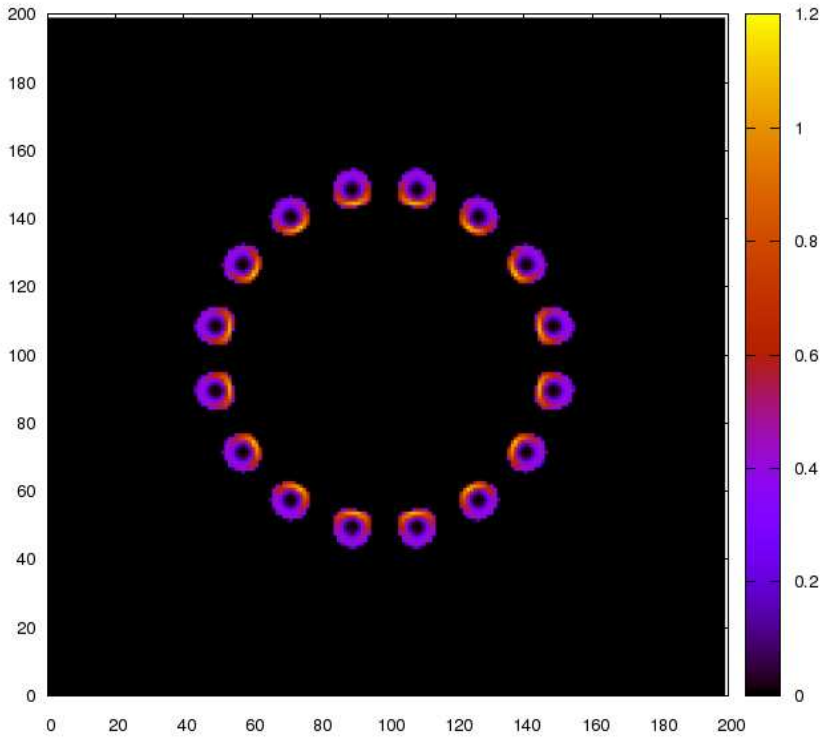


Figure 7.18: Plot of the dimensionless temperature at 30 ns where a vacuum resistivity with inverse dependence on number density is used to confine current. The initial conditions used a floor density of five orders of magnitude off of solid with an 16 wire, 9 mm array diameter, 10 micron wire diameter, aluminum array with reference temperature of 14 eV.

ber dependence, does not provide a unique physical answer. In Figure 7.18, the temperature profile is shown for the resistive MHD model when the floor cutoff is increased. The magnitude of the temperature is more in line with the electron inertia model, however the hot coronal plasma is more tightly confined to the core region. These results show that for the two-dimensional wire array simulations, the only self-consistent treatment of the plasma-vacuum interface is provided by the generalized Ohm's law model through its inclusion of finite-electron mass.

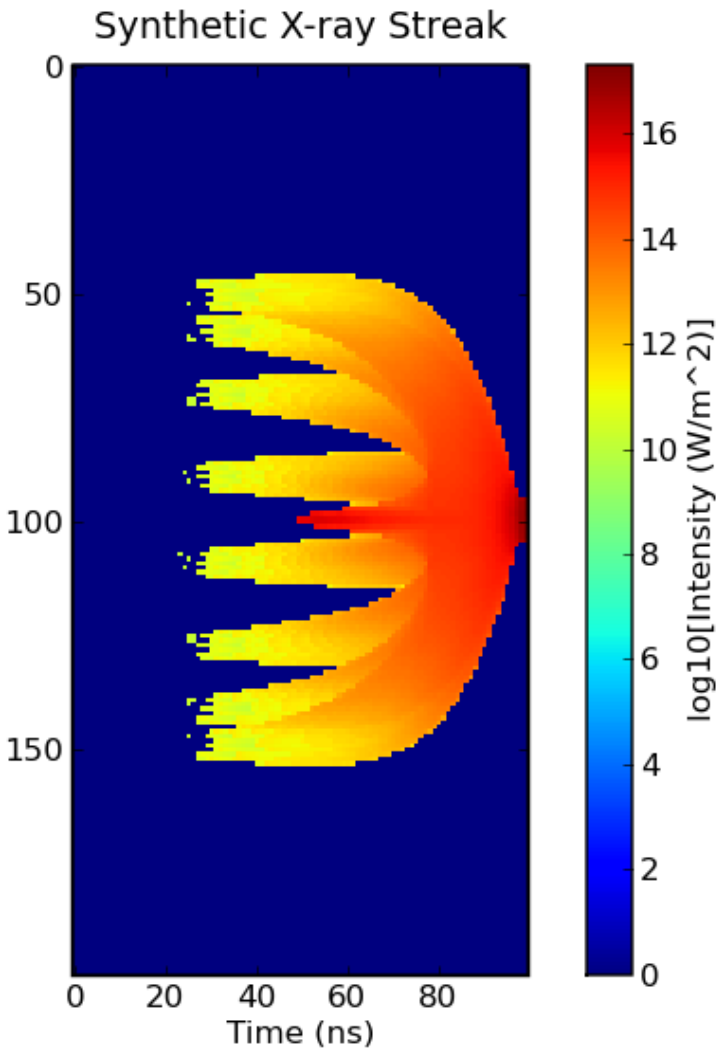


Figure 7.19: Log10 plot of synthetic X-ray streak for 16 wire, 9 mm diameter array with floor density set to $6x10^{13}cm^{-3}$ and collisionless confinement of current to wires.

We now compare the time evolution of the wire array problem between the different resistive MHD vacuum resistivity models and the generalized Ohm's law solution. Figure 7.19 shows the precursor formation and array trajectory for the previously discussed array. The streak result is consistent within the generalized Ohm's law model for different floor densities, as long as the electron inertial length is resolved by the grid at the floor number density. However,

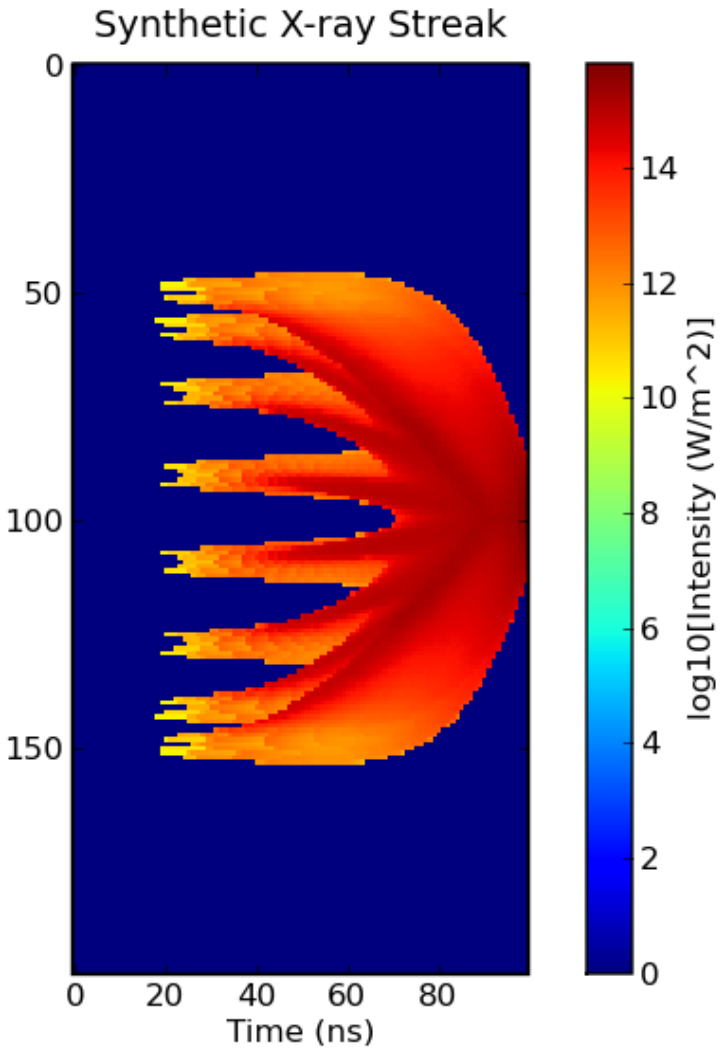


Figure 7.20: Log10 plot of synthetic X-ray streak for 16 wire, 9 mm diameter array with floor density set to $6x10^{16}cm^{-3}$ and vacuum resistivity with inverse number density dependence confining current to wires.

when we compare the results of resistive MHD by changing the floor density, we see that the overall dynamics greatly change. The resistive MHD solution is shown in Figure 7.20 where the density range in the simulation is the same as the generalized Ohm's law solution. For the resistive MHD case, the formation of a radiating precursor plasma is delayed until just before the implosion,

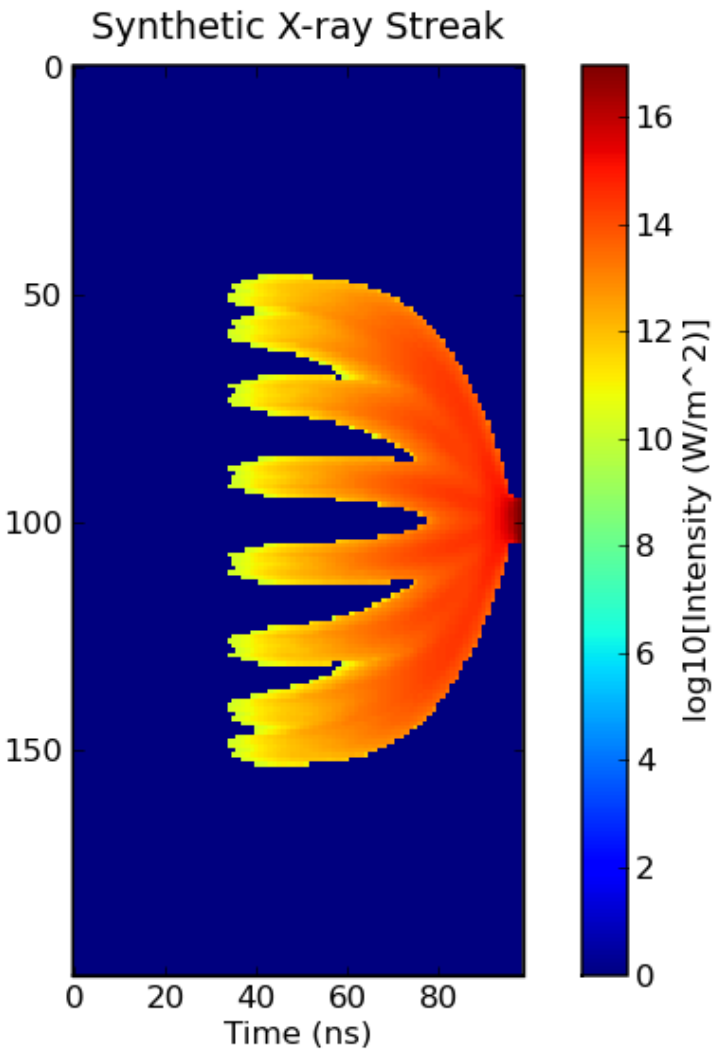


Figure 7.21: Log10 plot of synthetic X-ray streak for 16 wire, 9mm diameter array with floor density set to $6x10^{13}cm^{-3}$ and vacuum resistivity with inverse number density dependence confining current to wires.

in disagreement with the experimental results. By decreasing the density range to five orders of magnitude, the results of which are shown in Figure 7.21, both the implosion trajectory and precursor timing are changed. Again the resistive MHD model is dependent upon both the form of the anomalous numerical resistivity and the cutoff floor density.

CHAPTER 8

# THE HALL EFFECT IN ABLATING PLASMAS

In this chapter, we explore the evolution of the generalized Ohm's law system under two-dimensional slab geometry, using the assumption of an infinite z-axis. The orientation for the following plots has the axially resolved y-axis extend from left to right in the figures. The radial variation of the slab is from top to bottom. This geometry differs from the wire array simulations of the previous section in that we resolve the axial dimension, allowing for the development of Magneto-Rayleigh-Taylor (MRT) instability. In addition to the slab implosion problem, we simulate the slab version of the radial foil experiment. Our goal is to see if the typical jet and bubble structures form without the inclusion of radially converging current density. Experimentally fielded conical and radial wire/foil loads [71, 72] always include this radial convergence. The implosion of a thin shell and the expansion of a plasma bubble from foil both involve the evolution of a plasma with a large amount of surface area expanding into a vacuum. Thus, from our experience with previous simulations in this thesis, we expect that to properly model these experiments will require physics beyond the resistive MHD model.

## 8.1 Simulation of 2D Plasma Slab

We first consider the implosion of two infinite aluminum plasma slabs separated 16 mm from each other. The sine squared current source is applied as a $B_z$ boundary condition along the left edge of the figure. The driver has an assumed peak output of 1 MA. The initial condition for the number density is a

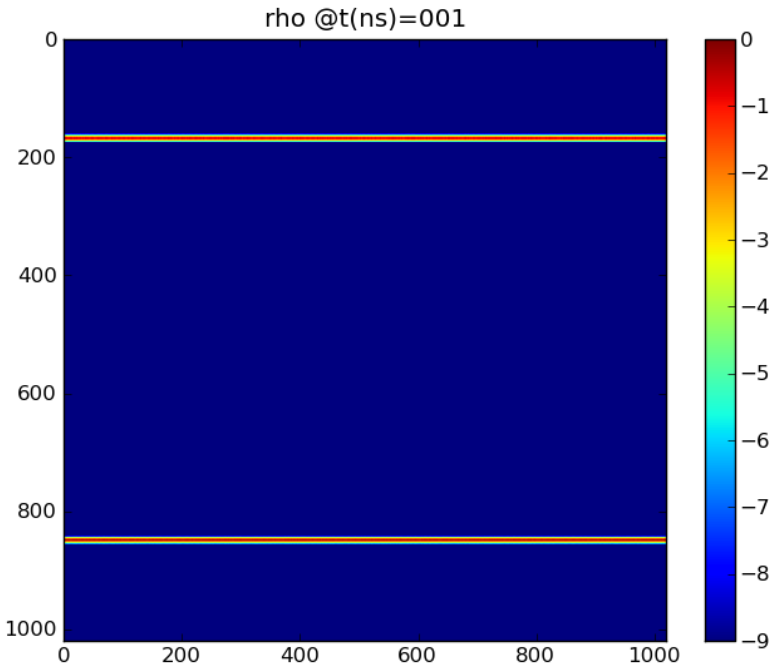


Figure 8.1: Log10 plot of the initial condition for the number density in the two dimensional plasma slab implosion simulation.

line of cells 24 mm high. A density perturbation of one percent is applied to the slab to seed MRT growth. This initial condition for the system is seen in Figure 8.1. The plasma has an initial temperature of 1 eV and all other field variables are initially zeroed out. The background number density is set to $10^{12}\text{cm}^{-3}$ and a Spitzer resistivity is applied to the system. Figure 8.2 shows the log of the number density 28 ns into the current pulse. The coordinate system is such that the anode is the left plane of the figure and the cathode is the right plane of the figure. For the slab geometry, the formation of precursor plasma flow occurs as soon as the global field diffuses through the liner. Unlike the wire array case, there is no local field component inside the slab to push against the expanding plasma. The grid resolution is increased to 1000 x 1000 cells for the 24

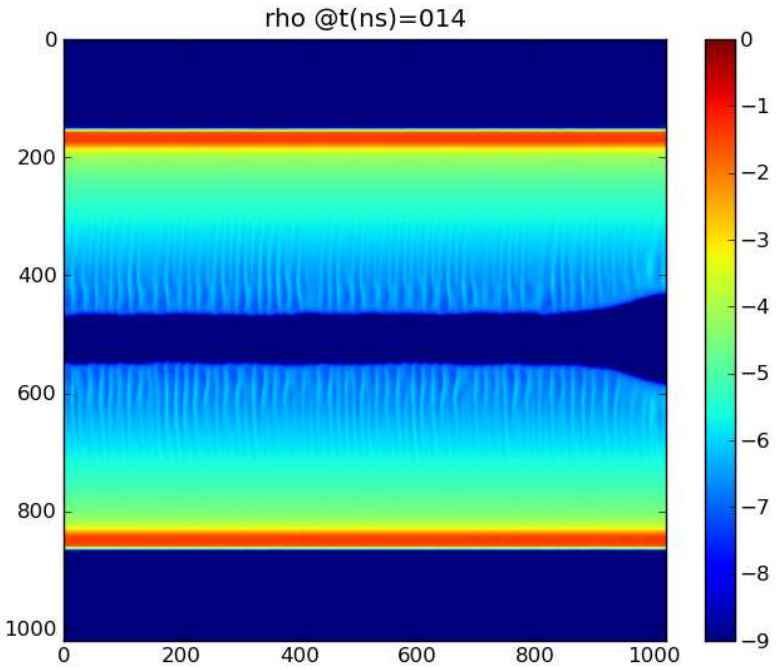


Figure 8.2: Log10 plot of the dimensionless number density for the plasma slab at 28 ns into the simulation. The anode surface is to the left and the cathode surface is to the right. Hall instability occurs in the leading edge of the ablation front for number densities of order $10^{17}\text{cm}^{-3}$.

mm x 24 mm simulation domain due to the existence of two unstable modes in the system. The first instability that appears is at the edge of the precursor flow as seen in Figure 8.2. The modulation in the number density only appears when the Hall term is included in Ohm's law. It grows from the grid scale to its saturation wavelength of 0.5 mm as seen in Figure 8.2. This wavelength is close to the so called fundamental mode [73] for aluminum arrays. It only exists in the precursor flow where the ion inertial length is of order a 1 mm and disappears at number densities above approximately $10^{17}\text{cm}^{-3}$ to $10^{18}\text{cm}^{-3}$. The wavelength is constant in time after saturation and well resolved by the grid.

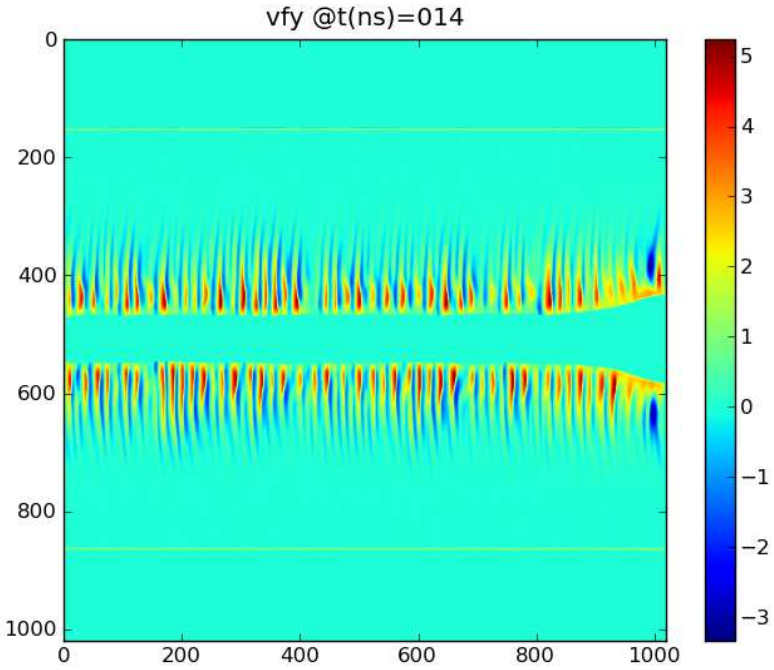


Figure 8.3: The dimensionless y component of the velocity (right facing direction for figure orientation) for the plasma slab at 28 ns into the simulation. The change in sign as a function of y shows the existence of Hall instability that maintains an approximately constant wavelength as the plasma-vacuum interfaces propagates to the geometric axis.

The axial component of velocity is seen in Figure 8.3. The short wavelength sign changes in the axial velocity are indicative of instability which is most likely due to a wave propagating against the precursor flow, resulting in its time constant wavelength. The Hall instability modulation of the density front embeds itself in the pinch column as a short wavelength fluctuation in number density. This is seen in Figure 8.4.

Another important difference between the generalized Ohm's law simulation and the MHD simulation is the presence of anode-cathode asymmetry in

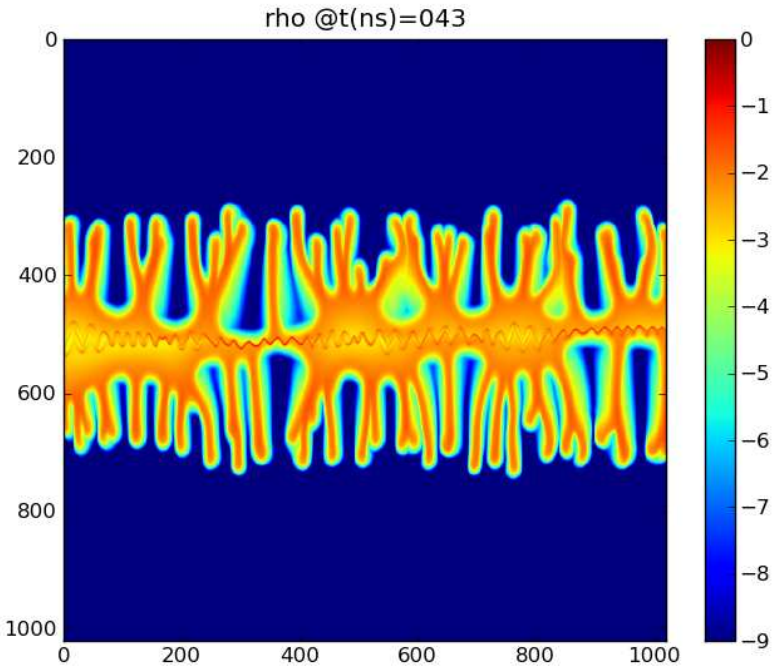


Figure 8.4: Log10 plot of the dimensionless number density for the plasma slab at 86 ns into the simulation. The anode surface is to the left and the cathode surface is to the right. The slab implosion has undergone Magneto-Rayleigh-Taylor instability while the density modulations due to the Hall instability have imprinted a short wavelength modulation on the precursor column.

the flow. Only when the Hall term is included in Ohm's law does the cathode experience a delay in implosion, most likely due to the large axial flow seen in the 2D planar wire array simulations. This axial component of the flow is always towards the cathode and leads to nonuniform precursor flow. Figure 8.4 shows the number density distribution at 86 ns into the simulation. At this point the global MRT instability has formed and the characteristic forking fingers are present. The wavelength of the MRT instability at implosion is comparable to the experimental results from imploding aluminum wire arrays of similar height.

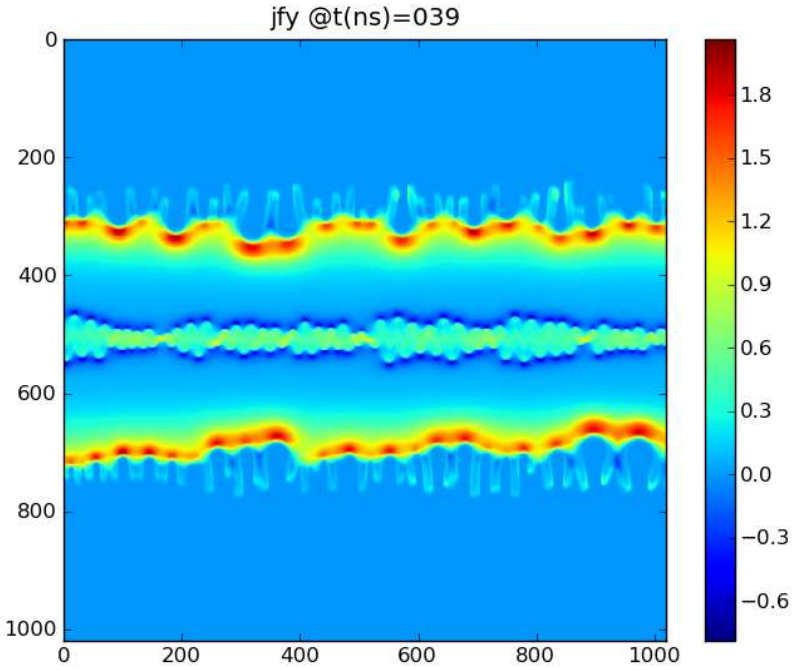


Figure 8.5: The dimensionless y component of the current density ( right facing direction for figure orientation) for the plasma slab at 78 ns into the simulation. Fingers from the forming MRT instability carry a small portion of the current while the majority of current density implodes as a sheet correlated with the highest density regions.

Figures 8.5 and 8.6 show the axial and radial current densities 78 ns into the simulation. A fraction of the current flows around the MRT finger while the majority of the current flows as a sheet near the leading edge of the implosion front. The result of the small wavelength modulation from the Hall instability is seen in current flow through the pinch column. Past this time the column pinches down until kink instability disrupts current flow. The entirety of these simulations were performed without tracking the vacuum interface. The overall effect of the Hall term on the growth of the MRT instability was negligible, due the fronts high density and small ion inertial length. From these results, we

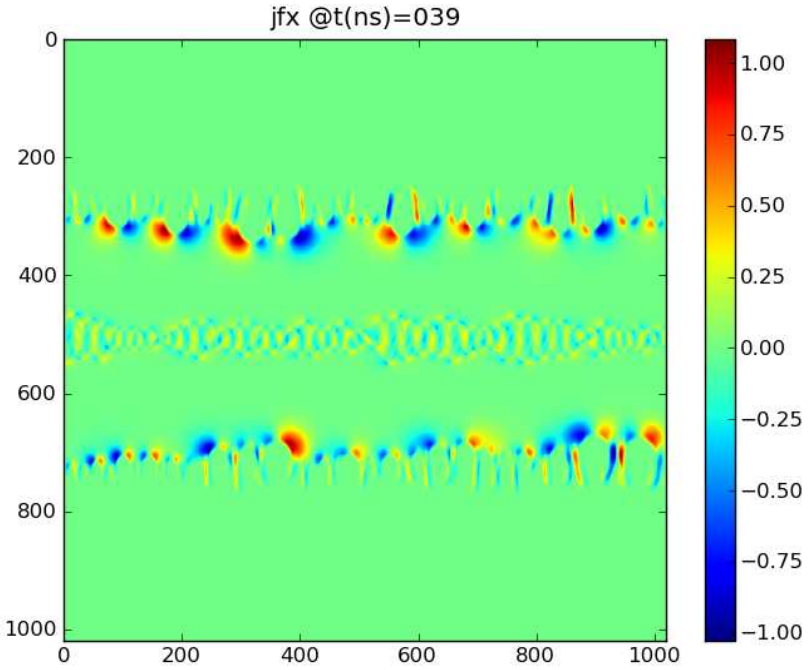


Figure 8.6: The dimensionless x component of the current density ( upward facing direction for figure orientation) for the plasma slab at 78 ns into the simulation. The periodic sign transition of the current density indicates that the current is tracking the path of the plasma-vacuum interface for the MRT instability, while the remnants of the Hall instability are apparent due to the variations in the current path through the geometric axis.

conclude that the Hall term introduces a flow from the anode to the cathode. This results in an asymmetric ablation front which is only due to the Hall radial electric field. Additionally, the Hall term produces a modulation instability for plasma regions where the ion inertial length is of order 1 mm. It is interesting to note that saturation wavelength of the Hall instability is of order the wavelength of the fundamental mode and if we were to assume that it scaled in proportion to the ion inertial length, we would expect that tungsten would generate a Hall instability with wavelength $\lambda_W \approx \lambda_{Al} * \sqrt{m_{Al}/m_W} \approx 1.25mm$. This scales in the

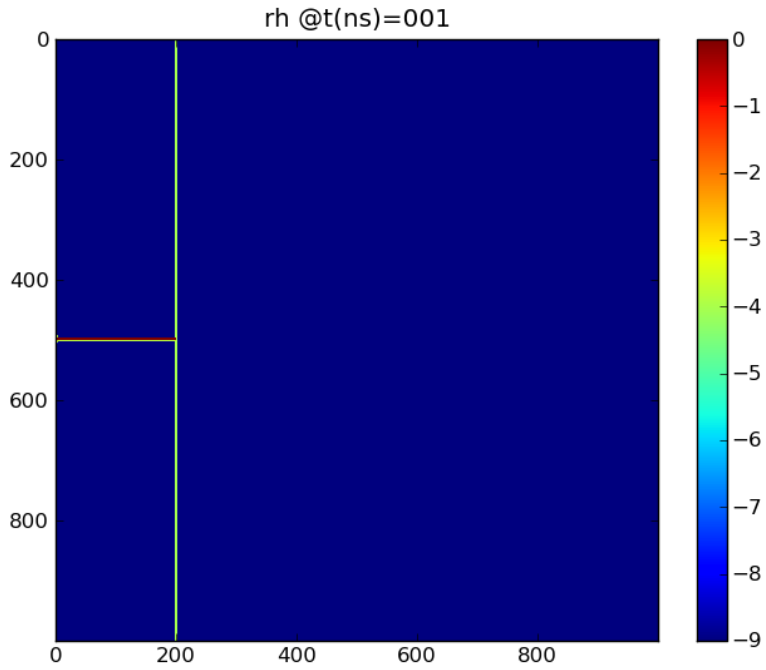


Figure 8.7: Log10 plot of the initial condition for the number density in the two dimensional foil slab problem.

wrong direction for the tungsten fundamental, but the magnitude of the scale factor between Aluminum and Tungsten is right. As the slab implodes, it is subject to MRT instability that limits the pinch convergence on axis. This suggests that experiments on COBRA for cylindrical shells massed to implode in 100 ns will most likely be experience instability during implosion.

## 8.2 Planar Foil Simulation

We now turn our attention to the ablation of a foil surface where the current is returned though a central metal pin. This configuration, along with radial

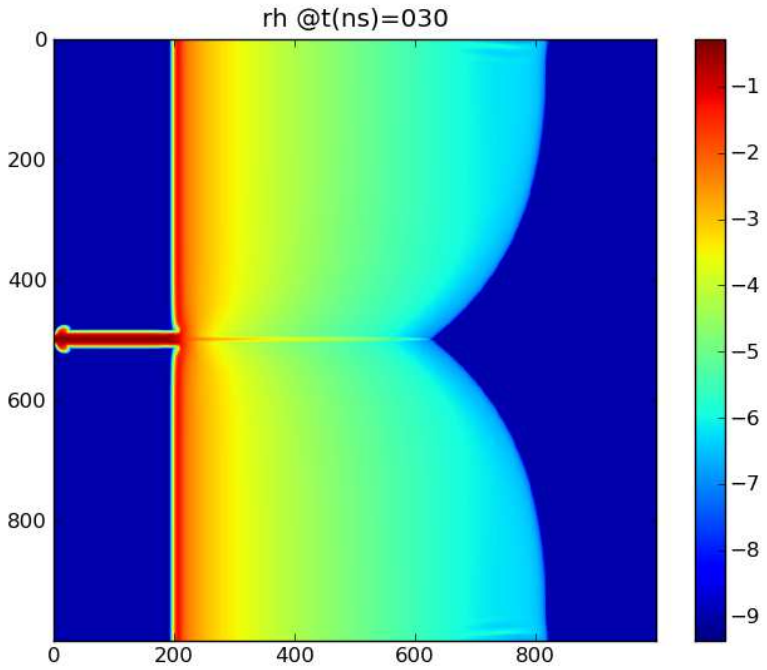


Figure 8.8: Log10 plot of the dimensionless number density for the foil slab at 60 ns into the simulation. The anode surface is connected to the foil while the cathode surface is connected to the central pin. The surface of the plasma has expanded into the vacuum forming a precursor flow for the bubble to form in.

wire arrays [74], has seen interest as a mechanism for producing astrophysical jet like flows and plasma bubbles. Whether by foil or array, these experimental setups typically contain radial convergence of the current flow to a central pin. Since our code is in Cartesian coordinates, we investigate this problem as an infinitely long slab without radial convergence of the current density. For this case, it is not known if the same qualitative structures will exist. The initial density profile is given in Figure 8.7. It consists of a thin slab with a dense plasma cathode. Since there is no numerical interface between the plasma and vacuum, it is trivial to include the pin as a solid density plasma, instead of us-

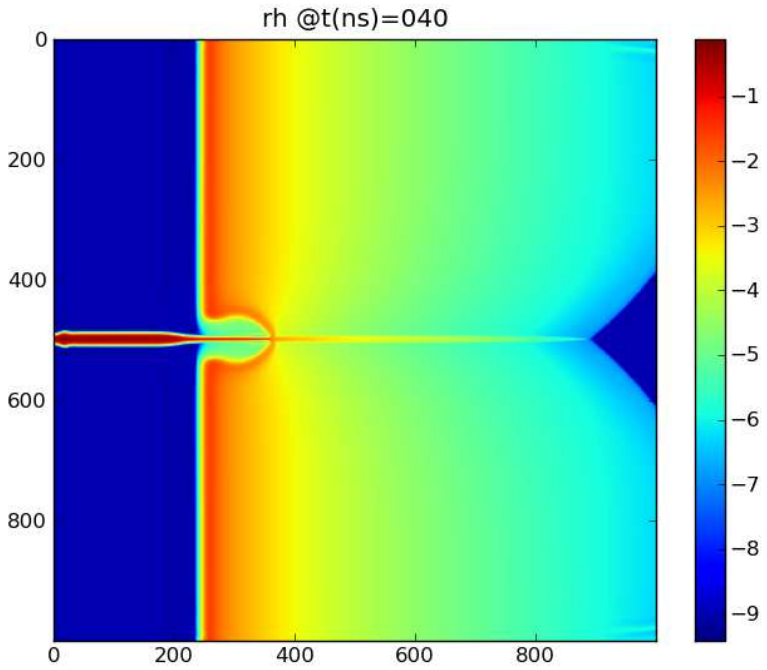


Figure 8.9: Log10 plot of the dimensionless number density for the foil slab at 80 ns into the simulation. A bubble is forming at the cathode pin without the necessity of radial convergence.

ing a more complicated boundary condition. The magnetic $B_z$ component is constant in space and increasing in time with a sign change on either side of the pin. The wall acts as an anode which current flows out, going into the foil and out of the pin. Figure 8.8 shows the number density for the simulation at 60 ns. The surface of the foil has ablated into the vacuum. The ablation is nonuniform due to the jump in magnetic field magnitude at the pin, and as such the surface plasma collides along the central axis dividing the cathode, forming the jet. The current density at this time shows the jet to be relatively unmagnetized, only containing the current density that propagated with the ablation front. This mechanism of forming the jet is different from those described in radially convergent geometries, where it is said to emerge from plasma expanding directly

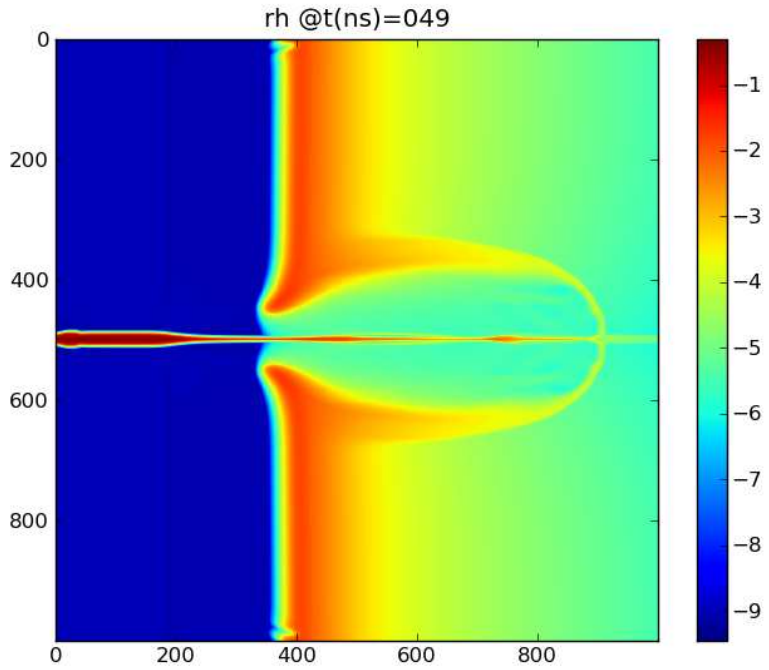


Figure 8.10: Log10 plot of the dimensionless number density for the foil slab at 98 ns into the simulation. The anode surface is connected to the foil while the cathode surface is connected to the central pin. The bubble has expanded into the precursor flow.

foil on top of the pin cathode. Surface plasma has started to ablate from the pin and fill in the anode-cathode gap. In Figure 8.9, the number density is shown at 80 ns. The majority of the simulation domain on the foil side has filled in with ablated plasma. The bubble expands not into vacuum, but a prefill of ionized plasma of about $10^{17}\text{cm}^{-3}$. The formation of a magnetized bubble is somewhat unexpected as only radially convergent geometries have been experimentally fielded to generate magnetic bubbles. Figure 8.2 shows the further evolution of the magnetic bubble as it propagates in the ablative prefill plasma. The return current column is fully formed inside inside the bubble. As time advances, the bubble leaves the system, producing a strong electric field in the density void

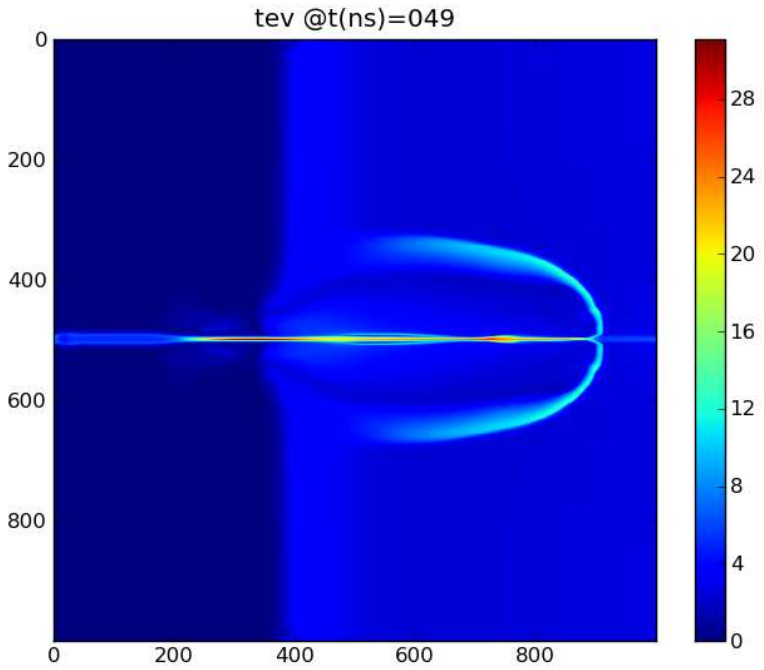


Figure 8.11: Plot of the dimensionless temperature profile for the foil slab at 98 ns into the simulation. The main current paths around the bubble and back through the internal pinch column experience the majority of the Joule heating.

left behind which launches a plasma jet toward the pin.

Figure 8.11 shows the temperature profile of the jet and bubble at 98 ns. The majority of the heating occurs at the bubble surfaces at it moves through the ablated plasma prefill. The return current path inside the bubble is subject to substantial Joule heating. The reason for this is evident when we look at the current density path, as shown by the vector plot of the current density at 98 ns. From Figure 8.12, we see that there are two current paths followed from the anode source to the cathode sink. The current moves along the foil surface until it reaches the vicinity of the pin, where a small amount directly flows across

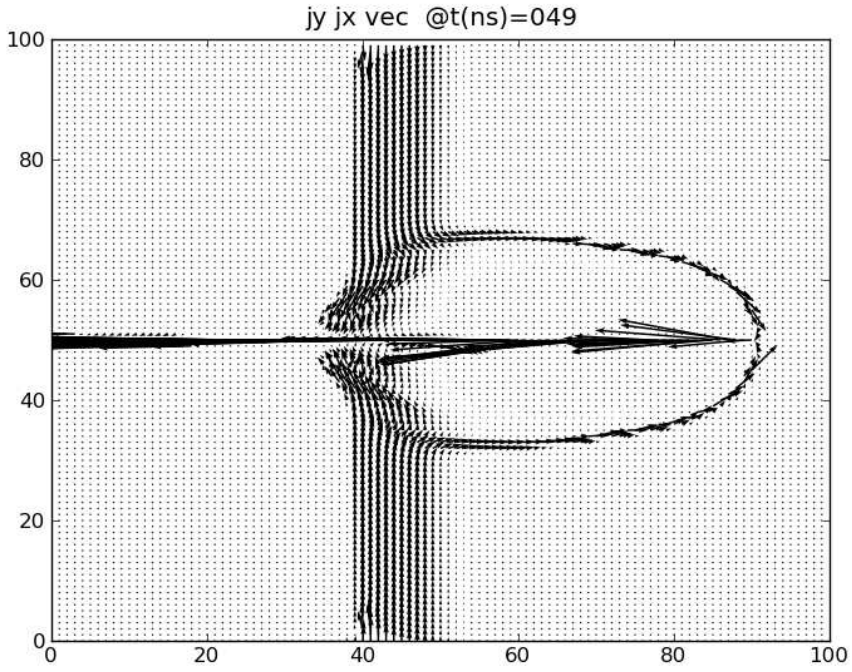


Figure 8.12: Vector field plot of the current density for the foil slab at 98 ns into the simulation. The current is seen entering from the anode boundary condition at the top and bottom of the figure branching into two current paths, one path directly to the cathode pin while the other current path goes through the surface of the plasma bubble.

the electron inertia current limiting density gap to the pin. The majority of the current flows over the bubble surface and back through the internal pinch column, sourcing the Joule heating. The current density vectors indicate magnetic reconnection occurring near the intersection of the pin and the bubble. The final field we consider is the velocity component in the direction of the bubble expansion. Figure 8.13 shows this component of velocity at 98 ns. The internal pinch column has a much lower expansion velocity as compared to the rest of the bubble, while the fastest expanding plasma occurs in the hollow region of the bubble. We also note that if random density perturbations are included in

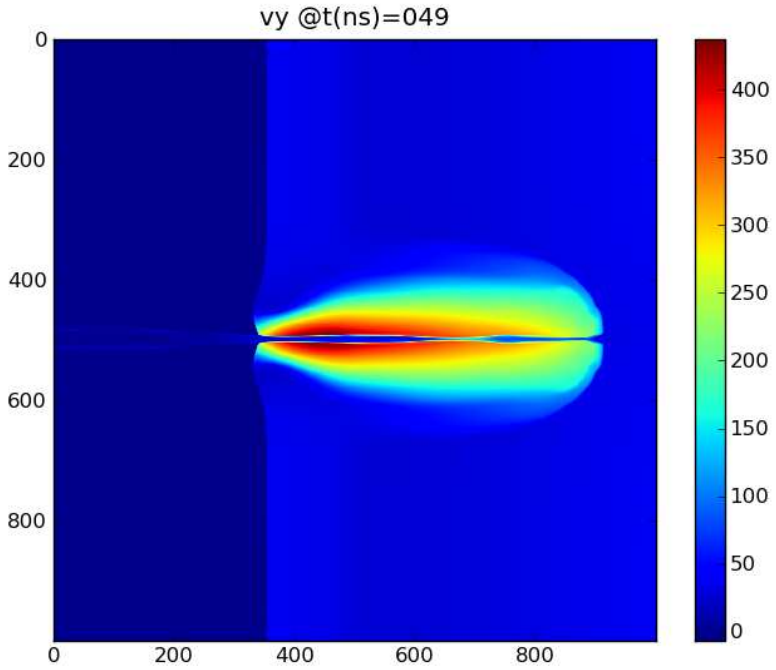


Figure 8.13: Plot of the dimensionless y component of velocity (right facing direction for figure orientation) for the foil slab at 98 ns into the simulation. The pinch column inside the bubble expands a much slower rate than the surface of the bubble.

the foil surface, a similar Hall instability as seen in the previous sections slab implosion occurs, although with longer spaced modulations.

The conclusions of this section are as follows. In the slab configuration, a thin aluminum foil with a pin cathode will still form the jet structures and the bubble structures that are qualitatively similar to those seen in geometries where the current density is radially convergent. The foil surface ablatively prefills the vacuum with plasma in a non-uniform matter that is subject to Hall instability if seeded with density perturbations. The jet is formed due to the collision of the non-uniformly ablated plasma from the foil surface. The bubble appears at the

pin cathode, even without radially convergent current flow. It expands into the plasma prefill creating an internal pinch column. After it leaves the system the density depleted area formed near the pin produces a region of strong electric field that sends a jet in the opposite direction the bubble expansion, toward the pin cathode.

CHAPTER 9

# CONCLUSIONS

Throughout this thesis, we have developed a self consistent model to treat the plasma-vacuum interface physics of plasmas created from pulsed power devices such as the 1 MA COBRA accelerator located at Cornell. As a result of exploring the physics of the plasma-vacuum interface, we have developed a code with unparalleled capability to implicitly integrate the generalized Ohm's law model and thus the Hall term. The inclusion of displacement current and finite electron inertia lets the code stably integrate over time steps much larger than allowed via implicit formulations of Hall MHD. Additionally, we have explained the process by which ablative streaming is initiated in the wire array configuration and for the first time numerically simulated the effect of precursor plasma instability originating from the Hall physics. The end result is a self consistent model for the plasma-vacuum interface, which unlike resistive MHD has no adjustable numerical parameters.

## 9.1 Chapter Review

We now review the conclusions of each chapter. In chapter two we examined the dimensionless plasma parameters that characterize the flows associated with wire array ablation and precursor formation. From this analysis, it is determined that two-fluid physics is essential in modeling current carrying plasma flowing into a vacuum region. The large electron and ion inertial lengths at the ablation front suggest that the validity of resistive MHD is limited for modeling pulsed power flows. We derive a reduced two-fluid model in the center-of-mass

frame and explore its solution near the plasma-vacuum boundary. The analysis of this generalized Ohm's law model shows that the collisionless physics is dominant, and, thus the electron inertial term must be retained. It is shown that the collisionless skin depth is dominant over anomalous collisionality even in the presence of lower hybrid instability.

In chapter three we developed numerical methods to stably integrate the generalized Ohm's law Maxwell system over time steps which are practical for the simulation of pulsed power loads driven over hundreds of nanoseconds. The key numerical developments are possible due to the inclusion of finite electron inertia and displacement current in the model. The electron inertia term, along with displacement current, let us solve for the current density as an independent variable, instead of being forced to take the curl of the magnetic field. The resulting equations are then strictly hyperbolic, with stiff source terms. Under this formulation, the relaxation scheme is used to solve the reduced two-fluid Riemann problem, while van Leer's MUSCl scheme allows for monotonic solution of the hyperbolic equations. Semi-implicit Runge-Kutta is used to time advance the system. The reduction from the full two-fluid model lets us implicitly integrate over the plasma frequency and electron cyclotron frequency. These source terms are independent of the grid scale and only depend upon the electron number density and magnetic field magnitude, respectively. The propagation of the whistler wave is now bounded for increasing wave number. The electron inertia term provides a resonance for the whistler dispersion, greatly increasing the stable time step as compared to the Hall MHD model. The implicit advance for the Hall term is reduced to a simple 3x3 solve that is spatially decoupled, unlike its spatially coupled form in Hall MHD, and by reducing the speed of light using the Boris correction, we may take time steps comparable to

MHD.

In chapter four we showed that the implicit generalized Ohm's law code recovers the ideal MHD limit for the shock tube problem, even when the inertial scale lengths are under-resolved. This shows that our application of van Leer's MUSCL scheme along with the Relaxation method of Xin and Jin is shock capturing under implicit time-advance for our hyperbolic system of equations in the MHD limit. This allows us to resolve the multi-scale nature of flows where some regions are MHD dominated, while other regions are two-fluid dominated. The numerical test of propagation of linear waves in the code shows that it recovers the electron cyclotron resonance for the whistler, bounding its phase velocity for large wave numbers.

In chapter five we explored the resistive MHD view of the wire array initiation problem. We find that the wire array configuration starts in a state where the wires are surrounded by closed local flux where the JxB force at every point is directed toward the wire core. It is only by thermal expansion sourced from Joule heating that the array may change its magnetic field configuration to an open state with global flux surrounding the wire core. This is accomplished through creation of a current sheet extending from the core in the direction of the geometric axis. This process has recently been experimentally verified [75]. The length of the current sheet required to open the flux around the core is found to scale with the inter wire gap and an analytic expression is presented. We show that for the expansion of the Joule heated plasma in to the vacuum the interface between these two regions is defined by the plasma $\beta = 1$ surface. The propagation velocity of the plasma-vacuum interface under the resistive MHD approximation is derived and when combined with the current sheet re-

quirement gives us a condition that must be satisfied is streaming ablation is to occur in a wire array under two-dimensional considerations. Thus, given the initial condition of the wire array and information on the current drive, we can predict if streaming ablation will occur. These analytic results are tested with simulation and found to be accurate.

In chapter six we numerically revisited the propagation of the plasma-vacuum interface under the generalized Ohm's model using our new algorithm. We showed that resistive MHD provides no unique solution in the presence of a plasma-vacuum interface. This is due to differences in the numerically calculated propagation velocity and heating rate of the plasma-vacuum interface when the density floor or method of resistive confinement of current density are modified. The generalized Ohm's law formulation has no free numerical parameters, just the resultant solution of the two-fluid equations and thus gives a self-consistent answer in the presence of flows in the electron and ion inertial regimes. We also show that the inclusion of finite electron inertia is sufficient to confine current to flow in the plasma, removing the need of a numerical vacuum resistivity.

In chapter seven we applied our numerical model to the simulation of wire arrays driven by a 1 MA peak, 100 ns rise time pulsed power device. The result is that for a globally constant resistivity, the generalized Ohm's law model still reproduces the qualitative features of an imploding wire array. These features are ablative streaming, current carrying precursor formation, implosion, and the formation of a pinch column on axis. We have found, by analyzing synthetic streak data of the wire array simulations, that agreement with experiment is obtained for the time of arrival of precursor plasma to the array axis when the

generalized Ohm's law model is used. However, exploration of the mass ablation rate is not in agreement with the rocket model and the arrays follow a 0D implosion trajectory. This suggests that additional physical models for thermal conduction or radiation transport may be necessary to correctly simulate the full wire array implosion process. We have shown that the generalized Ohm's law model gives a single answer for the ablation problem while the results of resistive MHD are dependent upon the floor density and vacuum resistivity. Additionally, we have shown that the resistive MHD model neglects the generation of radial electric fields and axial velocities created by the Hall effect. The magnitude of these fields amounts to as much as a 50 percent correction early on, falling to a 10 percent correction during the streaming ablation phase.

Finally, in chapter eight we studied the axial evolution of pulsed power loads under the generalized Ohm's law model. The first problem analyzed is the implosion of a thin slab where we have shown that an instability with wavelength of 0.5 mm in the ablated aluminum plasma is generated due to inclusion of the Hall term. This instability occurs in regimes where the ion inertial length is of order 1 mm and saturates at a constant wavelength. The instability imprints itself on the precursor column. We have shown that thin liners massed for implosion on the COBRA accelerator are theoretically predicted to be MRT unstable. Additionally, we have shown that inclusion of the Hall electric field breaks the symmetry of resistive MHD. The Hall term introduces an axial velocity component streaming from anode to cathode, with a velocity magnitude of order tens of kilometers per second. The result of this bulk axial flow is to delay the arrival of precursor plasma at the cathode. We then turned to simulating an ablative foil slab with cathode pin. We showed that in the slab geometry the magnetic bubble and jet still form, without the requirement of radial current convergence.

The jet forms due to collisions between the non-uniform ablation fronts expanding from the foil into the vacuum. As the magnetic bubble expands, a density depletion area forms at the pin which creates a strong electric field that drives a jet toward the pin cathode.

## 9.2 Future Work

Our analysis has lead to a numerical formulation of the reduced two-fluid model that has allowed us to simulate previously inaccessible plasma regimes. The wealth of new information on the physics of ablative pulsed power loads is overwhelming and there are many topics that must be explored in more depth.

### 9.2.1 Plasma-Vacuum Interface Dynamics

We we used the two-fluid model to explore the evolution of the plasma-vacuum interface for both the Resistive MHD and generalized Ohm's law models. We developed an analytic model describing the Resistive MHD propagation of this interface but we still require a more exact two-fluid description of its evolution. Additional analysis is required of the acceleration of the plasma-vacuum interface where finite electron inertia determines the current profile. This will help us understand the Joule heating rate and thus the expansion rate of such plasmas. Also, since different magnetic field profiles result from the collisional versus collisionless current limitation, the thermal conduction properties will differ between models. The effects on thermal conduction could be important for modeling Magnetized Target Fusion (MTF) loads where a plasma with finite

extent in to a vacuum impacts a liner. Future work will also involve examining the three dimensional evolution of the plasma-vacuum interface described by the generalized Ohm's law model.

### 9.2.2 Charge Carrier Starved Current Flow Effects

Future work entails understanding the physics of large electric fields in charge depleted regions. The mechanism by which plasma sheets pinch and thin, resulting in limited current flow, needs to be understood further. As shown in the simulation results of this thesis, large electric fields develop when charge carrier starvation limits the current flow in regions where the electron inertial length becomes large. This mechanism should be able to accelerate electrons to large velocities and is only present when the electron inertia term is retained. Additionally, the physics of inertial current limitation in three dimensional geometries needs to be explored. The exact mechanism by which extremely large electric fields form is an important topic in astrophysics. Charge density depletion regions in the shock front of supernovae could be a significant source of cosmic rays. Proper treatment of the plasma-vacuum interface and the electric fields generated from depletion regions may be important in understanding this problem.

### 9.2.3 Pulsed Power Load Anode-Cathode Asymmetry

Our simulation results show the generation of radial electric fields that are neglected under MHD simulation. The exact impact and role of these fields needs

to be better understood. One effect of the radial electric fields that appeared in our simulations was to generate anode to cathode flows. Recent experiments by John Greenly on the COBRA accelerator have shown anode-cathode asymmetry when metal cones are placed at the anode and electrode. The numerical exploration of this experiment could lead to a greater understanding of physics beyond the MHD approximation for wire arrays. The presence of axial flow also imparted a boundary layer behavior on the cathode. This led to nonuniform ablation along the slab and thus future work will involve understanding the flow of plasma along an electrode in the presence of shear due to the Hall term. In this manner we can better understand the ablation front lag observed at the cathode. The inclusion of the Hall term in the code implies that new insight may be gained into MTF loads. The Hall and electron inertia terms modify the magnetic reconnection rate of the plasma, a process that may be important for a field-reversed configuration under compression from a liner.

### 9.2.4 Hall Instabilities

One of the most important results of this thesis is the creation of an efficient model to advance the Hall term. The inclusion of displacement current and electron inertia has allowed us to numerically access previously unexplored regimes. For the first time we can see the role that the Hall effect plays in pulsed power loads. An important outstanding question is on the exact nature of the Hall instability of the plasma slab problem. This must be explored further and could be important in understanding the development of the fundamental mode in wire arrays. The unique formulation of our generalized Ohm's law model has been implemented in the PERSEUS (Plasma as an Extended-mhd

Relaxation System using an Efficient Upwind Scheme) code and will allow, for the first time, for full three dimensional calculations of pulsed power loads with the Hall and electron inertia physics.

APPENDIX A

# DERIVATION OF GENERALIZED OHM'S LAW MODEL

Many different approximations and assumptions are applied when reducing the separate ion and electron fluid equations in to a center-of-mass model. The large number of possible sub-models results in the generalized Ohm's law taking many different forms in literature. To provide a consistent model, we briefly review the derivation of the generalized Ohm's law given by Equation 2.11. We begin the derivation at the level of the two-fluid model, first introducing the continuity equations for each species in the center-of-mass frame.

Under the two-fluid model continuity constraint for ions is given by

$$\frac{\partial \rho_i}{\partial t} + \nabla \cdot (\rho_i \mathbf{u}_i) = 0 \tag{A.1}$$

and the continuity constraint for electrons is given by

$$\frac{\partial \rho_e}{\partial t} + \nabla \cdot (\rho_e \mathbf{u}_e) = 0 \tag{A.2}$$

where the ion mass density is defined in terms of number density and species mass as $\rho_i = m_i n_i$ and the electron mass density is $\rho_e = m_e n_e$. In the center-of-mass frame of the ion fluid and electron fluid, the total mass density $\rho$ is given by

$$\rho = m_i n_i + m_e n_e \tag{A.3}$$

and charge density $\rho_{\mathbf{c}}$ is defined below.

$$\rho_{\mathbf{c}} = Z e n_i - e n_e \tag{A.4}$$

The center-of-mass velocity $\mathbf{u}$ is defined as

$$\mathbf{u} = \frac{n_i m_i \mathbf{u_i} + n_e m_e \mathbf{u_e}}{\rho} \tag{A.5}$$

and with these definitions it is trivial to derive the equations for mass continuity

$$\frac{\partial \rho}{\partial t} + \nabla \cdot (\rho \mathbf{u}) = 0 \tag{A.6}$$

and charge continuity.

$$\frac{\partial \rho_c}{\partial t} + \nabla \cdot \mathbf{j} = 0 \tag{A.7}$$

These definitions are important as we now apply the same averaging procedure to the evolutionary equations for ion momentum and electron momentum.

The momentum equation for ions is given by

$$\frac{\partial \rho_i \mathbf{u}_i}{\partial t} + \nabla \cdot (\rho_i \mathbf{u}_i \mathbf{u}_i + P_i \mathbf{I}) = \frac{q_i \rho_i}{m_i} (\mathbf{E} + \mathbf{u}_i \times \mathbf{B}) + \mathbf{R}_i \tag{A.8}$$

and the momentum equation for electrons is given by

$$\frac{\partial \rho_e \mathbf{u}_e}{\partial t} + \nabla \cdot (\rho_e \mathbf{u}_e \mathbf{u}_e + P_e \mathbf{I}) = \frac{q_e \rho_e}{m_e} (\mathbf{E} + \mathbf{u}_e \times \mathbf{B}) + \mathbf{R}_e \tag{A.9}$$

where the variable names were defined in Chapter 2. We desire to work in the center-of-mass frame of the electron and ion species and so for convenience we define the difference between the ion and electron velocity as $\Gamma$, where

$$\mathbf{\Gamma} = \mathbf{u_i} - \mathbf{u_e} \tag{A.10}$$

which along with our definition of current density $\mathbf{j}$ given by

$$\mathbf{j} = Z e n_i \mathbf{u_i} - e n_e \mathbf{u_e} \tag{A.11}$$

allows us to represent the two-fluid momentum equations in terms of center-of-mass variables.

The ion and electron velocities can be exactly represented in our center-of-mass frame variables through the following definitions

$$\mathbf{u_i} = \frac{\rho \mathbf{u}}{n_i m_i} - \frac{n_e m_e}{n_i m_i}(\mathbf{u_i} - \mathbf{\Gamma}) = \mathbf{u} + \frac{n_e m_e}{\rho}\mathbf{\Gamma} \tag{A.12}$$

$$\mathbf{u_e} = \frac{\rho \mathbf{u}}{n_e m_e} - \frac{n_i m_i}{n_e m_e}(\mathbf{\Gamma} + \mathbf{u_e}) = \mathbf{u} - \frac{n_i m_i}{\rho}\mathbf{\Gamma} \tag{A.13}$$

Using these relations for the species velocities we can derive an exact expression for $\Gamma$ in terms of the mass density, charge density, current density, and center-of-mass velocity. This relation is given by

$$\mathbf{\Gamma} = \frac{\rho}{e n_i n_e (Z m_e + m_i)}[\mathbf{j} - \rho_c \mathbf{u}] \tag{A.14}$$

Next, we multiply Equation A.8 by $q_i/m_i$ and Equation A.9 by $q_e/m_e$ and apply the relations $\rho_e = m_e n_e$ and $\rho_i = m_i n_i$. Adding the resulting equations and substituting in Equations A.10 -A.11 and Equations A.12 - A.13 gives an expression for the evolution of the current density in terms of the center-of-mass velocities $\mathbf{u}$ and $\mathbf{\Gamma}$. The generalized Ohm's law is

$$\frac{\partial \mathbf{j}}{\partial t} + \nabla \cdot \left[ q_i n_i \left(\mathbf{u} + \frac{\rho_e}{\rho}\mathbf{\Gamma}\right)\left(\mathbf{u} + \frac{\rho_e}{\rho}\mathbf{\Gamma}\right) + q_e n_e \left(\mathbf{u} - \frac{\rho_i}{\rho}\mathbf{\Gamma}\right)\left(\mathbf{u} - \frac{\rho_i}{\rho}\mathbf{\Gamma}\right) + \left(\frac{q_i}{m_i}P_i + \frac{q_e}{m_e}P_e\right)\mathbf{I}\right] =$$
$$\frac{q_i^2 n_i}{m_i}\left[\mathbf{E} + \left(\mathbf{u} + \frac{\rho_e}{\rho}\mathbf{\Gamma}\right) \times \mathbf{B}\right] + \frac{q_e^2 n_e}{m_e}\left[\mathbf{E} + \left(\mathbf{u} - \frac{\rho_i}{\rho}\mathbf{\Gamma}\right) \times \mathbf{B}\right] \tag{A.15}$$

where no approximation to the two-fluid model has been assumed.

We now simplify Equation A.15 by neglecting terms of order $m_e/m_i$ while making no assumptions about quasi-neutrality. Under the approximation of

Equation A.17, $\Gamma$ reduces to

$$\mathbf{\Gamma} = \frac{\mathbf{j}}{en_e} - \frac{\rho_c \mathbf{u}}{en_e} \tag{A.16}$$

which upon substitution into Equation A.15 and using the approximation

$$m_e \ll m_i \tag{A.17}$$

gives the approximate generalized Ohm's law derived in Chapter 2. Its dimensional form, using the definition $\xi = 1 + \rho_c / en_e$ is given by

$$\begin{aligned} \frac{\partial \mathbf{j}}{\partial t} + \nabla \cdot \left[ \xi \left( \mathbf{uj} + \mathbf{ju} - \rho_c \mathbf{uu} \right) - \frac{\mathbf{jj}}{en_e} - \frac{e}{m_e} P_e \mathbf{I} \right] = \\ \frac{e^2 n_e}{m_e} \left[ \mathbf{E} + \left( \xi \mathbf{u} - \frac{\mathbf{j}}{en_e} \right) \times \mathbf{B} - \eta \left( \mathbf{j} - \rho_c \mathbf{u} \right) \right] \end{aligned} \tag{A.18}$$

and we have completed our derivation. The approximate generalized Ohm's law given by Equation A.18 still contains the two-fluid variable corresponding to the electron number density. For the singly ionized quasi-neutral case this is trivially found from the expression $n_e \approx n$. For the more general case of an multiply ionized fluid, the electron number density is calculated from the charge continuity constraint of Equation A.7.

## BIBLIOGRAPHY


[1] Michael E. Cuneo, Roger A. Vesey, Jr. John L. Porter, Gordon A. Chandler, David L. Fehl, Terrance L. Gilliland, David L. Hanson, John S. McGurn, Paul G. Reynolds, Laurence E. Ruggles, Hans Seamen, Rick B. Spielman, Ken W. Struve, William A. Stygar, Walter W. Simpson, Jose A. Torres, David F. Wenger, James H. Hammer, Peter W. Rambo, Darrell L. Peterson, and George C. Idzorek, "Development and characterization of a z-pinch-driven hohlraum high-yield inertial confinement fusion target concept," 2001, vol. 8, pp. 2257–2267, AIP.

[2] T. W. L. Sanford, R. E. Olson, R. C. Mock, G. A. Chandler, R. J. Leeper, T. J. Nash, L. E. Ruggles, W. W. Simpson, K. W. Struve, D. L. Peterson, R. L. Bowers, and W. Matuska, "Dynamics of a z-pinch x-ray source for heating inertial-confinement-fusion relevant hohlraums to 120–160 ev," *Physics of Plasmas*, vol. 7, no. 11, pp. 4669–4682, 2000.

[3] C. Deeney, C. A. Coverdale, M. R. Douglas, T. J. Nash, R. B. Spielman, K. W. Struve, K. G. Whitney, J. W. Thornhill, J. P. Apruzese, R. W. Clark, J. Davis, F. N. Beg, and J. Ruiz-Camacho, "Titanium k-shell x-ray production from high velocity wire array implosions on the 20-ma z accelerator," 1999, vol. 6, pp. 2081–2088, AIP.

[4] D. J. Ampleford, S. V. Lebedev, S. N. Bland, S. C. Bott, J. P. Chittenden, C. A. Jennings, V. L. Kantsyrev, A. S. Safronova, V. V. Ivanov, D. A. Fedin, P. J. Laca, M. F. Yilmaz, V. Nalajala, I. Shrestha, K. Williamson, G. Osborne, A. Haboub, and A. Ciardi, "Dynamics of conical wire array z-pinch implosions," *Physics of Plasmas*, vol. 14, no. 10, pp. 102704, 2007.

[5] D. A. Chalenski, B. R. Kusse, and J. B. Greenly, "Soldered contact and current risetime effects on negative polarity wire array z pinches," *Physics of Plasmas*, vol. 16, no. 8, pp. 082707, 2009.

[6] S. A. Pikuz, T. A. Shelkovenko, D. B. Sinars, J. B. Greenly, Y. S. Dimant, and D. A. Hammer, "Multiphase foamlike structure of exploding wire cores," *Phys. Rev. Lett.*, vol. 83, no. 21, pp. 4313–4316, Nov 1999.

[7] J. P. Chittenden, S. V. Lebedev, A. R. Bell, R. Aliaga-Rossel, S. N. Bland, and M. G. Haines, "Plasma formation and implosion structure in wire array $z$ pinches," *Phys. Rev. Lett.*, vol. 83, no. 1, pp. 100–103, Jul 1999.

[8] S. V. Lebedev, F. N. Beg, S. N. Bland, J. P. Chittenden, A. E. Dangor, M. G.

Haines, K. H. Kwek, S. A. Pikuz, and T. A. Shelkovenko, "Effect of discrete wires on the implosion dynamics of wire array z pinches," *Physics of Plasmas*, vol. 8, no. 8, pp. 3734–3747, 2001.

[9] T. W. L. Sanford, R. C. Mock, R. B. Spielman, M. G. Haines, J. P. Chittenden, K. G. Whitney, J. P. Apruzese, D. L. Peterson, J. B. Greenly, D. B. Sinars, D. B. Reisman, and D. Mosher, "Wire array z-pinch insights for enhanced x-ray production," 1999, vol. 6, pp. 2030–2040, AIP.

[10] S. V. Lebedev, F. N. Beg, S. N. Bland, J. P. Chittenden, A. E. Dangor, and M. G. Haines, "Snowplow-like behavior in the implosion phase of wire array z pinches," 2002, vol. 9, pp. 2293–2301, AIP.

[11] E. G. Harris, "Rayleigh-taylor instabilities of a collapsing cylindrical shell in a magnetic field," *Physics of Fluids*, vol. 5, no. 9, pp. 1057–1062, 1962.

[12] M. E. Cuneo, E. M. Waisman, S. V. Lebedev, J. P. Chittenden, W. A. Stygar, G. A. Chandler, R. A. Vesey, E. P. Yu, T. J. Nash, D. E. Bliss, G. S. Sarkisov, T. C. Wagoner, G. R. Bennett, D. B. Sinars, J. L. Porter, W. W. Simpson, L. E. Ruggles, D. F. Wenger, C. J. Garasi, B. V. Oliver, R A. Aragon, W. E. Fowler, M. C. Hettrick, G. C. Idzorek, D. Johnson, K. Keller, and S. E. Lazier, "Characteristics and scaling of tungsten-wire-array *z* -pinch implosion dynamics at 20 ma," *Phys. Rev. E*, vol. 71, no. 4, pp. 046406, Apr 2005.

[13] Jr. Lyman Spitzer and Raymond J. Seeger, "Physics of fully ionized gases," *American Journal of Physics*, vol. 31, no. 11, pp. 890–891, 1963.

[14] Huba Beam Physics, J. D. Huba, and Beam Physics Branch, "Nrl plasma formulary," 1994.

[15] Edmund P. Yu, B.V. Oliver, D.B. Sinars, T.A. Mehlhorn, M.E. Cuneo, P.V. Sasorov, M.G. Haines, and S.V. Lebedev, "Steady-state radiation ablation in the wire-array z pinch," *Phys. Plasmas*, vol. 14, pp. 022705, 2007.

[16] D. B. Sinars, M. E. Cuneo, E. P. Yu, D. E. Bliss, T. J. Nash, J. L. Porter, C. Deeney, M. G. Mazarakis, G. S. Sarkisov, and D. F. Wenger, "Mass-profile and instability-growth measurements for 300-wire *z*-pinch implosions driven by 14˜18 ma," *Phys. Rev. Lett.*, vol. 93, no. 14, pp. 145002, Sep 2004.

[17] S. I. Braginskii, "Transport processes in a plasma," *Reviews of Plasma Physics*, vol. 1, pp. 205, 1965.

[18] H. Dreicer, "Electron and ion runaway in a fully ionized gas," *Physical Review*, vol. 115, no. 2, pp. 238–249, 1959.

[19] N.A. Krall and P.C. Liewer, "Low-frequency instabilities in magnetic pulses," *Physical Review A*, vol. 4, no. 5, pp. 2094–2103, 1971.

[20] D. Biskamp and R. Chodura, "Computer simulation of anomalous dc resistivity," *Phys. Rev. Lett.*, vol. 27, no. 23, pp. 1553–1556, Dec 1971.

[21] C. T. Dum, R. Chodura, and D. Biskamp, "Turbulent heating and quenching of the ion sound instability," *Phys. Rev. Lett.*, vol. 32, no. 22, pp. 1231–1234, Jun 1974.

[22] R Chodura, G Bardotti, and F Engelmann, "Numerical investigation of the anomalous resistivity due to two-stream instability," *Plasma Physics*, vol. 13, no. 12, pp. 1099–1110, 1971.

[23] J. Aparicio, M. G. Haines, R. J. Hastie, and J. P. Wainwright, "Fast reconnection due to localized anomalous resistivity," *Physics of Plasmas*, vol. 5, no. 9, pp. 3180–3186, 1998.

[24] J. P. Chittenden, "The effect of lower hybrid instabilities on plasma confinement in fiber z pinches," *Physics of Plasmas*, vol. 2, no. 4, pp. 1242–1249, 1995.

[25] R. C. Davidson, N. T. Gladd, C. S. Wu, and J. D. Huba, "Effects of finite plasma beta on the lower-hybrid-drift instability," *Physics of Fluids*, vol. 20, no. 2, pp. 301–310, 1977.

[26] Y. Takeda and H. Inuzuka, "Anomalous resistivity caused by nonlinear lower hybrid waves in a high-voltage linear plasma discharge," *Phys. Lett. A*, vol. 265, pp. 282–287, 2000.

[27] C. K. Birdsall and Langdon, *Plasma Physics via Computer Simulation (Series on Plasma Physics)*, Taylor & Francis, January 1991.

[28] U. Shumlak and J. Loverich, "Approximate riemann solver for the two-fluid plasma model," *Journal of Computational Physics*, vol. 187, no. 2, pp. 620 – 638, 2003.

[29] A. Hakim, J. Loverich, and U. Shumlak, "A high resolution wave propaga-

tion scheme for ideal two-fluid plasma equations," *Journal of Computational Physics*, vol. 219, no. 1, pp. 418 – 442, 2006.

[30] J. Loverich and U. Shumlak, "A discontinuous galerkin method for the full two-fluid plasma model," *Computer Physics Communications*, vol. 169, no. 1-3, pp. 251 – 255, 2005, Proceedings of the Europhysics Conference on Computational Physics 2004.

[31] C. R. Sovinec, D. D. Schnack, A. Y. Pankin, D. P. Brennan, H. Tian, D. C. Barnes, S. E. Kruger, E. D. Held, C. C. Kim, X. S. Li, D. K. Kaushik, S. C. Jardin, and the NIMROD Team, "Nonlinear extended magnetohydrodynamics simulation using high-order finite elements," *Journal of Physics Conference Series*, vol. 16, pp. 25–34, Jan. 2005.

[32] L. Chacón and D. A. Knoll, "A 2d high-ßhall mhd implicit nonlinear solver," *J. Comput. Phys.*, vol. 188, no. 2, pp. 573–592, 2003.

[33] R. J. LeVeque, *Finite Volume Methods for Hyperbolic Problems*, Cambridge University Press, 2005.

[34] Ami Harten, "High resolution schemes for hyperbolic conservation laws," *J. Comput. Phys.*, vol. 135, no. 2, pp. 260–278, 1997.

[35] S. K. Godunov, "High resolution schemes for hyperbolic conservation laws," *Mat. Sb.*, vol. 47, pp. 271, 1959.

[36] Shi Jin and Zhouping Xin, "The relaxation schemes for systems of conservation laws in arbitrary space dimensions," *Comm. Pure Appl. Math*, vol. 48, no. 3, pp. 235 – 276, 1995.

[37] Bram van Leer, "Towards the ultimate conservative difference scheme. v. a second-order sequel to godunov's method," *Journal of Computational Physics*, vol. 32, no. 1, pp. 101 – 136, 1979.

[38] Pavel B. Bochev, Christopher J. Garasi, Jonathan J. Hu, Allen C. Robinson, and Raymond S. Tuminaro, "An improved algebraic multigrid method for solving maxwell's equations," *SIAM J. Sci. Comput.*, vol. 25, no. 2, pp. 623–642, 2003.

[39] C.A. Jennings, "Radiation transport effects in wire array z-pinches and magneto-hydrodynamic modelling techniques," *Ph.D. Thesis*, 2005.

[40] J.P. Boris, "Physically motivated solution of the alfven problem," *Naval Res. Lab. Memo. Rept. No. 2167*, 1970.

[41] J. P. Chittenden and C. A. Jennings, "Development of instabilities in wire-array z pinches," *Physical Review Letters*, vol. 101, no. 5, pp. 055005, 2008.

[42] Hy Trac and UeLi Pen, "A primer on eulerian computational fluid dynamics for astrophysics," *Publications of the Astronomical Society of the Pacific*, vol. 115, no. 805, pp. 303–321, 2003.

[43] Ue-Li Pen, Phil Arras, and ShingKwong Wong, "A free, fast, simple, and efficient total variation diminishing magnetohydrodynamic code," *The Astrophysical Journal Supplement Series*, vol. 149, no. 2, pp. 447–455, 2003.

[44] Thomas A. Gardiner and James M. Stone, "An unsplit godunov method for ideal mhd via constrained transport," *Journal of Computational Physics*, vol. 205, no. 2, pp. 509 – 539, 2005.

[45] P. K. Sweby, "High resolution schemes using flux limiters for hyperbolic conservation laws," *SIAM Journal on Numerical Analysis*, vol. 21, no. 5, pp. 995–1011, 1984.

[46] Gabor Toth, "The div b=0 constraint in shock-capturing magnetohydrodynamics codes," *Journal of Computational Physics*, vol. 161, no. 2, pp. 605 – 652, 2000.

[47] Dinshaw S. Balsara and Daniel Spicer, "Maintaining pressure positivity in magnetohydrodynamic simulations," *Journal of Computational Physics*, vol. 148, no. 1, pp. 133 – 148, 1999.

[48] L. Chacon and D. A. Knoll, "A 2d high-beta hall mhd implicit nonlinear solver," *Journal of Computational Physics*, vol. 188, no. 2, pp. 573 – 592, 2003.

[49] Lukas Arnold, Jrgen Dreher, and Rainer Grauer, "A semi-implicit hall-mhd solver using whistler wave preconditioning," *Computer Physics Communications*, vol. 178, no. 8, pp. 553 – 557, 2008.

[50] T E Stringer, "Low-frequency waves in an unbounded plasma," *Journal of Nuclear Energy. Part C, Plasma Physics, Accelerators, Thermonuclear Research*, vol. 5, no. 2, pp. 89–107, 1963.

[51] E. N. Sarmin and L. A. Chudov, "On the stability of the numerical integration of systems of ordinary differential equations arising in the use of the straight line method," *USSR Computational Mathematics and Mathematical Physics*, vol. 3, no. 6, pp. 1537 – 1543, 1963.

[52] L. Pareschi and G. Russo, "Implicit-explicit runge-kutta schemes and applications to hyperbolic systems with relaxation," *Journal of Scientific Computing*, vol. 25, no. 1, pp. 129–155, 2005.

[53] Uri M. Ascher, Steven J. Ruuth, and Raymond J. Spiteri, "Implicit-explicit runge-kutta methods for time-dependent partial differential equations," *Appl. Numer. Math.*, vol. 25, no. 2-3, pp. 151–167, 1997.

[54] J. D. Huba, "Hall Magnetohydrodynamics - A Tutorial," in *Space Plasma Simulation*, J. Büchner, C. Dum, & M. Scholer, Ed., 2003, vol. 615 of *Lecture Notes in Physics, Berlin Springer Verlag*, pp. 166–192.

[55] M. Brio and C. C. Wu, "An upwind differencing scheme for the equations of ideal magnetohydrodynamics," *Journal of Computational Physics*, vol. 75, no. 2, pp. 400 – 422, 1988.

[56] J. B. Greenly, J. D. Douglas, D. A. Hammer, B. R. Kusse, S. C. Glidden, and H. D. Sanders, "A 1 ma, variable risetime pulse generator for high energy density plasma research," *Rev. Sci. Instrum.*, vol. 79, pp. 073501, 2008.

[57] R. B. Spielman, C. Deeney, G. A. Chandler, M. R. Douglas, D. L. Fehl, M. K. Matzen, D. H. McDaniel, T. J. Nash, J. L. Porter, T. W. L. Sanford, J. F. Seamen, W. A. Stygar, K. W. Struve, S. P. Breeze, J. S. McGurn, J. A. Torres, D. M. Zagar, T. L. Gilliland, D. O. Jobe, J. L. McKenney, R. C. Mock, M. Vargas, T. Wagoner, and D. L. Peterson, "Tungsten wire-array z-pinch experiments at 200 tw and 2 mj," *Physics of Plasmas*, vol. 5, no. 5, pp. 2105–2111, 1998.

[58] S. V. Lebedev, F. N. Beg, S. N. Bland, J. P. Chittenden, A. E. Dangor, M. G. Haines, K. H. Kwek, S. A. Pikuz, and T. A. Shelkovenkob, "Effect of discrete wires on the implosion dynamics of wire array z pinches," *Phys. Plasmas*, vol. 8, pp. 3734, 2001.

[59] Eduadro M. Waisman, M.E. Cuneo, W.A. Stygar, P.V. Sasorov, and E.P. Yu, "A model for ablated-plasma distribution and width for wire-array z-pinch implosions," *Phys. Plasmas*, vol. 13, pp. 062702, 2006.

[60] Alexander L. Velikovich, Igor V. Sokolov, and Andrey A. Esaulov, "Perfectly conducting incompressible fluid model of a wire array implosion," *Physics of Plasmas*, vol. 9, no. 4, pp. 1366–1380, 2002.

[61] V. V. Aleksandrov, A. V. Branitskii, G. S. Volkov, E. V. Grabovskii, M. V. Zurin, S. L. Nedoseev, G. M. Oleinik, A. A. Samokhin, and P. V. Sasorov, "Dynamics of Heterogeneous Liners with Prolonged Plasma Creation," *Plasma Physics Reports*, vol. 27, pp. 89–109, Feb. 2001.

[62] P. V. Sasorov, B. V. Oliver, E. P. Yu, and T. A. Mehlhorn, "One-dimensional ablation in multiwire arrays," *Physics of Plasmas*, vol. 15, no. 2, pp. 022702, 2008.

[63] J. P. Chittenden, S. V. Lebedev, B. V. Oliver, E. P. Yu, and M. E. Cuneo, "Equilibrium flow structures and scaling of implosion trajectories in wire array z pinches," *Physics of Plasmas*, vol. 11, no. 3, pp. 1118–1127, 2004.

[64] J.P. Chittenden, S.V. Lebedev, S.N. Bland, F.N. Beg, and M.G. Haines, "One-, two-, and three-dimensional modeling of the different phases of wire array z-pinch evolution," *Phys. Plasmas*, vol. 8, pp. 2305, 2001.

[65] M.G. Haines, "A three-dimensional model of wire array instability, ablation, and jetting," *IEEE Trans. Plasma Sci.*, vol. 30, pp. 588, 2002.

[66] C. J. Garasi, D.E. Bliss, T.A. Mehlhorn, B.V. Oliver, A.C. Robinson, and G.S. Sarkisov, "Multi-dimensional high energy density physics modeling and simulation of wire array z-pinch physics," *Phys. Plasmas*, vol. 11, pp. 2729, 2004.

[67] J. P. Chittenden and C. A. Jennings, "Development of instabilities in wire-array z pinches," *Physical Review Letters*, vol. 101, no. 5, pp. 055005, 2008.

[68] Ch. Sack and H. Schamel, "Plasma expansion into vacuum – a hydrodynamic approach," *Physics Reports*, vol. 156, pp. 311 – 395, 1987.

[69] R. P. Drake, *High-Energy-Density Physics*, Springer, 2006.

[70] R. D. McBride, T. A. Shelkovenko, S. A. Pikuz, D. A. Hammer, J. B. Greenly, B. R. Kusse, J. D. Douglass, P. F. Knapp, K. S. Bell, I. C. Blesener, and D. A. Chalenski, "Implosion dynamics and radiation characteristics of wire-array z pinches on the cornell beam research accelerator," *Physics of Plasmas*, vol. 16, no. 1, pp. 012706, 2009.

[71] S. V. Lebedev, J. P. Chittenden, F. N. Beg, S. N. Bland, A. Ciardi, D. Ampleford, S. Hughes, M. G. Haines, A. Frank, E. G. Blackman, , and T. Gardiner, "Laboratory astrophysics and collimated stellar outflows: The production of radiatively cooled hypersonic plasma jets," *The Astrophysical Journal*, vol. 564, no. 1, pp. 113–119, 2002.

[72] A. Ciardi, "Laboratory Studies of Astrophysical Jets," in *Lecture Notes in Physics, Berlin Springer Verlag*, P. J. Valente Garcia & J. M. Ferreira, Ed., 2009, vol. 793 of *Lecture Notes in Physics, Berlin Springer Verlag*, pp. 31–50.

[73] P. F. Knapp, K. S. Bell, I. C. Blesener, D. A. Chalenski, J. D. Douglass, J. B. Greenly, M. R. Martin, R. D. McBride, S. A. Pikuz, T. A. Shelkovenko, D. A. Hammer, B. R. Kusse, and G. N. HAll, "Development of the axial instability in low wire number wire array z-pinches," 2009, vol. 1088, pp. 61–64, AIP.

[74] S V Lebedev, A Ciardi, D J Ampleford, S N Bland, S C Bott, J P Chittenden, G N Hall, J Rapley, C Jennings, M Sherlock, A Frank, and E G Blackman, "Production of radiatively cooled hypersonic plasma jets and links to astrophysical jets," *Plasma Physics and Controlled Fusion*, vol. 47, no. 12B, pp. B465–B479, 2005.

[75] John Greenly, Matthew Martin, Isaac Blesener, David Chalenski, Patrick Knapp, and Ryan McBride, "The role of flux advection in the development of the ablation streams and precursors of wire array z-pinches," 2009, vol. 1088, pp. 53–56, AIP.